



UNIVERSIDAD NACIONAL AUTÓNOMA DE MÉXICO  
PROGRAMA DE POSGRADO EN ASTROFÍSICA  
Instituto de Ciencias Nucleares, Ciudad Universitaria.

**DESINTEGRACIÓN DE CÚMULOS ESTELARES  
MASIVOS EN FORMACIÓN**

TESIS

QUE PARA OPTAR POR EL GRADO DE:  
**DOCTOR EN CIENCIAS (ASTROFÍSICA)**

PRESENTA:

**PEDRO RUBEN RIVERA ORTIZ**

TUTOR PRINCIPAL

**DR. ARY RODRÍGUEZ GONZÁLEZ,**  
Instituto de Ciencias Nucleares, Ciudad Universitaria.

CIUDAD UNIVERSITARIA, CDMX, AGOSTO 2019



Universidad Nacional  
Autónoma de México

Dirección General de Bibliotecas de la UNAM

**Biblioteca Central**



**UNAM – Dirección General de Bibliotecas**  
**Tesis Digitales**  
**Restricciones de uso**

**DERECHOS RESERVADOS ©**  
**PROHIBIDA SU REPRODUCCIÓN TOTAL O PARCIAL**

Todo el material contenido en esta tesis esta protegido por la Ley Federal del Derecho de Autor (LFDA) de los Estados Unidos Mexicanos (México).

El uso de imágenes, fragmentos de videos, y demás material que sea objeto de protección de los derechos de autor, será exclusivamente para fines educativos e informativos y deberá citar la fuente donde la obtuvo mencionando el autor o autores. Cualquier uso distinto como el lucro, reproducción, edición o modificación, será perseguido y sancionado por el respectivo titular de los Derechos de Autor.



# Agradecimientos

Después de mucho tiempo, finalmente llegó el día de concluir un proyecto que ha significado mucho para mi y quiero agradecer a los involucrados, empezando por mi familia. A mis padres, que me han dado todas las herramientas para vivir productivamente. A mi madre, por todos los valores, la confianza y el apoyo que me ha brindado. A mi padre, por su motivación y su ejemplo de superar los defectos propios. A mis hermanos. A Anel, por su preocupación, su cariño y toda la ayuda incondicional que nunca me ha sobrado. A José Francisco, que siempre ha sido un gran ejemplo de esfuerzo y de ser humano para mi. A Alfonso, por su franqueza, su sinceridad y por probar los límites de mi paciencia. A mis cuñados, Claudia, Andrea y René, por hacer mas grande nuestra familia.

Agradezco también a Claudia, por motivarme a seguir mis metas, por aventurarse conmigo, por su paciencia, por las ganas de vivir que me brinda, por todo el amor que me da y por compartir su vida con la mía. A su familia por su apoyo y su confianza.

A Ary, por su amistad, sus consejos y las ideas que hemos compartido. También por asesorarme en el posgrado, hasta que lo conocí pensaba en ser un científico *a pesar* de los demás y ahora creo que puedo serlo *con* los demás. A Liliana, por su sinceridad, su ayuda y por hacerme sentir en familia. Al resto del grupo Raga, Pablo, Esquivel, Claudio y Fabio, por todas las platicas tan interesantes que compartieron conmigo. A todos en el ñoño-journal, donde compartimos muchos temas y nos divertimos exponiendo cada semana.

A los amigos que me han acompañado desde hace muchos años, Blanca, Luis Angel, Gerardo, Nayeli y Tania, que han estado al pendiente de mi. También a todos mis alumnos que se volvieron mis amigos y que también me han enseñado y motivado a seguir por este camino. A los amigos que hice durante el posgrado, Alberto, Arturo y Antonio y, especialmente a Rosa y a Diana, que han estado conmigo en toda esta aventura, me han ayudado sin pedirme nada

y que quiero como hermanas.

A mis sinodales, Luis Felipe Rodríguez, Luis Zapata, Sergiy Silich, Jose María Torrelles y, en especial, a Jorge Cantó, que me ayudaron a incrementar el nivel de este trabajo sustancialmente y de quienes me queda mucho que aprender. También a Medel Perez, quien inspiró en mí la vocación científica y a Ciro Robles que me dirigió a la astronomía. Agradezco a los proyectos CONACYT 220626, DGAPA-UNAM IA103115, IN109715, IN109416, PE103609, PAPIIT-UNAM IN-109518, IG-100218 y al High Performance Computing OCCIGEN CINES del proyecto DARI A0030406842. Tambien a CONACyT-México por la becas otorgadas con el expediente 29057 y al apoyo económico de COZCyT. También agradezco a Bertha, por su ayuda y paciencia con mis trámites y finalmente al juez anónimo.

*Dedicado a mis sobrinos,  
Rubén, Regina, Santiago, Venus, Abigail, Ian y Mayola.*

# Contents

|          |   |           |
|----------|---|-----------|
| <b>1</b> | <b>Orion BN/KL</b>  | <b>5</b>  |
| 1.1      | Main goals . . . . .                                      | 11        |
| 1.1.1    | Particular goals . . . . .                                | 11        |
| <b>2</b> | <b>Motion of losing mass plasmon</b>                      | <b>15</b> |
| 2.1      | Introduction . . . . .                                    | 15        |
| 2.2      | Analytical model . . . . .                                | 17        |
| 2.2.1    | De Young & Axford's plasmon . . . . .                     | 17        |
| 2.2.2    | Mass loss rate . . . . .                                  | 18        |
| 2.3      | Axisymmetric simulations of plasmon evolution . . . . .   | 22        |
| 2.3.1    | The numerical setup . . . . .                             | 22        |
| 2.3.2    | Numerical models of the plasmon evolution . . . . .       | 24        |
| 2.4      | Physical properties of the plasmon . . . . .              | 27        |
| 2.5      | Conclusions . . . . .                                     | 32        |
| <b>3</b> | <b>The Ejection Conditions of the Orion BN/KL fingers</b> | <b>35</b> |
| 3.1      | Introduction . . . . .                                    | 35        |
| 3.2      | Observations . . . . .                                    | 37        |
| 3.2.1    | Ballistic motion . . . . .                                | 40        |
| 3.3      | Dynamic model . . . . .                                   | 43        |
| 3.4      | Conclusions . . . . .                                     | 48        |
| <b>4</b> | <b>KIMYA: A chemical network solver</b>                   | <b>51</b> |
| 4.1      | Introduction . . . . .                                    | 51        |

|          |  |            |
|----------|--|------------|
| 4.2      | The numerical solution of the network chemical rates . . . . .   | 54         |
| 4.2.1    | The Newton-Raphson iteration . . . . .                           | 55         |
| 4.2.2    | Conservation equations . . . . .                                 | 57         |
| 4.2.3    | Initial Newton-Raphson guess . . . . .                           | 57         |
| 4.3      | Description of KIMYA . . . . .                                   | 58         |
| 4.4      | The reactive flow equations . . . . .                            | 58         |
| 4.5      | Numerical and experimental models to code verification . . . . . | 61         |
| 4.5.1    | Sequence reactions test . . . . .                                | 61         |
| 4.5.2    | Dark cloud model . . . . .                                       | 63         |
| 4.5.3    | Nitric oxide formed during lightning discharge . . . . .         | 65         |
| 4.5.4    | Scaling of the computational time . . . . .                      | 72         |
| 4.6      | Discussion and Conclusion . . . . .                              | 73         |
| <b>5</b> | <b>Modeling the CO emission</b>                                  | <b>79</b>  |
| 5.1      | Introduction . . . . .   | 79         |
| 5.2      | Numerical simulation . . . . .                                   | 82         |
| 5.3      | The CO emission of the streamers . . . . .                       | 86         |
| 5.4      | Discussion . . . . .   | 91         |
| <b>6</b> | <b>Conclusions</b>   | <b>93</b>  |
|          | <b>Bibliography</b>  | <b>97</b>  |
| <b>A</b> | <b>Speed of sound</b>  | <b>105</b> |
| <b>B</b> | <b>Numerical densities of the molecules</b>                      | <b>109</b> |
| <b>C</b> | <b>Reaction selection</b>  | <b>123</b> |
| <b>D</b> | <b>Papers related to this thesis</b>                             | <b>125</b> |
|          | <b>List of Figures</b>   | <b>131</b> |
|          | <b>List of Tables</b>  | <b>135</b> |



# Abstract

Massive and young stars in the center of highly populated clusters can suffer very close dynamic encounters that can lead to very energetic and explosive events. Nevertheless, there is very little clear evidence of such phenomena. Orion BN/KL is a near and very interesting star forming region that shows a wide and enigmatic outflow that is assumed to be produced by an explosive event triggered by the close encounter of several forming stars. It is also one of the most chemically diverse regions.

Orion BN/KL is the nearest star forming region which allow us to determine its characteristics comparing the observation with theoretical models. However, the age, energy and the mechanism that produces this kind of outflows are not completely understood, since the models are barely including the complexity of the region. To describe the dynamics of the object numerical simulations are needed. The simulations should include hydrodynamics and chemical network solvers to reproduce, in abundance and spatially, the chemical species observed. Moreover, the simulations of a massive star forming cloud that suffers a non-hierarchical decay could lead to a better understanding of the constraints in the ejection mechanism, probing that a powerful and extended outflow, such as that observed in Orion, can be produced.

In this work we analyze, mainly three physical aspects of Orion BN/KL: The age of the “explosive” event, the physical conditions of the clumps at the time of their ejection, and the molecular CO distribution. To do that, we study the dynamics of the extended outflow driven by a filamentary structure known as the Orion Fingers and the chemical species distribution, specially the CO distribution, emission and velocities. For the first part we propose a new analytic model based on the mass loss of a high velocity clump moving in the interstellar medium. This model was compared with numerical simulations that include a molecular cooling. This model can be used in different astrophysical scenarios to constrain the dynamics of jets and outflows. Also, we have created and implemented KYMIA, a new chemical

network solver, that uses the local physical conditions in the creation and destruction of a selected chemical reactions network, coupling the results to a hydrodynamical solver. This code has been compared with zero-dimensional solvers and laboratory results. Finally the CO outflow is explained as a consequence of the motion of the high velocity clumps, that excite the molecular material that is perturbed by the transverse shock wave.

We have reconciliated the age of the H<sub>2</sub> outflow, assuming a deceleration effect of the ejected clumps, and the CO outflow, with a very characteristic “Hubble” law, as the product of a single event that was produced by the ejection of dense clumps impulsed by the close interaction of protostellar objects in a young cluster.

# Chapter 1

## Orion BN/KL

The Orion Complex is formed by numerous objects as the Great Orion Nebula M42, De Mairan Nebula M43, and the Horsehead Nebula in IC 434. The big scale maps of the Orion Complex, particularly in the  $^{12}\text{CO}$  transition  $J=1\rightarrow 0$  at 2.6 mm (Tucker et al., 1974), reveal a very extended molecular emission produced by two molecular complexes. The northern molecular complex is a region associated to the dark cloud L1630 that extends about four degrees in direction north-south from the Horsehead Nebula, NGC 2023 and NGC 2024 (Orion B) to the nebulae NGC 2068 and NGC 2071. The southern molecular complex corresponds to the dark clouds L1640, L1641 and L1647 (Kutner et al. 1977) and it extends to about six degrees to the south of the Orion Nebula (NGC 1076, Orion A). This complex is elongated, parallel to the Galactic Plane and it is subdivided in three regions of neutral material: OMC1, which is the molecular cloud associated to the HII region M42; OMC2, that is related to the HII region M43, and OMC3, located  $16'$  at the north of OMC2.

The Orion region is the closest star forming region at 414 pc (Mentel et al., 2007) making possible to perform several pioneering observations between the 60's and the 70's. A more recent distance determination locates Orion at 388 pc (Kounken et al., 2017). In fact, during these decades, Becklin & Neugebauer (1967) and Kleinmann & Low (1967) discovered the first protostar candidates in observations in the 1.5 and 22  $\mu\text{m}$  wavelengths. Inside OMC1 is the star forming region Orion Becklin-Neugebauer/Kleinmann-Low region (Orion BN/KL, Becklin et al., 1967, Kleinmann et al. 1967). Orion BN/KL shows an enigmatic outflow that is poorly colimated and it could be produced by the rupture of a forming star cluster. Orion BN/KL belongs to a totally new family of molecular outflows and is not related with the classic bipolar jets produced in the star forming processes (Zapata et al., 2017).

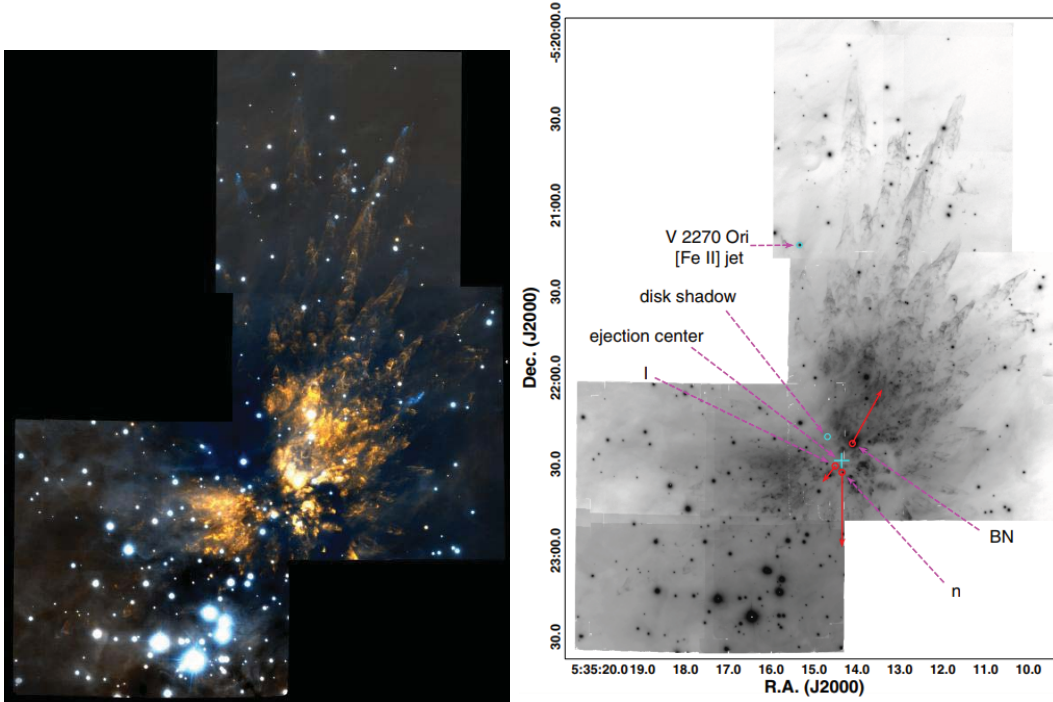


Figure 1.1: Orion BN/KL region. The left panel shows H<sub>2</sub> emission in yellow and [Fe II] emission in blue. The extended outflow and the Orion fingers are very well defined. In the right panel, in the same scale, the cross represent the possible origin of the interaction of the objects BN, n and source I. The lengths of the red-solid vectors are proportional to the motions of these objects (Bally et al., 2015)

Despite being a small region inside the OMC1 in the Orion Nebula, Orion BN/KL has a diameter of 2'. It is located at 1' to the northwest of the Trapezium cluster and its location coincides with the center of OMC1, the molecular cloud associated to the H<sub>2</sub> region M42. It has a size such that many observations in the past had an angular resolution similar to the entire region. Even when almost all protostellar outflows seem to be impulsed by jets and colimated winds (Reipurth et al., 2001), Orion BN/KL shows the distribution of a very wide outflow. Near infrared images reveal hundreds of individual shocks in [Fe II] and H<sub>2</sub> that have almost any direction (Kaifu et al., 2000). The high excitation species, like 1.64  $\mu\text{m}$  [Fe II], are tracers of the shock fronts and are called "bullets", and the filamentary structure traced by the H<sub>2</sub> emission define the so called "fingers", as in Figure 1.1. Since their discovery by Taylor (1984), the Orion Fingers had been mapped by several authors in H<sub>2</sub>/IR emission. Until recently, the origin of the outflow has been more discussed than the origin of the fingers. In the recent past, many authors have analyzed several characteristics of the fingers.

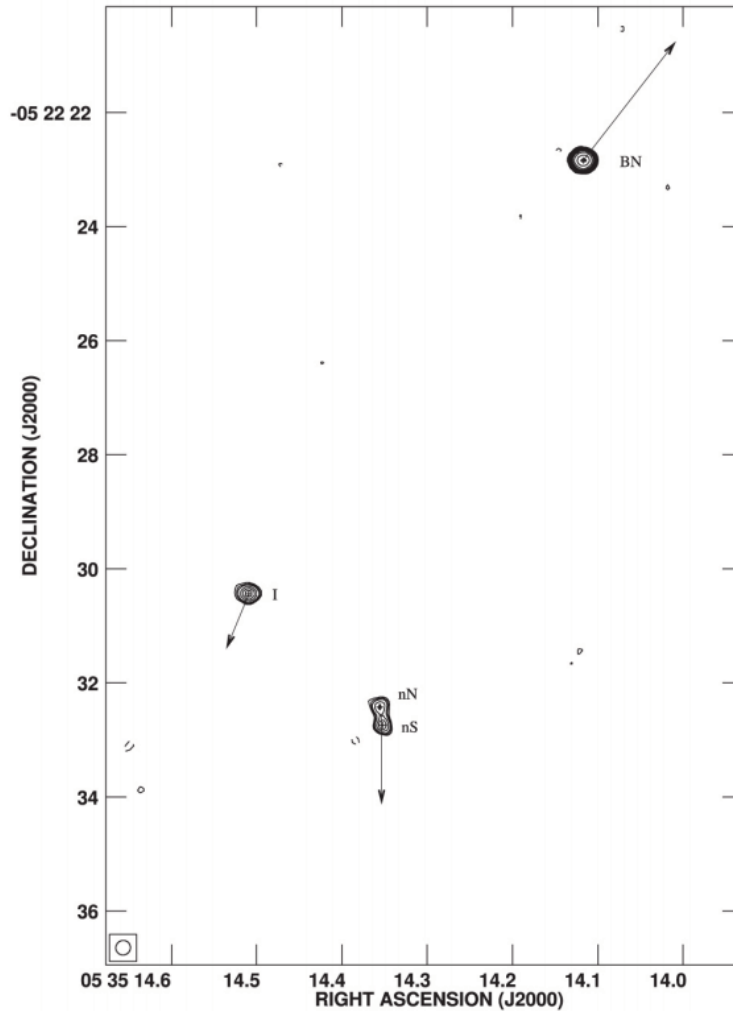


Figure 1.2: Proper motions of objects BN, n and source I. The closest encounter of these objects was produced 544 yr ago. (Rodriguez et al., 2011)

The  $\text{H}_2$  emission, even when it is not colimated, can be considered bipolar, with its axis in the southeast-northwest direction (redshifted-blueshifted). It contains around  $8 M_{\odot}$  of accelerated gas with a median velocity of  $20 \text{ km s}^{-1}$ . The momentum and kinetic energy of these outflows is at least  $160 M_{\odot} \text{ km s}^{-1}$  and between  $4 \times 10^{46}$  and  $4 \times 10^{47}$  erg (Snell et al., 1984 and Kwan & Scoville 1976, respectively).

The OMC1 center shows many infrared sources inside Orion BN/KL. From numerous observations (Reike et al., 1973, Downes et al. 1981, Gezari et al. 1998) with high angular resolution there have been detected several sources, such as sources n, IRc1, IRc2 and source

I. The source n, discovered by Lonsdale et al. (1982), is located just at the center of the H<sub>2</sub>O maser studied by Genzel et al. (1981), 3'' away from IRc2 (Robberto et al. 2005). There is an extended emission detected perpendicular to the principal axis of the source at 8 and 11.7  $\mu\text{m}$ . Shuping et al. (2004) suggested that source n is at the center of a bipolar cavity created by the same outflow as masers observed in this region. Besides that, the presence of a compact H II region suggests that source n is an early type star with a luminosity around 2000 L<sub>⊙</sub> (Greenhill, et al., 2004), which corresponds to a B type star.

The source IRc1, also known as the BN object was discovered by Becklin & Neugebauer (1967). It is the most brilliant source in the region at less than 20  $\mu\text{m}$  wavelengths (Scoville et al., 1983). They thought that BN was a protostar, but recent interpretations associate it to a type B star deeply embedded in the maternal cloud. Also, highly reddened hydrogen recombination lines emission (Grasdalen et al., 1976, Joyce et al. 1978) indicates that the BN object is associated with a compact HII region.

Orion Source I is a young stellar object (YSO) candidate, and is probably a binary system (5 – 7M<sub>⊙</sub>: Plambeck & Wright 2016; 15 M<sub>⊙</sub>: Ginsburg et al. 2018). Source I has been proposed as the origin of the outflow observed in the Orion BN/KL region (Wright et al., 1996, Greenhill et al. 1998, Bally & Zinnecker, 2005) but the real origin is still at debate. Rodriguez et al. (2005) proposed that sources I, BN and n had a very close encounter almost 500 years ago, which resulted in the ejection of the interacting sources and the formation of a binary system in source I. Based on a study of the proper motions at 8.4 GHz, Gómez et al. (2008) proposed that sources I, BN and n, participated in the same dynamic interaction about 500 years ago and actually, the three sources are moving away from the supposed center of the interaction, with velocities of 6, 8 and 12 km s<sup>-1</sup> respectively for sources I, n and BN. According to Zapata et al. (2009), the energy released in such encounter could be enough to power the high velocity outflow in the NW-SE direction. Rodriguez et al. (2017) found that this encounter was produced 544 years ago (Figure 1.2).

Unfortunately, the effect of this type of interaction is still unknown. Tan (2004, 2008) proposed an scenario for the interaction of the sources BN and I. A close encounter could originate accretion by tidal forces and, subsequently, it originates an explosion and pushes away material of the accretion, forming the high velocity outflow. This excludes the possibility that source I formed a binary system during the 500 years after the interaction with

BN. Therefore, source I was a binary system before this interaction and then, at the closest distance of BN and I of about 50 au, the original circumbinary disk of source I was truncated.

On the other hand, Bally et al. (2011) has proposed a qualitative model to explain the dynamic ejection of massive stars in OMC1. This event started a few thousands years ago when a massive star system or a massive binary formed the OMC1 core. This model included simulations that can account for the distribution of sources I, BN and n, Nevertheless, those models cannot explain the structure and chemical properties of the high velocity outflow.

Bally et al. (2015) have numerically simulated high density,  $n_{cl} = 10^7 \text{ cm}^{-3}$ , and high velocity clumps, with temperature 100 K moving in a low density ambient,  $n_a = 10^3 \text{ cm}^{-3}$ , using code ENZO with an adiabatic equation of state. For simplicity, to generate a material tail, they considered a static clump and a moving environment with  $v_0 = 250 \text{ km s}^{-1}$  and temperature 20 K. They compared their results with the observed fingers: they reproduced the structure and transverse velocity of the observed fingers for simulations with times shorter than 100 years, which was of the order of magnitude of the cooling time. Also, the environment density was several orders of magnitude lower than the observed, only  $\text{H}_2$  emission was simulated. Therefore, more efforts have to be made to understand the dynamics of fingers.

Also, the chemistry in Orion BN/KL has a very high molecular diversity. After Sgr B2, Orion BN/KL is the most molecular diverse region and also, is the only known source with a detectable abundance of molecular oxygen (Goldsmith et al., 2011). Allen (1993) reported a non-collimated outflow in the arcminute-scale traced by CO and  $\text{NH}_3$  molecules with emission lines wider than  $100 \text{ km s}^{-1}$ . Feng et al. (2015) spatially resolved the abundance variations in Orion KL for 20 species, including 11 complex organic molecules (COM), and found a difference between the molecular contents in the core and in the post-shock regions.

This region also has an extended CO outflow which was first detected in single-dish observations by Kwan & Scoville (1976). In more recent interferometric observations, this outflow has been resolved into a system of CO “streamers” (Zapata et al. 2009, Bally et al. 2017, Zapata et al., 2017). The CO streamers show a more isotropic direction distribution than the  $\text{H}_2$  fingers. They found a dynamical age of about 500 yr for the extended CO outflow. They also mentioned its impulsive nature, and the different structure with respect to the bipolar jets impulsed by accretion disks and that it is originated from a few arcseconds away from



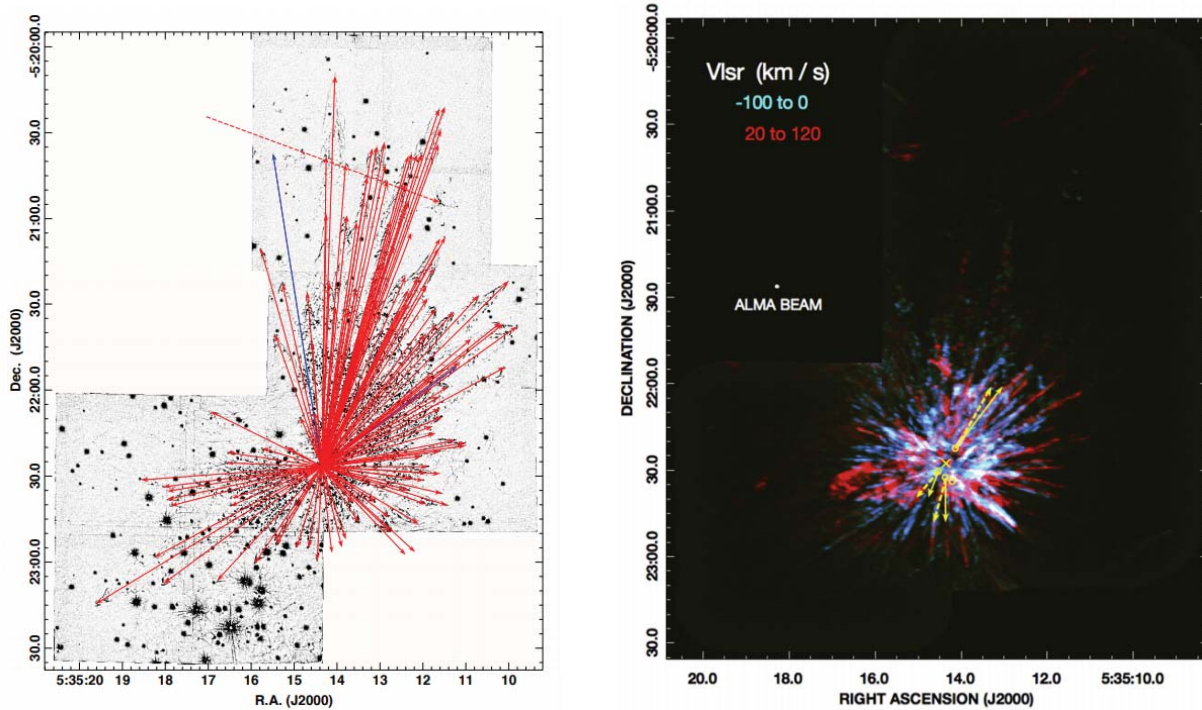


Figure 1.3: The  $\text{H}_2$  fingers are presented in the left panel. The red lines represent the length of each finger. The CO streamers emission, in the right panel, is shorter and more isotropic than the  $\text{H}_2$  fingers

the point of the closest interaction of sources BN, n and I.

Many of the CO streamers partially coincide with the  $\text{H}_2$  fingers, as shown in Figure 1.3, but they do not reach out to the position of the optical “bullets” at the tip of the fingers. Typically, the CO streamers emission fades away at  $0.3 \rightarrow 0.7$  times the length of the corresponding  $\text{H}_2$  fingers. The CO streamers are barely resolved with the ALMA interferometer, with widths of  $400 \rightarrow 800$  au (Bally et al. 2017). Therefore, the CO streams are shorter and narrower than the  $\text{H}_2$  fingers by factors of  $\sim 2$ . As some of the fingers and streamers are spatially coincident and have different widths, it can be argued that the CO emission is produced inside the  $\text{H}_2$  fingers.

Then, in this work, the possibility of a common origin for the fingers and the streamers in a single event is explored, under the assumption that those filamentary structures are the result of the interaction of clumps injected into the interstellar medium produced by the close interaction of the protostellar objects BN, n and I.



## 1.1 Main goals

**To explain the structure, dynamics, physical and chemical abundance conditions of the outflow observed in Orion BN/KL**

### 1.1.1 Particular goals

- **Analyze the dynamics of a dense and high velocity clumps.** The motion of a dense clump has been previously analyzed, but numerical simulations have not implemented cooling mechanisms. We are going to improve the numerical and theoretic description of high velocity clumps, such as the ones that could have originated the Orion fingers.
- **Explain the deceleration of the H<sub>2</sub> fingers, in order to justify the assumption of an origin in a single ejection event** The available observational constraints of the Orion BN/KL region will be applied in an improved dynamical model. The ejection conditions for clumps that formed the Orion fingers will be discussed.
- **Implement a chemical network solver in hydrodynamical simulations**  
To reproduce the observed CO streamers, we have to develop a chemical network solver that can be implemented in hydrodynamical simulations. It has to include an algorithm to select reactions of a database and solve the differential equations of a reactive flow.
- **Reproduce the observed characteristics of the CO streamers using numerical simulations**  
We assume that the CO streamers are formed by the same clumps that form the H<sub>2</sub> fingers. To probe this, we use our numerical code to estimate the CO abundance conditions that can explain observations.

### Modelling Restrictions

The observational constraints are,

#### H<sub>2</sub> fingers

- number  $\sim 200$  (Bally et al., 2011),
- lengths  $10^4 - 10^5$  au (Lee & Burton, 2000, Bally et al. 2011),

- widths  $\sim 3000$  au (Bally et al, 2015),
- proper motions  $\sim 300$  km s $^{-1}$  (Cunningham, 2006),
- H $_2$  heads and wakes, also bullets in [Fe II], [O I]
- dynamical ages  $\sim 500 - 4500$  yr (Cunningham, 2006),
- almost isotropic distribution (Zapata et al, 2017),
- same injection point that ejected BN, I and n runaway proto-stars (Rodriguez et al., 2017),
- total energy  $\sim 10^{47} - 10^{48}$  erg (Snell et al., 1984 and Kwan & Scoville 1976),
- total mass  $\sim 8 M_{\odot}$  (Snell et al., 1984).

### CO streamers

- number  $\sim 50$  (Zapata et al. 2009),
- lengths  $\sim 0.3 - 1$  times H $_2$  length (Zapata et al. 2009, Bally et al. 2017),
- widths  $\sim 400$  au (Zapata et al., 2009),
- radial velocities  $\sim 150$  km s $^{-1}$ , with “Hubble law” acceleration (Zapata et al. 2009),
- H $_2$  fingers related to CO streamers (Zapata et al., 2017),

Our main results are presented in four chapters:

1. **The motion of a losing mass plasmon.** *Published in The Astrophysical Journal, Volume 874, Issue 1, article id. 38, 9 pp. (2019).*

Authors: **Pedro Ruben Rivera-Ortiz**, Ary Rodríguez-González, Liliana Hernández-Martínez, Jorge Cantó

In this chapter we analyze the interaction of a high velocity clump with the static ambient gas using the plasmon model. This model considers a pressure balance between the ram pressure and the internal clump pressure which creates a density stratification in the moving material. Here, we also discuss the mass-loss rate and define two friction terms

$\alpha$  and  $\lambda$ . The values of the friction terms are determined through radiative numerical simulations. Our model can reproduce the position, velocity and mass evolution of a high velocity clump as a function of the ejection velocity and the clump and ambient gas densities.

2. **The ejection conditions of the Orion fingers.** To be send to *Monthly Notices of the Royal Astronomical Society* in June 2019.

Authors: **Pedro Ruben Rivera-Ortiz**, Ary Rodríguez-González, Liliana Hernández-Martínez, Jorge Cantó, Luis Zapata

Orion BN/KL, as mentioned above, is an example of our poor understanding of the mechanism of the close interaction of protostellar objects that produces and destroys a forming stellar cluster. The filamentary structure, the diversity of molecules, the energy involved, the mass of the region suggest that a single event feedbacks the local interstellar medium. This effect could be quantified if there would be information of the frequency and duration of such an event. Using the Orion fingers as a timescale there is a contradiction with the idea of a single event, since each one has an age between 500 and 4000 years. To explain this discrepancy we have used the dynamical model of the losing mass plasmon to find the ejection conditions of a clump. This leads to constrain the initial size, mass and velocity of the Orion fingers.

3. **KIMYA, a code for solving chemical reaction networks in astrophysics.** *Published in Revista Mexicana de Astronomía y Astrofísica Vol. 54, pp. 409-422 (2018).*  
Authors: A. Castellanos-Ramírez, A. Rodríguez-González, **P. R. Rivera-Ortiz**, A. C. Raga, R. Navarro-González, & A. Esquivel

KIMYA is a new code to solve a system of differential equations to describe the time evolution of a chemistry network. In this code we implemented a simple and convergent numerical method and evaluate its precision. KIMYA was designed to implement the solution of a chemical network into multidimensional hydrodynamical simulations. To test our code we have compared it with previous codes using a dark cloud and, also, with a model of nitric oxide formation during a lightning discharge, simulated with a laser pulse. The latter was probed in a single cell simulation and in a 2D hydrodynamical simulation and the results were compared with a laboratory experiment.

4. **Modeling the CO emission of the Orion BN/KL region.** To be send to *Monthly*

*Notices of the Royal Astronomical Society in July 2019.* **P.R. Rivera-Ortiz**, A. Castellanos-Ramírez, A.C. Raga, R. Navarro-González, L. Hernández-Martínez, J. Cantó, F. Robles-Valdez, A. Esquivel & L. Zapata

In this chapter, we present the results of the implementation of KIMYA in the hydrodynamical solver Walicxe 2D to explain the molecular CO outflow that is associated to the Orion BN/KL explosive event. We have considered a chemistry network with 14 chemical species, an atomic and molecular cooling function for the gas and cosmic rays heating. Our simulations explore different parameters, such as the ejection velocities of H<sub>2</sub> clumps, several densities of the interstellar medium and different CO abundances. Using the density, velocity, temperature and emission coefficient for the CO transition J=2→1 we have produced CO maps and position-velocity diagrams. Then we have compared them with observations and found a linear relation between the CO emission and the velocity of the detected transition, which explains the observed Hubble-type law observed.

In Chapter 6 concluding remarks and some considerations which lead to the future of this work are presented. In Appendix D we present the related papers, published and in revision by the authors.

# Chapter 2

## The Motion of a Losing Mass Plasmon

Published in *The Astrophysical Journal*, Volume 874, Issue 1, article id. 38, 9 pp. (2019).

Authors:

Pedro Ruben Rivera-Ortiz, Ary Rodríguez-González, Liliana Hernández-Martínez, Jorge Cantó

*The interaction of a high velocity clump of gas with the interstellar medium has been described by the plasmon model, which considers balance between the ram pressure and the internal stratified structure of the decelerated clump. In this paper we propose an analytical model to describe the mass loss of such a clump due to the interaction with the environment, describing its influence on the plasmon dynamics. We carry out comparisons between an analytic model and axisymmetric gasdynamic simulations of plasmon evolution. From our simulations we were able to find the values of the friction constants  $\alpha$  and  $\lambda$ . Comparing the numerical simulations with the complete analytic model, we can infer the position and the mass loss of a clump as a function of the clump and the environment densities ratio.*

### 2.1 Introduction

The problem of a molecular cloud interaction with a stellar wind has been long studied in the past. De Young & Axford (1967, hereafter DA) described the motion of a clump decelerated by the ram pressure and determined the lifetime of the plasmon. They applied this model to Cygnus A and concluded that analyzing the dynamics of plasmons one can reduce their free parameters. It became a very popular model to explain confinement of radio lobes propagating through the intergalactic medium (Ubachukwu, Okoye & Onuora 1991; Daly, 1994), models

of radio-loud quasars (Daly, 1995) and models of the optical narrow-line regions in Seyfert galaxies (Taylor, Dyson & Axon 1992; Veilleux, Brent & Bland-Hawthorn, 1993). Cantó et al., (1998; hereafter C98) rederived the plasmon solution adding the centrifugal pressure to obtain a modified plasmon profile.

In most cases it is difficult to calculate the real age of an astronomical plasmon since there is no clear information about deceleration and most of plasmons are isolated so there is not enough information about the static medium. To solve this problem one has to consider several plasmons with noticeable decelerations.

Orion BN/KL is an ideal laboratory to prove the plasmon solution, because has an almost isotropic outflow that could be produced by the non-hierarchic close dynamic interaction of a forming multiple-star system (Zapata, 2009). In this region there are more than a hundred filamentary structures known as fingers that allow one to estimate a dynamical age between 1000 years and 500 years, assuming that there was no deceleration. Nevertheless, there is observational evidence that the longest fingers detected in H<sub>2</sub> emission are losing speed (Bally et al. 2011). It is a star formation region that due to its distance, at 414 pc, allows us to determine its characteristics with enough detail. Therefore, we also can study the physics by making theoretical and numerical models, and using observational constrains. Some of these models have achieved important results such as the determination of the dynamical age and the energy of the explosive event. Nevertheless the real age of the event, the mechanism that generates the observed distribution of the fingers, as well as their ejection velocity in the presence of a drag force are still in debate.

The effect of a drag force must be included in order to understand the real motion of a plasmon. Several numerical simulations have shown a deceleration effect greater than the expected by the ram pressure (Yalinewich & Sari, 2016), but it has not been deeply analyzed since cooling effects were not included.

The destruction of the original clump was also considered in Raga et al. (1998) in their study of the interaction of a fast wind impinging a compact spherical cloud. They concluded that the motion is affected by the detachment of material of the cloud, which results in a limited application of their model.

Thus, the assumption that a clump does not decelerate or decelerates according to models with constant a mass, can lead to the overestimated the age of astrophysical outflows.

In this work, we use the DA solution to propose a mass loss rate for a plasmon and obtained the plasmon equation of motion. We compare results of this analytic model with numerical simulations using Orion BN/KL plausible ejection conditions. Analytic (Section § 2.2) and numerical (Section § 2.3) models of clumps deceleration which account for density ratio and the mass loss rate are presented. A comparison between the analytic and numerical models and a prediction for the lifetime of clumps assuming similar conditions to those found in the Orion BN/KL system are presented in Section § 2.4. Finally, we formulate our conclusions in Section § 2.5.

## 2.2 Analytical model

### 2.2.1 De Young & Axford's plasmon

DA studied the problem of a clump of gas moving through an uniform environment. They found a solution (the 'plasmon' solution) based on the balance between the ram pressure of the environment and the stratified thermal pressure of the decelerating clump. For a clump of mass  $M$  with an isothermal sound speed  $c$ , which moves supersonically with velocity  $v$  through a medium of density  $\rho_a$ , the plasmon adopts a pressure and density stratification given by

$$P = P_0 e^{-x/h}, \quad \rho = \rho_0 e^{-x/h}, \quad (2.1)$$

where  $x$  is the distance from the tip of the cloud where the pressure is  $P_0$ , and  $\rho_0 = P_0/c^2$ , where  $c$  is the isothermal speed of sound and  $P_0 = \rho_a v^2$  is the ram pressure of the ambient gas with density  $\rho_a$ .

In Eq. (2.1)

$$h = \frac{c^2}{a}, \quad (2.2)$$

is the scaleheight of the pressure distribution, and  $a$  is the deceleration of the clump.

The balance between the internal pressure and the ram pressure the plasmon as,

$$y = 2h \arctan(e^{x/h} - 1)^{1/2}. \quad (2.3)$$

Then, the mass of the moving clump is,

$$M = \int_0^\infty \pi \rho y^2 dx = \xi_{DA} \frac{\rho_a v^2 h^3}{c^2}, \quad (2.4)$$

where  $\xi_{DA} = \frac{\pi}{2}(\pi^2 - 4)$ .

### 2.2.2 Mass loss rate

We propose a mass loss rate per unit area,  $\mu$ , which depends on the density and the internal sound speed,  $c$ ,

$$\mu = \lambda \rho c, \quad (2.5)$$

where  $\lambda$  is an unknown parameter expected to be less than one. Behind Eq. (2.5), there is the assumption that the clump loses mass at a rate per unit area proportional to the local mass density,  $\rho$ , and with a subsonic velocity  $\lambda c$ . This hypothesis have been proposed and tested, for instance, by Kahn (1980), Cantó and Raga (1991) and Raga, Cabrit and Cantó (1995) in their studies of the turbulent mixing layers produced by the interaction of interstellar outflows. An estimation of  $\lambda$ , in our case, is based in the comparison with our numerical simulations.

The total mass loss rate is given by the integration of  $\mu$  over the surface of the plasmon,

$$\dot{M} = \int_0^\infty \mu dA = \lambda \xi_{DA} \left( \frac{8}{\pi + 2} \right) \frac{\rho_a v_0^2 h^2}{c}, \quad (2.6)$$

Dividing Eq. (2.6) by Eq. (2.4) and using Eq. (2.2) we obtain the differential equation,

$$\frac{1}{M} \frac{dM}{dv} = \frac{8\lambda}{(\pi + 2)c}. \quad (2.7)$$



We can use a dimensionless version of Eq. (2.7) with the following definitions,

$$m = M/M_0, \quad u = v/v_0, \quad \alpha = \frac{8\lambda v_0}{(\pi + 2)c}, \quad (2.8)$$

where  $M_0$  is the initial mass and  $v_0$  is the initial velocity of the plasmon. The solution to Eq. (2.7) then is

$$m = e^{\alpha(u-1)}, \quad (2.9)$$

which relates the plasmon mass with the plasmon speed.

The equation of motion of the plasmon is,

$$\frac{dv}{dt} = -a. \quad (2.10)$$

Solving Eq. (2.4) for  $h$ , Eq. (2.2) for  $a$ , and substituting in Eq. (2.10), we find the equation of motion in a non-dimensional form

$$\frac{du}{d\tau} = - \left( \frac{u^2}{m} \right)^{1/3}, \quad (2.11)$$

where

$$\tau = t/t_0, \quad t_0 = \left( \frac{M_0 v_0}{\xi_{DA} \rho_a c^4} \right)^{1/3}. \quad (2.12)$$

Eq. (2.11), together with Eq. (2.9), has the formal solution,

$$\tau = \int_u^1 u^{-2/3} e^{-\frac{\alpha}{3}(1-u)} du. \quad (2.13)$$

The position  $R$  of the clump after ejection is found by solving the kinematic equation,

$$\frac{dR}{dt} = v. \quad (2.14)$$

Defining  $r = R/(v_0 t_0)$  and combining it with Eq. (2.14), we find the solution

$$r = \int_u^1 u^{1/3} e^{-\frac{\alpha}{3}(1-u)} du. \quad (2.15)$$

Then Eq. (2.9), Eq. (2.13), and Eq. (2.15) give the mass  $m$ , velocity  $u$  and position  $r$  of the clump at a time  $\tau$  after of ejection, as functions of variable  $u$  in the interval  $[0,1]$ .

The clump halts at a finite time  $\tau_f$  and finite distance  $r_f$  with finite mass  $m_f$ . These limits are determined by the condition  $u = 0$  in Eq. (2.9), Eq. (2.13) and Eq. (2.15) and are functions of  $\alpha$  only.

We can find useful approximations in the limits  $\alpha \ll 1$ :

$$\tau_f \simeq 3 \left(1 - \frac{\alpha}{4}\right), \quad (2.16)$$

$$r_f \simeq \frac{3}{4} \left(1 - \frac{\alpha}{7}\right), \quad (2.17)$$

which are consistent with the DA solution. Furthermore, for  $\alpha = 0$  in Eq. (2.13) and Eq. (2.15) we recover the solution of DA.

Also, there are some interesting results concerning the stalling time  $\tau_f$  and distance  $r_f$  that deserve to be highlighted. First, we must notice that independent of the physical characteristics of the original clump (shape, density structure or internal sound speed), the initial interaction with the medium through which it moves will modify these characteristics to those of a plasmon. That is, its shape will be transformed to that given by Eq. (2.3), its pressure and density stratification given by Eq. (2.1) and so on. This transformation is actually accomplished by a reverse shock that moves inside the original clump, changing it into a plasmon.

As we have seen above the structure of the plasmon is highly dependent on its internal sound speed i.e., on its temperature). Let us assume that the temperature of the newly formed plasmon is the one left by the reverse shock that moved through it. For simplicity, let us also assume that this shock is planar and strong. In the Appendix we show that the corresponding isothermal sound speed is,

$$c = v_0 \left(\frac{\gamma - 1}{2}\right)^{1/2} \beta, \quad (2.18)$$

where  $\beta = \sqrt{\rho_a/\rho_{cl}}$  is the square root of the environment and the original clump density ratio.

Using Eq. (2.18) in Eq. (2.8) we find

$$\alpha = \frac{8\lambda}{\pi + 2} \sqrt{\frac{2}{\gamma - 1}} \left( \frac{1}{\beta} \right), \quad (2.19)$$

which is independent of the velocity  $v_0$  and depends only on the ratio  $\beta$ .

Next, let us consider the time  $t_f$  for the clump to stop. It is given by

$$t_f = t_0 \tau_f(\alpha), \quad (2.20)$$

where  $t_0$  is defined by Eq. (2.12) as,

$$t_0 = \left( \frac{M_0 v_0}{\xi_{DA} \rho_a c^4} \right)^{1/3}, \quad (2.21)$$

or

$$t_0 = \left[ \frac{M_0}{\xi_{DA} \rho_a} \left( \frac{v_0}{c} \right)^4 \right]^{1/3} \frac{1}{v_0}, \quad (2.22)$$

and corresponds to the timescale used by DA in their solution to estimate the lifetime of a plasmon (Eq. (2.27)).  $t_0$  can be associated to the lifetime of a plasmon using Eq. (2.20).

As shown in the Appendix (see also Eq. (2.18)) the ratio  $v_0/c$  is only function of the density contrast  $\beta$  and independent of the velocity  $v_0$ . Thus, given the ratio  $\beta$ , the time  $t_0$  and therefore the time  $t_f$  for the clump to stop decreases as the initial velocity of the clump increases. This is an unexpected result: the time to stop a stripping clump is in inverse proportion with its initial velocity. Faster clumps stop earlier independent of their size. Now, let us consider the stopping distance  $R_f$ . This is given by,

$$R_f = v_0 t_0 r_f(\alpha), \quad (2.23)$$

From the discussion above, the product  $v_0 t_0$  results independent of  $v_0$ , and thus  $R_f$ .

Then, clumps with the same ratio  $\beta$  stop at the same distance from the injection point, independent of either their initial velocity or size.

## 2.3 Axisymmetric simulations of plasmon evolution

### 2.3.1 The numerical setup

In order to validate the analytical model, we have computed axisymmetric numerical simulations with the full radiative gasdynamic equations. We used the WALKIMYA 2D code (see Castellanos-Ramírez et al. 2018 and Esquivel et al. (2010)) to perform all numerical simulations. The code solves the hydrodynamic equations and chemical networks on a two dimensional Cartesian adaptive mesh, using a second order finite volume method with HLLC fluxes (Toro et al. 1994).

The adaptative mesh consists of four root blocks of  $16 \times 16$  cells, with 7 levels of refinement, yielding a maximum resolution of  $4096 \times 1024$  (axial  $\times$  radial) cells. The boundary conditions used on the symmetry axis are reflective and the other ones are outflows. The size of the mesh is large enough so that the choice of outer boundaries does not affect the simulation.

The energy equation includes the cooling function described by Raga & Reipurth (2004) for atomic gas and for lower temperatures we have included the parametric molecular cooling function presented in Kosiński & Hanasz (2007),

$$\Lambda_{\text{mol}}(T) = L_1 \cdot T^{\epsilon_1} + L_2 \cdot \exp\left(-\frac{c_*}{(T - T_*)^{\epsilon_2}}\right), \quad (2.24)$$

for  $T < 5280$  K, where,  $\epsilon_1 = 10.73$ ,  $\epsilon_2 = 0.1$ ,  $L_1 = 4.4 \times 10^{-67}$  erg cm<sup>3</sup> s<sup>-1</sup> K<sup>- $\epsilon_1$</sup> ,  $L_2 = 4.89 \times 10^{-25}$  erg cm<sup>3</sup> s<sup>-1</sup>,  $c_* = 3.18$  K <sup>$\epsilon_2$</sup>  and  $T_* = 1$ . K. The total radiative energy for temperatures lower than 5280 K is given by,

$$L_{\text{rad,mol}} = n_{\text{gas}} \cdot n_{\text{CO}} * \Lambda_{\text{mol}}(T) \quad (2.25)$$

where,  $n_{\text{gas}}$  and  $n_{\text{CO}}$  are the number densities of the gas and the CO molecule, respectively.

We have also considered the heating of the gas via cosmic rays, using the heating rate presented in Henney et al. (2009),

$$\Gamma_{\text{crp}} = 5 \times 10^{-28} n_{\text{H}} \text{ erg s}^{-1} \quad (2.26)$$

where,  $n_H$  is the number density of all the hydrogen species.

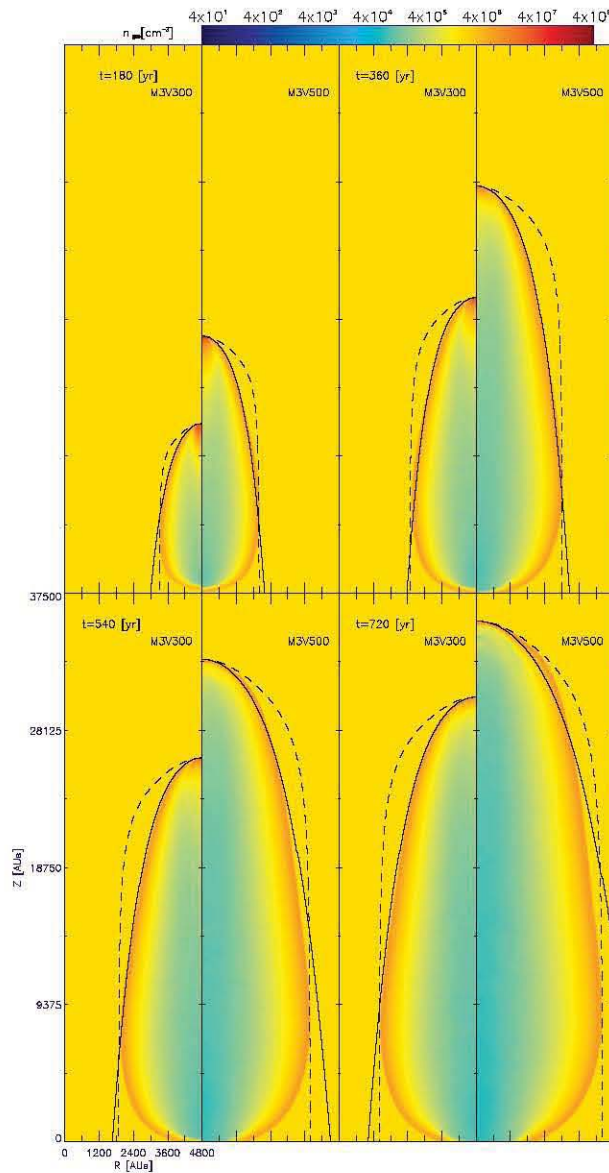


Figure 2.1: Snapshots from the numerical simulations showing the number density. Each panel, with  $4800 \times 37500$  AU, compares two models with initial velocity of 300 (left) and 500 (right)  $\text{km s}^{-1}$  at  $t = 180, 360, 540$  and  $720$  years. Dashed and solid lines present the DA and our analytic solutions, respectively.

### 2.3.2 Numerical models of the plasmon evolution

In order to study the deceleration of a high velocity clump we use parameters compatible with the ejection of Orion Fingers in Orion BN/KL. We have run numerical simulations assuming that the computational domain was initially filled by a homogeneous, stationary ambient medium with temperature  $T_{\text{env}} = 100$  K and various densities (see below). The numerical integration had a domain with physical size of  $48000 \times 12000$  AU on each side, with a maximum resolution (along the two axes) of 11.7 AU.

We carried out time integration from  $t_i=0$  to  $t_f=1000$  yr, and the clump is released at  $z=700$  AU for all models. An estimated initial mass in each of the clumps is  $m_{\text{cl}} = 0.03 M_{\odot}$  since the total mass of the moving gas in the  $\sim 400$  fingers in Orion BN/KL is about  $8 M_{\odot}$  (Bally, 2016). Also, the observed transverse size of the fingers is about 400 AU.

In the numerical models, the initial clump is imposed as a sphere of radius  $R_{\text{cl}}=50$  AU, corresponding to 4 pixels at the maximum resolution of the adaptive grid and with an uniform density  $n_{\text{cl}}=1 \times 10^{10} \text{ cm}^{-3}$ . Since the initial clump is out of equilibrium, it grows to about 400 AU, and then the density structure of a plasmon arises.

We have computed ten models of the clumps, varying the density of the interstellar medium and the velocity at which the clump was injected (see Table 2.1).

Table 2.1: Initial conditions of the numerical models

| Models        | Environment          | clump                  |
|---------------|----------------------|------------------------|
|               | $n_{\text{a}}$       | $v_0$                  |
|               | [ $\text{cm}^{-3}$ ] | [ $\text{km s}^{-1}$ ] |
| M1V300/M1V500 | $1.0 \times 10^6$    | 300/500                |
| M2V300/M2V500 | $3.16 \times 10^6$   | 300/500                |
| M3V300/M3V500 | $1.0 \times 10^7$    | 300/500                |
| M4V300/M4V500 | $3.16 \times 10^7$   | 300/500                |
| M5V300/M5V500 | $1.0 \times 10^8$    | 300/500                |

One of the main hypothesis of our analytic model is that the early interaction of the original clump with the environment will modify its initial characteristics (shape, density stratification or sound speed) to those of a plasmon. The sound speed of the moving clump is calculated

using the internal temperature, which is about 15 K and is close to the sound speed obtained with Equation (A.14) .

In order to illustrate the numerical results, in Figure (2.1) we present the density maps for models M3V300 and M3V500 (left and right panels, respectively) at evolutionary time of 180, 360, 540 and 720 yr, top left, top right, bottom-left and bottom right panels, respectively. The solid lines, in all the panels, are the analytic fit to the plasmon shape (see Eq. (16) and Eq. (17) presented in C98) and the dashed lines are also the plasmon shape's fit obtained by DA in their Eq. (2). In both models, the plasmon shape expected by the DA equation is wider than the shape of the plasmon's head obtained in the numerical simulations. For model M3V500 (the right panels of Figure (2.1)) the plasmon shape proposed by C98 is in very good agreement with the numerical simulations, at least up to  $t \sim 500$  yr. After this time, the plasmon (model M5V300) is rapidly decelerated and the bow shock changes in a different shape that the one proposed by C98. The models with a lower initial velocity (model M3V300) do not have an appreciable deceleration and the numerical shape is in agreement with the C98 prediction.

Other prediction of our model is that the dimensionless mass  $m$  of the clump is related to its dimensionless velocity  $u$  by Eq. (2.9). We can test this prediction. The top panel of Figure 2.2 shows the plasmon position as a function of time for models with initial velocity  $300 \text{ km s}^{-1}$  (see Table (2.1)). The squares, asterisk, triangles, plus and diamond symbols are drawing the results obtained for the models evolving with logarithmic interstellar medium densities of 6, 6.5, 7, 7.5 and 8, respectively. As one can see, the position of the plasmon is smaller for models with denser ambient densities as the deceleration (see middle panel of Figure (2.2)) is larger in models with larger ram pressure (Eq. (A.6)). In the bottom panel of this figure, we present the mass of the clump as a function of time. We calculated the mass considering the gas inside the sphere of 50 AU around the clump center. One can note that the denser interstellar medium produce a larger mass loss rate.

In the same way, Figure (2.3) shows the plasmon position, velocity and mass as functions of time in the numerical simulations with a larger initial plasmon velocity,  $300 \text{ km s}^{-1}$ . The results for the distance, velocity and mass are very similar to those found in the models with initial velocity of  $300 \text{ km s}^{-1}$ . However, the deceleration in the models with initial velocity of  $500 \text{ km s}^{-1}$  is larger than those in the models with  $v_0 = 300 \text{ km s}^{-1}$ , whereas the lifetime of

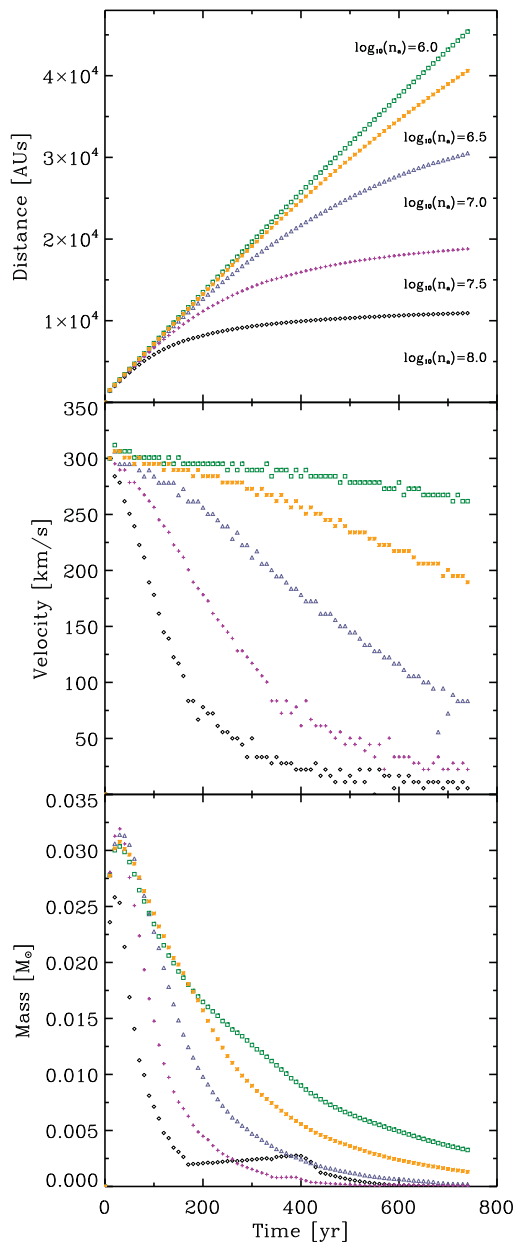


Figure 2.2: The top, middle and bottom panels show the position, velocity and mass as a function of time by the numerical model with initial velocities of  $300 \text{ km s}^{-1}$ , respectively. In each of these panels we plot the results obtained for the models evolving with logarithmic interstellar medium densities of 6, 6.5, 7, 7.5 and 8 using green squares, yellow asterisks, blue triangles, magenta crosses and black diamonds symbols, respectively.



faster clumps is smaller, as we predicted in our Eq. (2.22).

Using the dimensionless mass of the clump and velocity from our numerical simulation in the Eq. (2.13) we fitted the  $\alpha$  value for all numerical models. Figure (2.4) shows the logarithm of the mass of the clump as a function of velocity (dimensionless), for all the models with initial velocity of  $300 \text{ km s}^{-1}$ , we use the same nomenclature for the symbols as in the Figure (2.2), and the solid lines are the fit for the models, M1V300, M2V300, M3V300, M4V300, M5V300 and M6V300.

The  $\alpha$  values for all the models presented here are plotted in Figure (2.5). The plus and diamond symbols are the  $\alpha$  values fitted for models with  $v_0=300$  and  $500 \text{ km s}^{-1}$ , respectively. In order to obtain the value for the constant  $\lambda$  (see Eq. (2.19)), we have fitted the  $\alpha$  values as a function of the density contrast  $\beta$  to our numerical simulation (solid line in this figure). The best fit gives  $\lambda = 0.0615$ . Notice that the  $\alpha$  values are only a function of density contrast and these values are not dependent of the initial velocity or other parameters of the cloud, as described by Eq. (2.19).  $\lambda$  is a constant that is independent of the physical properties of the interstellar medium or gas clump.

## 2.4 Prediction of evolutionary physical properties of the plasmon

The solution for a constant mass plasmon can be found from Eq. (2.13) with  $\alpha = 0$ . The results are,

$$u = \left(1 - \frac{\tau}{3}\right)^3, \quad (2.27)$$

for the velocity, and

$$r = \frac{3}{4} \left[1 - \left(1 - \frac{\tau}{3}\right)^4\right] \quad (2.28)$$

for the position.

Therefore, in the approximation of DA the lifetime of a plasmon is  $t_f = 3 \cdot t_0$  (see Eq. (2.27)). When the mass loss rate is taking into account the plasmon's motion is changed, and the Eq. (2.13) can be integrated numerically to obtain  $u$  and the dimensionless position  $r = x/x_0$  with  $x_0 = v_0 t_0$ . It is important to recall that C98 included the centrifugal pressure, which

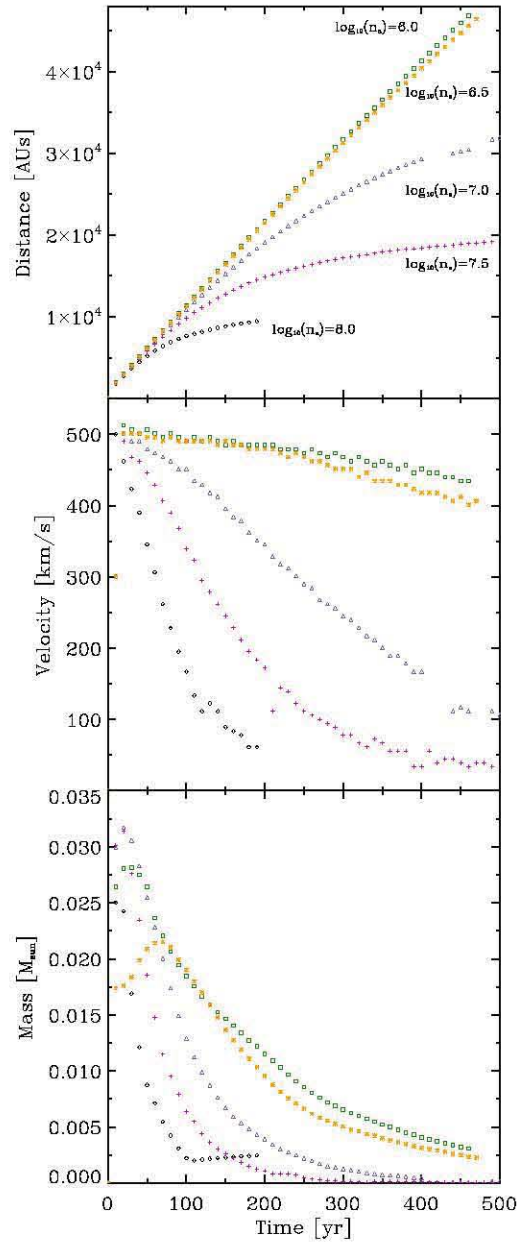


Figure 2.3: The same as Figure 2.2 but for models with initial velocity of  $500 \text{ km s}^{-1}$ .

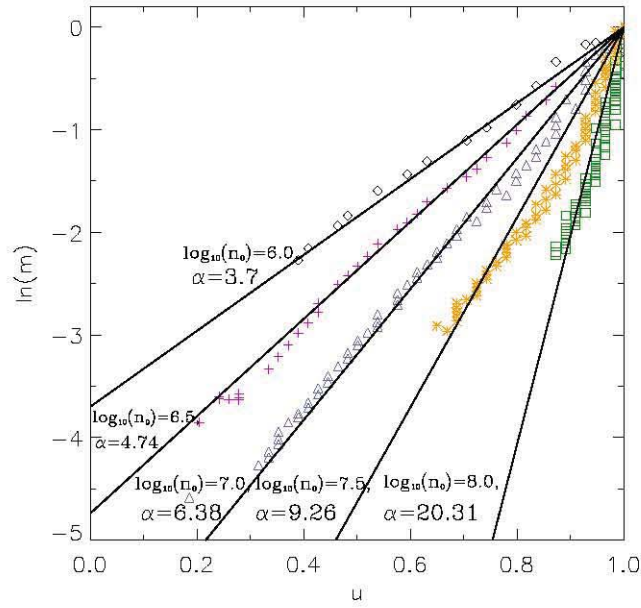


Figure 2.4: Mass of the clump as a function of the clump’s velocity (dimensionless). The nomenclature of the symbols is the same as in the Figure (2.2) and in solid lines we plot the fit for each of the models with initial velocities of  $300 \text{ km s}^{-1}$ .

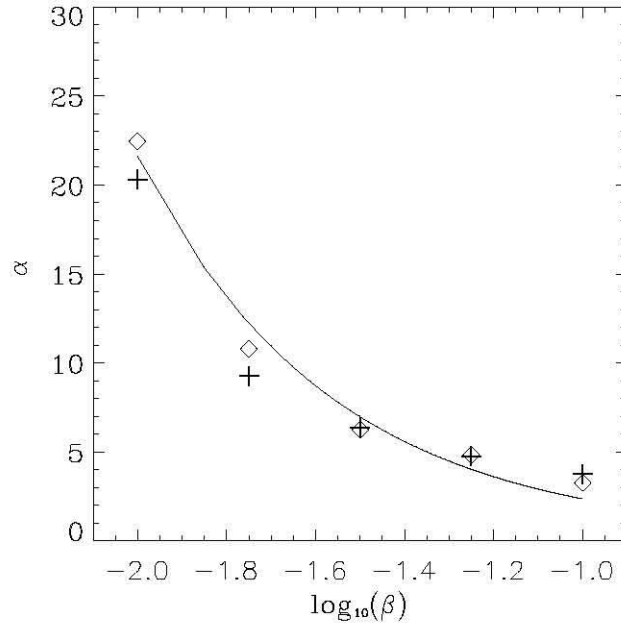


Figure 2.5: The constant  $\alpha$  as a function of density contrast ( $\beta$ ). The plus and diamond symbols are the  $\alpha$  values for models with  $v_0=300$  and  $500 \text{ km s}^{-1}$ , respectively and the solid line is the best fit of  $\lambda$  (see Eq. 2.19),  $\lambda=0.0615$ .

can affect the plasmon shape. This effect was not included in DA neither by us.

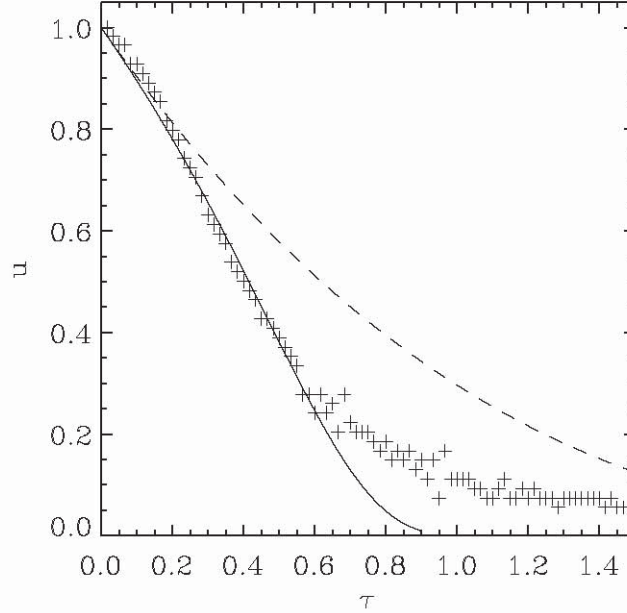


Figure 2.6: Dimensionless velocity,  $u$ , vs dimensionless time,  $\tau$ , for the model with  $\log \beta = -1.25$ . Solid line represents the solution to Eq. 2.13, dashed line is the De Young and Axford prediction in Eq. 2.27 and crosses are the numerical simulation data normalized with  $v_0 = 300 \text{ km s}^{-1}$  and  $t_0 = 600 \text{ yr}$

Finally, we use our numerical simulations to probe our models and their limitations. Each simulation has physical units, so they have to be normalized with  $v_0$ ,  $t_0$  and  $x_0$ .  $v_0$  is obtained directly from the initial conditions,  $t_0$  is obtained from a fit of the velocity data and  $x_0$  comes from a similar fit of the position data.

Figure (2.6) shows the dimensionless velocity as a function of dimensionless time. From this figure, one can see that the DA solution agrees with the numerical results of the model M4V300 only for  $\tau \leq 0.2$  (crosses). However, the semi-analytical solution, solid line is in agreement with the numerical model up to  $\tau = 0.6$ . Notice, that after  $\tau = 0.6$  the values of  $u$ , for the numerical simulation, tends to a constant. There are numerical uncertainties that lead to overestimate the velocity, since, as the plasmon losses mass, it is difficult to determine its position and therefore its velocity.

Figure (2.7) shows the dimensionless position as a function of dimensionless time. The DA

solution, semi-analytic solution and numerical data are represented in this figure. The DA solution is similar to the numerical data for  $\tau \leq 0.4$ , while the semi-analytical solution is in agreement within up to  $\tau \simeq 0.6$ . Note that semi-analytical solution predicts a similar to the numeric stop distance while the DA model predicts a larger distance.

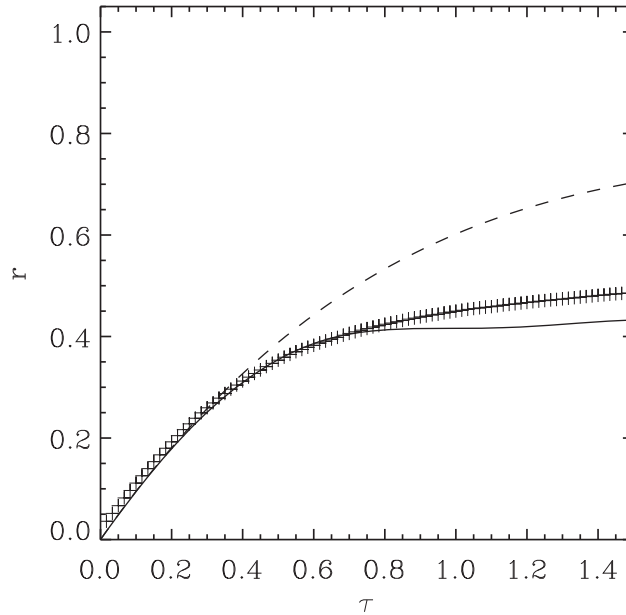


Figure 2.7: Dimensionless position  $r$  vs dimensionless time  $\tau$  for the model with  $\log \beta = -1.25$ . Solid line represents the solution to Eq. (2.13), dashed line is the De Young and Axford prediction in Eq. (2.28) and crosses are the numerical simulation data normalized with  $x_0 = 38000\text{AU}$  and  $t_0 = 600\text{yr}$

Finally, the analytic  $t_0$  and  $x_0 = v_0 t_0$  obtained from Eq. (2.12) and the numerical  $t_0$  and  $x_0$ , for all the models presented in Table (2.2) and Table (2.3) for initial velocities  $300 \text{ km s}^{-1}$  and  $500 \text{ km s}^{-1}$ , respectively.

From the analytical solution, we can see that the final position (the scale length) is only function of the density contrast and it is not related to the clump's initial velocity (see Table 2.2 and Table 2.3). However, the lifetime of the plasmon or clump depends on the initial velocity and the density contrast. The plasmons that were faster initially suffer a larger deceleration.

Table 2.2: Analytic and numerical scale length  $x_0$  and time  $t_0$  for models with  $v_0 = 300$  km  $s^{-1}$ 

| $\log\left(\frac{n_a}{[\text{cm}^3]}\right)$ | Analytical         |               | Numerical         |               |
|--|--------------------|---------------|-------------------|---------------|
|  | $x_0$<br>[AU]      | $t_0$<br>[yr] | $x_0$<br>[AU]     | $t_0$<br>[yr] |
| 6  | $1.14 \times 10^6$ | 18369         | $1.2 \times 10^6$ | 18400         |
| 6.5  | 363868             | 5868          | 200000            | 3000          |
| 7.   | 117000             | 1900          | 90000             | 1400          |
| 7.5  | 38231              | 616           | 38000             | 600           |
| 8  | 12762              | 205           | 18000             | 250           |

Table 2.3: Analytic and numerical scale length  $x_0$  and time  $t_0$  for models with  $v_0 = 500$  km  $s^{-1}$ 

| $\log\left(\frac{n_a}{[\text{cm}^3]}\right)$ | Analytical         |               | Numerical         |               |
|--|--------------------|---------------|-------------------|---------------|
|  | $x_0$<br>[AU]      | $t_0$<br>[yr] | $x_0$<br>[AU]     | $t_0$<br>[yr] |
| 6  | $1.14 \times 10^6$ | 11022         | $1.1 \times 10^6$ | 10000         |
| 6.5  | 363868             | 3500          | 300000            | 2700          |
| 7.   | 117000             | 1134          | 90000             | 850           |
| 7.5  | 38231              | 370           | 40000             | 400           |
| 8  | 12762              | 123           | 19000             | 165           |

## 2.5 Conclusions

We have used the plasmon solution obtained by DA and the solution presented in C98 to propose an analytical solution of the plasmon's deceleration when the mass loss is considered.

This leads to interpret the plasmon mass as a function of the plasmon velocity and relate them by a constant  $\alpha$ . This  $\alpha$  can be interpreted as a friction coefficient. We calculate its dependence on the density contrast between the plasmon and the surrounding environment.

Several numerical simulations were performed trying to compare the validity of our analytic model. This led to  $\lambda = 0.0615$ .

The lifetime obtained from the simple plasmon model is greater than the expected by our losing mass considerations. The deceleration obtained in this method is more likely to be responsible for the age discrepancy in astronomical such flows as the Orion fingers. Also, it is

important to notice that plasmons with greater ejection speeds have shorter lifetimes, which can be also observed in numerical simulations. The final length of a plasmon is not related to its shape and depends on the initial conditions.

Finally, the losing mass plasmon model has proved to be a useful approximation to describe the motion of a high velocity clump in the interstellar medium. In the next chapter, we use the observational constrains of Orion BN/KL in this model to obtain the initial ejection conditions for the clumps that generate the Orion Fingers in Orion BN/KL.





# Chapter 3

## The Ejection Conditions of the Orion BN/KL fingers

Sent to the *Astrophysical Journal* in June 2019

Authors:

P.R. Rivera-Ortiz, A. Rodríguez-González, L. Hernández-Martínez, J. Cantó, L. A. Zapata.

*Orion BN/KL is an example of a poorly understood phenomena in star forming regions involving the close encounter of young stellar objects. The filamentary structure, the great variety of molecules observed, the energy involved in the event and the mass of the region suggest a contribution in the chemical diversity of the local interstellar medium. Nevertheless, the frequency and duration of other events like this have not been determined. In particular, the Orion fingers have kinematical ages between 500 and 4000 yr, which is in contradiction with the idea of a single event. In this paper we explore a recent analytic model taking into account the interaction of a clump and the environment and the resulting deceleration to explain the age discrepancy of the Orion fingers and to infer the initial conditions of the explosion and estimate a lifetime for the region.*

### 3.1 Introduction

Orion BN/KL is a very interesting star formation region that is associated to an explosive event that is poorly understood. In particular it contains around 200 hundred filamentary structures in H<sub>2</sub> emission known as the Orion fingers, which could be formed by the close

encounters of young stellar objects (Zapata et al. (2009), Bally et al. (2011) and references therein). The most accepted interpretation of these fingers is that they were formed by the interaction of high velocity gas clumps with the environment. We will consider this interpretation.

The age of the event has been determined by several authors using different techniques. Bally et al. (2011) analyzed the projection of the heads of the H<sub>2</sub> fingers position and velocity. For each finger, they found an individual age that is between 1000 and 500 yr. This is in contradiction with the idea that Orion BN/KL was produced in a single explosive event and that the expelled clumps are in ballistic motion, so they concluded that there must be some deceleration. Zapata et al. (2009) reported another filamentary outflow observing the J= 2 → 1 CO transition, called CO streamers, which can be associated to H<sub>2</sub> fingers. Each streamer has a radial velocity that increases linearly with the distance to a common origin and, assuming a simultaneous ejection, they determined the 3D structure and obtained a most probable age of approximately 500 yr. This is in agreement with the age estimated by Rodríguez et al. (2017), who used the proper motions and projected positions of the runaway objects I, n and BN to estimate a close encounter 544 years ago. Also, Zapata (2011) calculated the age of a expanding bubble in <sup>13</sup>CO centered in the same possible origin of the region. The radial velocity and the size of this outflow result in ~ 600 years. The momentum and kinetic energy of this outflow is at least 160 M<sub>⊙</sub> km s<sup>-1</sup> and 4 × 10<sup>46</sup> and 4 × 10<sup>47</sup> erg (Snell et al. 1984 and Kwan & Scoville 1976) .

There is a chance that the fingers could be originated at different moments. Perhaps, there is an unexplored mechanism to produce such an extended structure. The machine-gun model has been mentioned as a possible explanation, but previous models (Raga & Biro, 1993), even when they are not collimated, are far from being as isotropic as the Orion fingers. Then, the runaway stars (Rodríguez et al. 2017), the expansion of the hot core (Zapata et al. 2011) and the age determined by the CO fingers (Zapata et al. 2009), are strong evidence of a single and simultaneous event.

There are several attempts to describe the interaction of a moving cloud against a static medium. De Young & Axford (1967) (hereafter DA) analyzed the plasmon problem, which consists in a moving cloud that adopts a particular density structure, and derived its equation of motion. Cantó et al. (1998) improved the plasmon solution including centrifugal pressure.

Also, Raga et al. (1998) proposed the equation of motion of a static spherical cloud that is accelerated with a high velocity wind due to the ram pressure. More recently, Rivera-Ortiz et al. (2019) (hereafter RO19) proposed a modification to the plasmon problem, considering the mass lost by the clump, which can modify a plasmon dynamic history if it is embedded in a high density environment.

Then the dynamical analysis of the motion of the Orion fingers could lead to a better understanding of the conditions that formed such a structure. Bally et al. (2015) performed numerical simulations of the fingers using observational restraints and obtained a notable resemblance to the actual fingers. Nevertheless, as they described, the interpretation of such simulations is limited since they used an adiabatic system, while the cooling length is much shorter than the total length of the longest fingers. Therefore, more detailed numerical solutions and an adequate analytic model can be helpful to determine the physical conditions and, perhaps, the ejection mechanism of the fingers, which can be helpful to understand the relevance and duration of similar events in the star forming processes.

Then, adopting an age of  $t = 544$  yr (see Rodríguez et al. 2017), we propose a model to obtain the physical conditions of the ejection. The mass-loss plasmon has an implicit dependence on its own size and it can be used to find better restrictions on the ejection mechanism. In Section 3.2, we present the sample of objects to be analyzed, in Section 3.3, we present the estimation of the properties for the clumps before the explosive event that generated the Orion fingers in Orion BN/KL. Finally the conclusions are presented in Section 3.4.

## 3.2 Observations

From Lee & Burton (2000), Doi et al. (2002) and Bally et al. (2011) we have obtained the proper motion of several features and the projected positions for the reported data.

Lee & Burton (2000) analyzed the proper motions of 27 bullets, with emission in [Fe II], and 11 H<sub>2</sub> knots, using a time baseline of 4.2 yr (see Figure 3.1). From these 38 objects only 19 have proper motion vectors aligned with the position vectors with respect to IRc2, the possible origin of the explosive event. They used a distance to the Orion Nebula of  $d = 450$  pc (Genzel & Stutzki, 1989), that is larger than the actually accepted  $d = 414$  pc (Menten et al., 2007) which leads to overestimate the projected distance and proper motion of the data. We have corrected this effect for this paper. In

general, they conclude that the farther features have larger proper motions, which is consistent with, at least, some kind of impulse with an age shorter than 1000 yr. However, it is interesting to note that they reported some  $\text{H}_2$  knots as almost stationary, but these are not included in the final analysis.

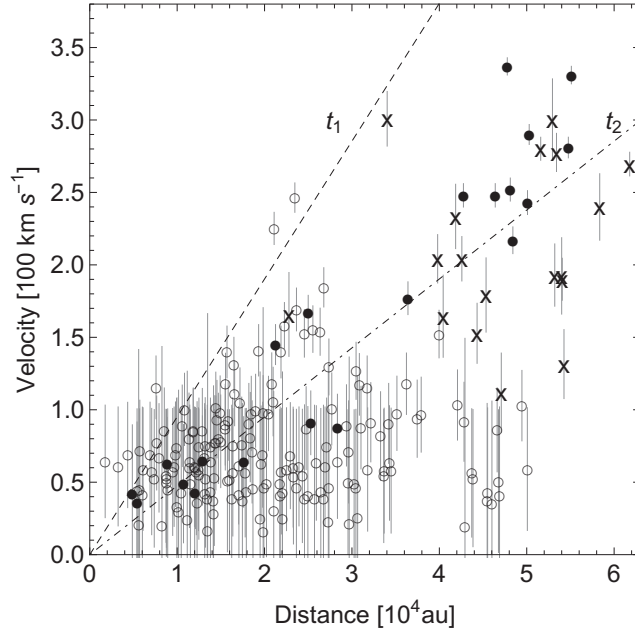


Figure 3.1: This figure shows the three data sets used for this work, with their respective uncertainties. The open circles stand for the  $\text{H}_2$  fingers reported by Bally et al. (2011) (see also, Cunningham (2006)), the filled circles stand for the  $[\text{FeII}]$  bullets (Lee & Burton, 2000) and the crosses represent the HH objects reported by Doi et al. (2002). The lines indicate an age consistent with no deceleration,  $t_1 = 500$  yr (dashed) and  $t_2 = 1000$  yr (dot-dashed).

Doi et al. (2002) measured the proper motions of several HH objects in the Orion nebula. For the Orion BN/KL region they found 21 HH objects moving away from IRC2. As Lee & Burton (2000), they found that the larger objects are faster. The uncertainties lead them to fit an age of  $1010 \pm 140$  yr. Even in this case, several objects are not in the range of 870 to 1150 yr. Also, they used a distance of 450 pc, that has been corrected in this work to 414 pc.

Bally et al. (2011, see also Cunningham 2006) obtained the proper motions of 173 fingers in  $\text{H}_2$ , but in this case there is no clear evidence for a linear dependence of the velocity on the projected distance. They only mentioned that the age of the event could be between 500 and 1000 yr, if the simultaneous ejection assumption is maintained. The three data sets are represented in Figure 3.1.

Also, Zapata et al. (2009) analyzed the CO streamers that seem to be related to the fingers. These streamers are  $\sim 2$  times shorter and narrower than the fingers and each one follow a Hubble type

law. The kinematic age of each one could be related to the projection angle with respect to the plane of the sky, and assuming that the explosion was isotropic they found that the most probable age is around 500 yr. Bally et al. (2017), using ALMA, found more streamers and confirmed that these streamers have an isotropic extension. This means that some of the CO streamers do not have associated fingers.

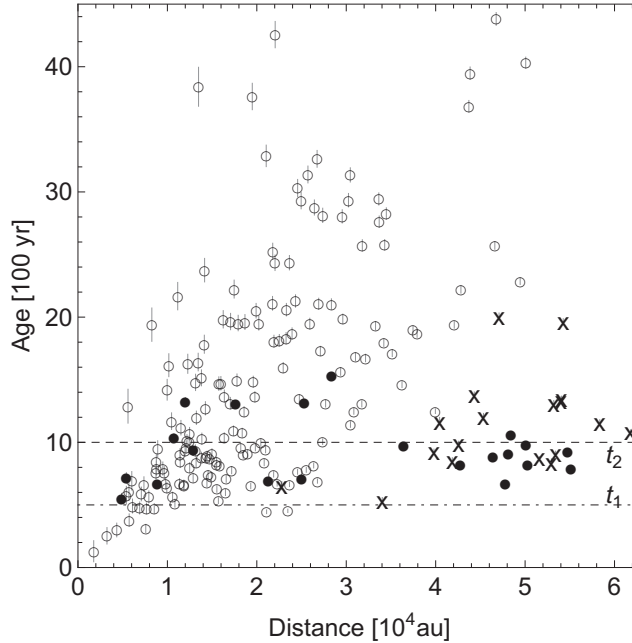


Figure 3.2: Kinematic age assuming no deceleration. The symbol notation is the same as in Figure 3.1. The dashed line correspond to an age of 1000 yr and the dot-dashed line represents an age of 500 yr.

Recently, Rodriguez et al. (2017) has measured, with high precision, the proper motions of the objects I, BN and n. They found that these objects had to be ejected from a common origin  $544 \pm 6$  yr ago. In this work, we assume this event to be the origin of the ejection of the material that created the fingers and the streamers.

Cunningham (2006) measured  $8 M_{\odot}$  as the mass of the moving gas. We can use this estimate to find the upper limits for either the mass of an individual clump, or its size.

For the mass, we assume that the observed moving gas corresponds, exclusively, to that of the ejected clumps. Since there are 200 fingers, then the average mass of each clump is simply  $8/200 = 0.04 M_{\odot}$ . An inferior limit for the clump mass is that calculated by Allen & Burton (1993) and Burton & Allen (1994) of  $10^{-5} M_{\odot}$  based on the [Fe II]  $1.64 \mu\text{m}$  line flux and size.

On the other hand, an upper limit for the size of the initial clump is obtained by adopting the opposite assumption than above, that is, that all the moving mass comes from the swept up environmental material, and, a negligible amount from the clumps themselves. To follow this idea we have to fix the density of the environment. Extinction observations of the region by Oh et al. (2016) and Bally et al. (2017) indicate densities between  $10^5$  and  $10^7$   $\text{cm}^{-3}$ . We adopt this latter limit,  $n_a = 10^7$   $\text{cm}^{-3}$ .

We now model a finger as a cylinder of radius  $R_{cl}$  and individual length  $l_i$ . Thus, the mass swept up by all the fingers (assuming the same radius) is,

$$M_t = \pi R_{cl}^2 \mu m_h n_a \sum_i l_i, \quad (3.1)$$

where  $\mu = 2$  is the mean molecular mass,  $m_h$  mass of hydrogen and  $n_a$  is the numerical density of the ambient medium. Considering, as a limit, that  $M_t = 8 M_\odot$  is equal to the accelerated mass we can obtain  $R_{cl} \sim 90$  au, then this is the upper limit for the initial size of the ejected clumps.

### 3.2.1 Ballistic motion

The simplest model is to suppose that every ejected clump travels with constant velocity and, therefore, the motion is described by:

$$r = vt. \quad (3.2)$$

Since the projected length,  $r$ , and the velocity,  $v$ , also in projection, are observational data, then, the age of each clump can be obtained straightforward:

$$t = \frac{r}{v}, \quad (3.3)$$

which is independent of projection.

Therefore each clump has an individual age and if we assume that all of them were ejected in a single event, each age should be, at least, similar. This is far from which we observe. In Figure 3.2 we show the result of Equation 3.3 applied to each data. The calculation of the spread of the error for the age was done using the standard procedure. The reported errors for the velocities of all the HH objects is  $10 \text{ km s}^{-1}$  (see Doi et al. 2002), of all the  $\text{H}_2$  fingers is the  $25 \text{ km s}^{-1}$  (see Cunningham 2006) and for the [FeII] bullets is reported in Lee & Burton (2000) for each of them. Then, Figure 2

implies that there was no simultaneous event or that the ballistic motion model is not an appropriate assumption. Deceleration is the most likely interpretation.

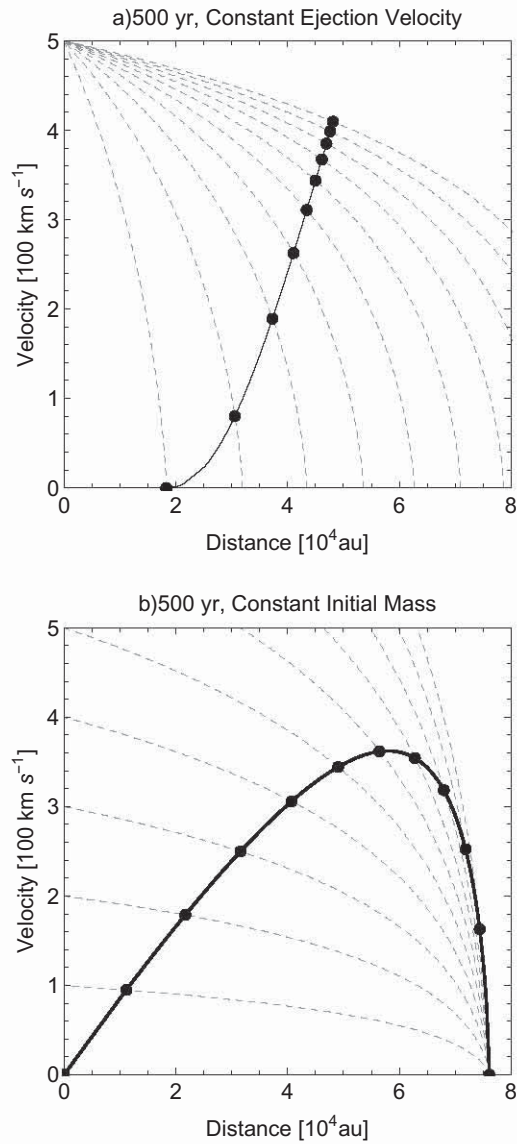


Figure 3.3: In both panels, the gray dashed lines are the trajectories for RO19 plasmons with a) different mass and constant ejection velocity (with a lower and higher mass trajectories of  $2 \times 10^{-2} M_{\odot}$  and  $2 \times 10^{-1} M_{\odot}$ , respectively, divided into 10 equal intervals) and b) different ejection velocities and constant mass (with a lower and higher velocities trajectories from  $100 \text{ km s}^{-1}$  to  $1100 \text{ km s}^{-1}$  with intervals of  $100 \text{ km s}^{-1}$ ). Given a fixed time  $t = 500 \text{ yr}$ , each trajectory reaches a position  $r$  and a velocity  $v$ , marked as a black point in it.



### 3.3 Dynamic model

In order to determine the fundamental parameters that control the dynamics of a high velocity clump, such as the ejection velocity  $v_0$ , the initial size of the clump  $R_{cl}$ , the density of the ejected material  $\rho_{cl}$  and the density of the environment  $\rho_a$ , or their density contrast  $\beta = \sqrt{\rho_a/\rho_{cl}}$ , we use an analysis based on the plasmon proposed by De Young & Axford (1967)

Assuming a spherical clump at the ejection, the initial mass can be expressed as,

$$M_0 = \frac{4\pi R_{cl}^3 \rho_{cl}}{3} = \frac{4\pi R_{cl}^3 \rho_a}{3\beta^2}. \quad (3.4)$$

We assume that every clump was ejected with the same size ( $R_{cl} = 90$  au) and the environment density is  $10^7 \text{ cm}^{-3}$ , therefore we can estimate the ejection conditions.

In this section we explore a model which takes into account the deceleration of the clump as it losses mass due to the interaction with the environment. This is the model developed in RO19. As stated in RO19, no matter the physical characteristics of the original clump (shape, size, density, velocity or temperature) the initial interaction of the clump with the surroundings will transform it into a plasmon as proposed by De Young & Axford (1967) (see also Cantó et al. (1998) and RO19). Mass, on the other hand, is preserved.

RO19 shows that the mass  $M$ , velocity  $v$ , and position  $R$  of the newly created plasmon after a time  $t$  of ejection/formation are given by the parametric form

$$M = M_0 e^{-\alpha \left(1 - \frac{v}{v_0}\right)}, \quad (3.5)$$

$$t = t_0 \int_{v/v_0}^1 u^{-2/3} e^{-\frac{\alpha}{3}(1-u)} du, \quad (3.6)$$

and

$$R = v_0 t_0 \int_{v/v_0}^1 u^{1/3} e^{-\frac{\alpha}{3}(1-u)} du, \quad (3.7)$$

respectively, where  $M_0$  is the initial mass of the clump,  $v_0$  the ejection velocity,  $\alpha$  a parameter given by,

$$\alpha = \frac{8\lambda}{\pi + 2} \sqrt{\frac{2}{\gamma - 1}} \left(\frac{1}{\beta}\right), \quad (3.8)$$

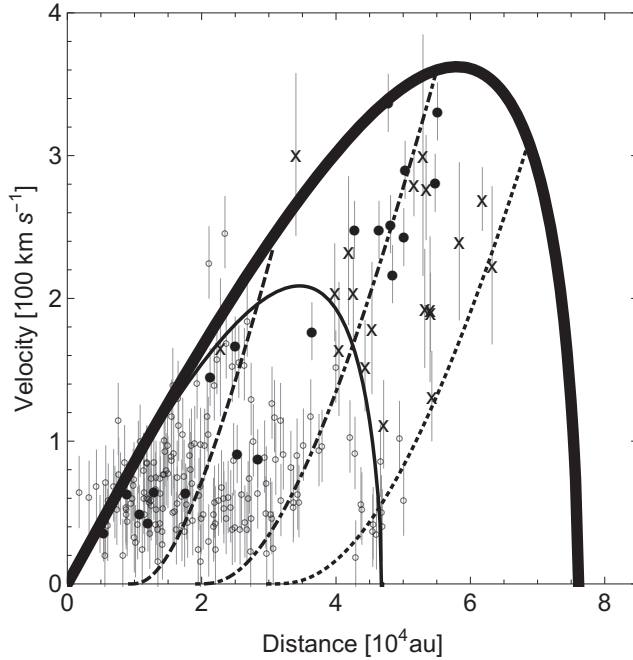


Figure 3.4: In the figure are the data sets described in Figure 3.1, along with the fixed time curves with constant ejection velocities of  $v = 200, 500$  and  $800 \text{ km s}^{-1}$  (dashed, dot-dashed and dotted lines, respectively) and  $M_0 = 0.2$  and  $0.1 M_\odot$  constant mass (black thick and thin lines, respectively) using the RO19 plasmon model

and a scale time  $t_0$

$$t_0 = \frac{R_{\text{cl}}}{\beta^2} \left( \frac{16\pi}{3\xi_{DA}(\gamma-1)^2} \right)^{1/3} \frac{1}{v_0}, \quad (3.9)$$

with  $\xi_{DA} = 9.22$   $\lambda = 0.0615$ , and  $\gamma = 1.4$  is the adiabatic coefficient for an ideal diatomic gas.

Combining Equations (3.8) and (3.9), we obtain:

$$\left[ \frac{v_0}{\text{km s}^{-1}} \right] \left[ \frac{t_0}{\text{yr}} \right] = 233 \left[ \frac{R_{\text{cl}}}{\text{au}} \right] \alpha^2. \quad (3.10)$$

The purpose of the present paper is to use Equations (3.4) to (3.10) to estimate the physical parameters, such as mass, ejection velocity, density, of each of the original clumps that produce the fingers we see today and formed by the interaction of the clumps with the surrounding molecular cloud.

We begin by assuming that all the clumps were ejected in a single explosive event that took place 544 years ago from the place of the closest interaction that expelled BN, n and I objects reported by Rodriguez et al. (2017). So, in Equation (3.6) we set  $t = 544\text{yr}$  for all the clumps, although each clump had their own initial mass and ejection velocity.

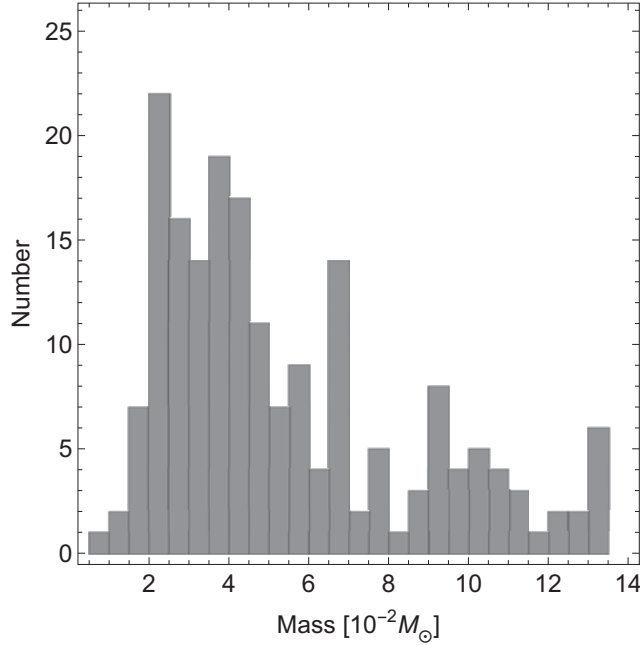


Figure 3.5: The mass of the clumps calculated using the losing mass plasmon model of RO19, for the data set presented in Section 3.2

Next, for each clump we know, from observations, its distance to the origin of the explosion  $R$  and its current velocity  $v$ . Both quantities are those on the plane of the sky. However, we take them as estimates of the real values, since there is no way to de-project them without making further assumptions.

Even so, we need to make a further assumption, since we have more unknowns than equations. We might, for instance, choose to assume a fixed value of  $\beta$ , which means the same initial density for each clump, or, perhaps, the same initial mass, or any other reasonable constrain. We choose, however, to assume a unique initial radius for all the clumps of  $R_{cl} = 90$  au, based on the assumption that all the clumps were produced by the close encounter of two protostellar objects that ripped off material with the same cross section interaction.

Then, we have a set of equations (equations 3.5, 3.6 and 3.10) that can be solved for  $v_0$ ,  $t_0$  and  $\alpha$  simultaneously, and by Equation (3.4) we also can obtain the mass of each ejected clump. The number density of the surroundings was taken  $n_a = 10^7 \text{cm}^{-3}$ . In Figure 3.3 we represent the trajectories of several plasmons in dashed lines with different initial masses and ejection velocities. An important characteristic is that the stopping distance depends on the initial mass.

In Figure 3.4, we can see that the model curves that envelope the data set do not have high mass ( $> 0.2 M_{\odot}$ ) and high velocity clumps ( $> 800 \text{ km s}^{-1}$ ). We could expect slow points with low velocities at a distance greater than  $8 \times 10^4 \text{ au}$ , but there is not any evidence of such clumps but in this case we have that  $800 \text{ km s}^{-1}$  is the fastest velocity that meets the longer features. Also, a plasmon with ejected mass of  $0.2 M_{\odot}$  will reach a final distance of  $\sim 8 \times 10^4 \text{ au}$ . This means that a less massive plasmon, with less velocity than  $800 \text{ km s}^{-1}$  could be near to its lifetime or maybe it has already stopped. This could explain the CO streamers that are not related to any  $\text{H}_2$  finger.

Finally, the RO19 plasmon solution is applied to each of the object of the data sets of the Sect. 3.2 and the initial mass, ejection velocity and lifetime are obtained, Figure 3.5, 3.6 and 3.8, respectively. The total mass, Figure 3.5, is  $11.93 M_{\odot}$  with mean mass of  $0.06 M_{\odot}$  which is close to the limits of  $4 \times 10^{-2} M_{\odot}$  analyzed in Section 3.2.

Figure 3.6 shows the ejection velocity distribution. It is interesting to note that there are 2 peaks in this distribution around  $200$  and  $500 \text{ km s}^{-1}$ . Further analysis is required to propose a mechanism of explosion that could explain this characteristic. Also, the kinetic energy of the model is  $3 \times 10^{49} \text{ erg}$ .

Once that the ejection parameters are obtained, we can infer the lifetime and stopping distance

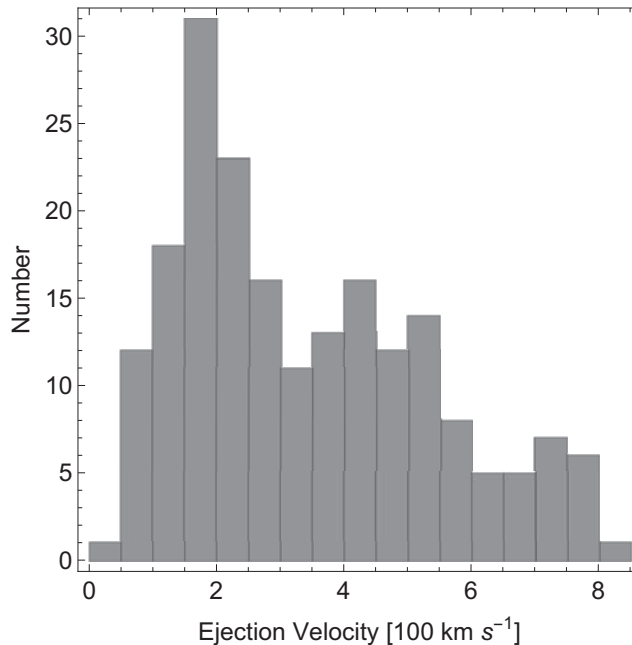


Figure 3.6: Velocity distribution according to the losing mass plasmon model (see RO19), using the corresponding calculated ejection conditions.

of each clump using  $v = 0$  in Equations (3.6) and (3.7). In Figure 3.8 we show the distribution of the lifetime for the clumps. This can give an idea of the lifetime of the explosive event, in this case

2000 yr after the explosion, there will be just a few fingers and this can be reason that there are just a few observations of encounters of this kind.

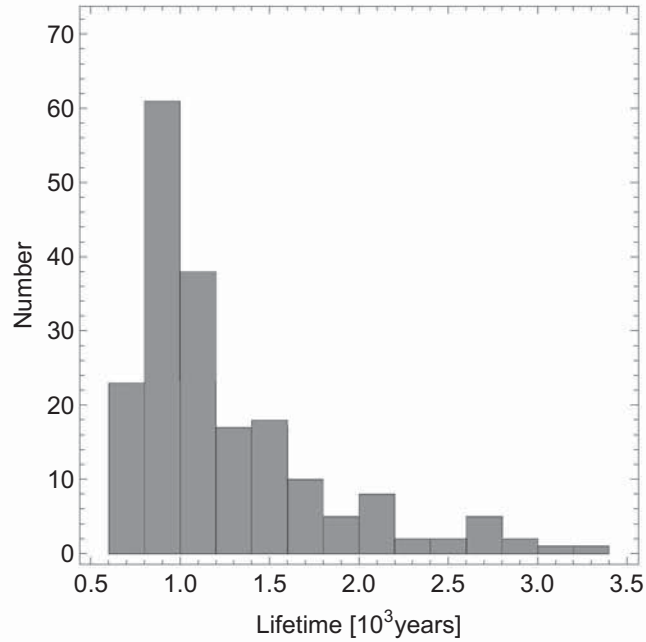


Figure 3.7: Lifetime of each finger (for the sample used in this chapter) using  $R_{cl} = 90$  au.

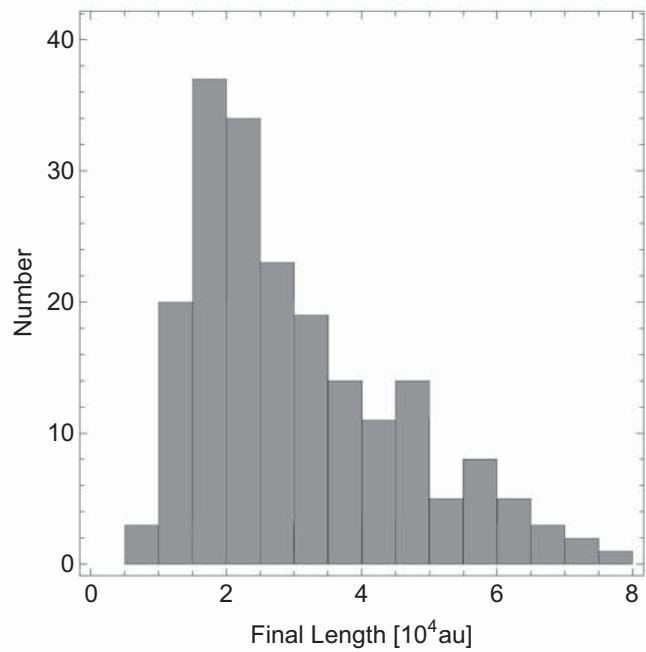


Figure 3.8: Final length of each finger (for the sample used in this chapter) using  $R_{cl} = 90$  au.

Finally, in Figure 3.9 we show the time and position of each clump compared with its own lifetime

and stopping distance, respectively. Again, there is a tendency for most of the clumps to be at the end of their lives. This suggests that maybe some fingers have already ended their lives, explaining that there are  $\text{H}_2$  features with no proper motion and CO streamers with no  $\text{H}_2$  fingers associated.

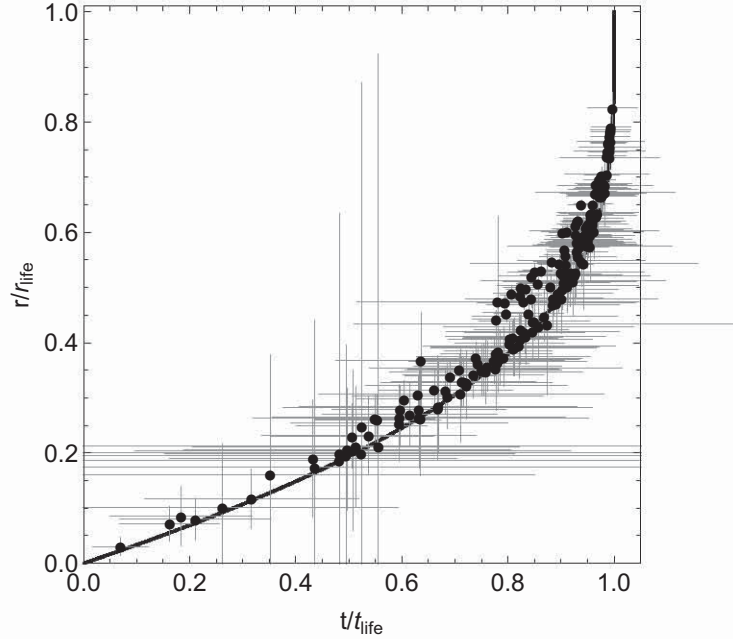


Figure 3.9: Distance normalized with the stopping distance versus time normalized with the lifetime for each data from Figure 3.1. The black line corresponds to the prediction using a  $0.025M_{\odot}$  plasmon.

### 3.4 Conclusions

The plasmon model is a useful tool for the analysis of the dynamics of a clump interacting with a dense environment. Using the dynamic models presented in DA and RO19 we estimate the physical features, initial velocities and masses, for the components (clumps, [FeII] and HH object) reported in Lee & Burton [2000], Doi et al. (2002) and Cunningham (2006) assuming that these components were produced un a single event 544 years ago..

We obtain that the individual maximum mass for the clumps is  $0.2 M_{\odot}$ , but the maximum velocity of this sample is of  $800 \text{ km s}^{-1}$ . The total kinetic energy, in this case, is  $\sim 3 \times 10^{49} \text{ erg}$ , which represents  $10^2$  times more energy than the energy obtained for the total luminosity in the Orion Fingers region.

Other two consequences of the plasmon model is that the larger ejection velocities produce the shorter lifetimes, and the initial mass of a clump determines its stopping distance. The RO19 plasmon predicts that the longest fingers in Orion BN/KL have almost reached their lifetime, but they are not far from their final length and they required ejection velocities as high as  $800 \text{ km s}^{-1}$  to reproduce the observations. This implies that the slower fingers could have lifetimes as long as 3000 yr. The mass-loss plasmon can explain that there are not visible longer fingers because, if there were clumps thrown with higher speed or less mass, they could have died by now. Also, the required ejections velocities for most of the longest fingers are about  $500 \text{ km s}^{-1}$  which is less than twice their observed velocity.

Therefore, using the RO19 model we obtained the initial masses of each of the clumps, from their mass distribution it is observed a large quantity of clumps has a mass in the interval of  $8 \times 10^{-3} - 2 \times 10^{-1} M_{\odot}$  and from the velocities distribution, we obtain a distribution of, at least, 2 populations, one of them with a maximum at  $200 \text{ km s}^{-1}$  and another with a velocity of  $500 \text{ km s}^{-1}$ .

Finally, from our calculated time and position of each clump and their own expecting lifetime we can see a tendency for the most of the clumps to be at the end of their lives. We proposed that some fingers have already ended their lives, it explains that there are  $\text{H}_2$  features with no proper motion and CO streamers with no  $\text{H}_2$  fingers associated.





# Chapter 4

## KIMYA: A chemical network solver

Published in *Revista Mexicana de Astronomía y Astrofísica* Vol. 54, pp. 409-422 (2018).

Authors: A. Castellanos-Ramírez, A. Rodríguez-González, **P. R. Rivera-Ortiz**, A. C. Raga, R. Navarro-González, & A. Esquivel.

*In order to study the temporal evolution of the gas molecular composition, one needs to solve the equation which determines the abundances of the different gas species. This requires to construct a chemical network which describes the creation and destruction reactions for different gas species. KYMIA is a new code that can be implemented in other hydrodynamical solvers. We have tested KYMIA with other codes and experiments.*

### 4.1 Introduction

Chemical kinetics networks have applications in atmospheric chemistry, processes of combustion and of detonations, biological systems and as in the planetary, stellar and interstellar astrophysics.

In order to follow the time-evolution of a chemical system, one needs to determine the reagents and products which are involved, as well as the relevant chemical reactions. The resulting rate equations have to be integrated in time together with the equations that describe the time-evolution of the reactive fluid (these could be the gasdynamic or the magnetohydrodynamic equations in 1, 2 or 3D, which are coupled to the chemical network through the equation of state and possible energy gain/loss terms). The simplest possible model is a “0D” approximation, in which the chemical rate equations are integrated for a single, homogeneous parcel in which either a constant or a time-dependent density (or pressure) and temperature are imposed.

In order to follow the temporal evolution of the gas molecular composition, one needs to integrate the density conservation equations for the different species contained in the gas. In order to do this, one has to construct a chemical network which includes the creation and destruction reactions for all the species. Such a network is a system of ordinary differential equations (ODEs). As initial conditions, we use the density for each species  $n_i(t)$  at the initial time  $t$ . This system must be solved numerically in order to find the densities of each species at a future time,  $n_i(t + \Delta t)$ .

The chemical model may include a large number of species (ranging from  $\sim 10$  to several thousands). The interaction between the species results in a large number of elementary reactions with rates that can, in principle, differ by many orders of magnitude. As a result, chemical networks (see equation 4.2 in Section 4.2) are “stiff” systems of ordinary differential equations, which require special numerical integration methods.

The stiffness of a chemical network was first discussed by Curtiss & Hirschfelder (1952), who noted that the so-called “explicit methods” for solving differential equations failed to solve some chemical reactions (though versions of explicit methods appropriate for stiff systems were later developed, see below). Dahlquist & Lindberg (1973) found that numerical instabilities resulting from the widely ranging evolutionary timescales of the different species are the main reason for the failure of explicit methods in the solution of stiff equations.

There is an extensive literature on the solution of stiff ODEs. The review of May & Noye (1984) gives an introduction to the subject, and the classical book of Gear (1971) describes appropriate numerical methods. Jacobson (2005) gives a review of many different methods for solving stiff equations.

These methods fall into two main categories:

- explicit methods: In this case the solutions are marched forwards in time with the creation/destruction terms (see equation 4.2) evaluated at the current time. Explicit methods appropriated for stiff equations include schemes with partially time-integrated rates and/or logarithmic time-stepping,
- implicit methods: In this case which the creation/destruction terms are evaluated with the time-advanced densities.

While the first type of method is simpler to program and generally faster to compute, all implementations share the complexity of having many adjustable parameters associated with choosing different sub-timestepping schemes which depend on the characteristics of the chosen network. They typically have trouble converging to chemical equilibrium and have to be specifically adjusted for

solving different chemical networks. A well known example of this kind of method is the one described by Young & Boris (1973).

The implicit methods generally have guaranteed convergence to chemical equilibrium, and produce numerically stable (though not necessarily accurate) time-evolutions regardless of the size of the timestep. However, they are computationally much slower than explicit methods, requiring iterations involving the Jacobian of the chemical network equation system. The best known method of this kind is Gear's algorithm, and variations of this algorithm are implemented in many generally used codes (see, e.g., the review of Nejad 2005).

An important part of the chemical network is reliable values for the reaction rates. There are several databases containing experimental and/or theoretical values of the rate coefficients for specific temperature ranges. Examples are presented in the work of Baulch et al. (2005) for combustion, Crowley et al. (2010) for atmospheric chemistry, and Millar et al. (1991) and Wakelam et al. (2012) for astrochemistry.

Summaries of astrochemical codes and astrochemistry databases have recently been given by Semenov et al. (2010), Motoyama (2015) and Ziegler (2016). Since the pioneering work of Bates & Spitzer (1951), many chemical models (and the necessary numerical codes) have been developed. With modern high angular and spectral resolution ALMA interferometer, it became necessary to increase the complexity of astrochemistry simulations. In particular, in order to obtain predictions that can be compared with recent observations it is necessary to compute multi-dimensional models involving both the dynamics of the gas (modeled either with the hydrodynamical or the magnetohydrodynamical equations) and appropriate chemical network. A possibility for reducing the computational time is to consider steady-state chemistry (see Semenov et al., 2010), but in order to obtain realistic results it is necessary to include the full, time-dependent chemistry in simulations of the gas dynamical properties.

An example of this is the code presented by Ziegler (2016). This code solves a chemical reaction network together with the magnetohydrodynamic equations. Also, the recently developed by Grassi et al. (2012) KROME code and the GRACKLE library by Smith et al. (2017) have chemical evolution routines that can be implemented in hydrodynamic/magnetohydrodynamic codes.

Another example is the work of Navarro-González et al. (2010), who developed a chemical evolution code for integrating a set of chemical rate equations in order to predict the degree of oxidation and chlorination of organics in the Martian soil. This code solves the chemical kinetics model using

an explicit method. This code was in good agreement with the results previously reported in others standard chemical kinetics codes (see Navarro-González et al. 2010). Nevertheless, the numerical method used in this code has difficulties converging to the correct solution for particularly stiff reactions networks.

The aim of the present work is to develop a code based on a fast, simple implicit solver for chemical networks, which is appropriate for implementations in multidimensional gasdynamic simulations. We evaluate the accuracy of this solver by computing:

- a single parcel, “dark cloud” model, which we compare with previously published results of this problem,
- a single parcel, and an axisymmetric gasdynamical model of a laser laboratory simulation of a lightning discharge.

The simulations of the laboratory experiment are used to calculate the chemical evolution of an atmospheric, laser generated plasma bubble, which is then compared with actual measurements of the chemical species and their densities. While a few attempts have been done in the past to evaluate the precision of the astrophysical gasdynamic codes through comparisons with laboratory experiments (see, e.g., Raga et al. 2000, Raga et al. 2001 and Velázquez et al. 2001), to the best of our knowledge this is the first time that this type of test is done for an astrophysical chemical evolution and reactive gasdynamics code.

The paper is organized as follows. In Section 4.2 we present the numerical method for solving the chemical networks. We describe briefly the KIMYA code in Section 4.3. The gasdynamic equations together with the reaction network are described in Section 4.4. In Section 4.5 we apply KIMYA to model two phenomena: a dark cloud model, and an experimental study of the formation of nitric oxide during a lightning discharge simulated with a laser pulse. Finally, in Section 4.6 we discuss the proper operation of the code and present our conclusions. In Appendix C we show the algorithm to select the appropriate chemical network and create the reaction equations that are intended to be solved.

## 4.2 The numerical solution of the network chemical rates

A chemical network is described by the system of differential equations:

$$\frac{dn_i}{dt} = \sum \text{formation} - \sum \text{destruction}, \quad (4.1)$$

where  $n_i$  is the density of species  $i$ . The first term in the right hand side contains all the formation processes and the second term all the destruction processes for each specie  $i$ .

If the chemical network involves only binary reactions, we have:

$$\frac{dn_i}{dt} = \sum_{j,k} f_{jk}^{(i)} n_j n_k - n_i \sum_k d_{ik}^{(i)} n_k, \quad (4.2)$$

where  $n_i$  is the density of a species  $i$ , and  $f_{jk}^{(i)}$  and  $d_{ik}^{(i)}$  are the temperature dependent rates of formation and destruction of species  $i$ , respectively. The indices  $i, j, k$ , go from 1 to the total number of species  $N$ .

### 4.2.1 The Newton-Raphson iteration

The set of equations described above can be written, without loss of generality, as

$$\frac{dn_i}{dt} = R_i, \quad (4.3)$$

where  $n_i$  are the densities of  $N$  species (i.e.,  $i = 1, 2, \dots, N$ ).

In order to solve the system of ODEs, we use an implicit method. We do the simplest possible “implicit discretization” of the left hand side of equation (4.3):

$$\frac{n_i - n_{i,0}}{\Delta t} = R_i. \quad (4.4)$$

where  $n_i$  are the densities at a time  $t + \Delta t$ ,  $n_{i,0}$  are the (known) densities at a time  $t$  and  $R_i$  are the source terms associated with the creation and destruction processes evaluated with the time-advanced densities  $n_i$ .

We rewrite equation (4.4) as:

$$Q_i = R_i - \frac{n_i - n_{i,0}}{\Delta t} = 0, \quad (4.5)$$

with  $i = 1, \dots, N$ .

For very large  $\Delta t$ , equation (4.5) gives  $R_i = 0$ , which is the condition for chemical equilibrium. However, this condition is not sufficient for specifying the chemical equilibrium, as not all of the  $R_i = 0$  equations are linearly independent. We therefore only consider a subset of  $p < N$  equations of the form (4.5), eliminating the  $N - p$  equations with  $R_i$  terms which can be written as linear

combinations of the  $R_p$  (with  $p \neq i$ ) terms of the remaining rate equations.

In order to close the system of equations, we then consider a set of “conservation equations”:

$$Q_m = C_m = 0, \quad (4.6)$$

with  $m = p, \dots, N$ . The definition of the  $C_m$  functions is given below (Subsection 4.2.2).

In order to find the time-advanced densities, we then have to find the roots of the set of equations:

$$Q_i = 0; \quad i = 1, \dots, N, \quad (4.7)$$

with the  $Q_i$  given by equations (4.5) and (4.6). If we take the  $\Delta t \rightarrow \infty$  limit in equation (4.5) this set of equations fully specifies the chemical equilibrium condition.

One of the common methods to find roots of the system (4.7) is the Newton-Raphson iteration. We apply this method to our particular problem as follows. One starts with an initial guess  $n_i$  ( $i = 1, \dots, N$ ) for the time-advanced densities. Then, expanding the  $Q_i(n_i)$  terms in a first order Taylor series one obtains:

$$Q_i + \sum_{m=1}^N \Delta n_m \frac{\partial Q_i}{\partial n_m} = 0. \quad (4.8)$$

Here, the partial derivatives are the elements of the Jacobian matrix. Both  $Q_i$  and  $\partial Q_i / \partial n_m$  are evaluated in the initial guess  $n_m$  ( $m = 1, \dots, N$ ) of the solution. We have then obtained a system of linear equations for the  $\Delta n_m$  corrections to our first guess for the time-advanced solution. This system is then solved using inversion methods for sets of linear equations (in our case, we use the standard routines of Press et al., 1993).

In this way, we find an improved guess

$$n_i^{(k+1)} = n_i^{(k)} + f \Delta n_i, \quad (4.9)$$

where  $n_i^{(0)}$  is our first guess for the time advanced densities, and  $f$  is a “convergence factor” that helps to reach convergence in the iteration process and is defined as:

$$f = \left( \frac{k}{N_{it}} \right)^\beta, \quad k \leq N_{it}; \quad f = 1, \quad k > N_{it}, \quad (4.10)$$

where  $N_{it}$  and  $\beta$  are chosen constants, and  $k$  is the current iteration number. We then recalculate the

rates and Jacobians with the corrected densities ( $n_i^{(1)}$ ), and repeat the process to obtain successively improved values for the time-advanced densities.

This iteration is repeated until a convergence criterion:

$$\frac{|n_i^{(k)} - n_i^{(k+1)}|}{n_i^{(k+1)}} < \epsilon, \quad (4.11)$$

is satisfied for all species  $i$ , where  $\epsilon$  is a previously chosen tolerance.

### 4.2.2 Conservation equations

The conservation equations (see equation 4.6) are determined by the total densities of the atomic elements present in all of the atomic/ionic/molecular species that are considered in the chemical network. For example, in a pure Hydrogen gas (of known total H density [H]) we have as possible species H<sub>2</sub> (molecular H), HI (neutral H), H II (ionized H) and electrons (as a result of the ionization of H). The associated conservation equations then are:  $C_H = [\text{H}] - 2[\text{H}_2] - [\text{HI}] - [\text{H II}] = 0$ , and  $C_e = [\text{H II}] - [e] = 0$  (here, the densities written as “[A]” correspond to the  $n_i$  of subsection 2.1).

In general, for an element  $A$  participating in the chemical network forming part of at least some of the (atomic/ionic/molecular) species  $n_k$ , the associated conservation equation is:

$$C_A = n_A - \sum_k a_k n_k = 0, \quad (4.12)$$

where  $n_A = [A]$  is the total density of element  $A$ , and  $a_k$  is the total number of  $A$  nuclei present in species  $k$  (with density  $n_k$ ). There is one conservation equation of this form for each element present in the chemical network, and the resulting set of conservation equations is used together with the rate equations to guarantee convergence to the correct chemical equilibrium (see equation 4.6).

### 4.2.3 Initial Newton-Raphson guess

For a system of equations such as (4.8) the convergence of the Newton-Raphson method strongly depends on the initial condition  $\mathbf{n}_0$ . We find that an appropriate initial guess for the time advanced densities (generally leading to a reasonably fast convergence) can be constructed as follows:

For a molecule  $[aA, bB]$  composed of “ $a$ ” atoms of element  $A$ , and “ $b$ ” atoms of element  $B$ , we

choose an initial density

$$n_i^{(0)} = \frac{1}{2} \min \left[ \frac{A_T}{a}, \frac{B_T}{b} \right] \quad (4.13)$$

where  $A_T$ ,  $B_T$  are the total densities of elements  $A$  and  $B$  (respectively). Equation (4.13) can be straightforwardly extended for molecules with three or more elements.

### 4.3 Description of KIMYA

Whether only the chemical kinetics is calculated, or if it is used within a hydrodynamic code, the operation of KIMYA is roughly as follows. As input, it needs the densities of all of the species and the temperature at a given time, and a timestep. With these values, the values of the  $Q$  functions and the Jacobian matrix are calculated (equation 4.8 of Section 4.2). The N-R method is used to obtain the new densities (4.9 in Section 4.2). The time-advanced densities are iterated until the relative differences between two successive iterations meet a (previously chosen) convergence criterion. This procedure is presented in the flowchart shown in Figure 4.1.

We have developed a benchmark suite using the network that will be described in section 4.5.3, with eleven chemical species and 40 chemical reactions. This particular benchmark serves to check the operation of the code when compared to laboratory experiments. We have run a benchmark test for  $10^4$ ,  $10^5$  and  $10^6$  timesteps. Our code solves a single timestep in  $\sim 3.9 \times 10^{-5}$  seconds of wall-clock time. This is relevant when one wants to couple this solver with a multi-dimensional gasdynamic code, where one should find the solution for each species in each of the  $10^4 - 10^9$  cells at every timestep.

### 4.4 The reactive flow equations

KIMYA is designed for inclusion in reactive flow numerical codes. Hydrodynamic codes in one, two or three dimensions solve the gas dynamic (or magnetohydrodynamic) equations in a discretized space. In the discrete “cells”, the mass, momentum and energy conservation equations are solved together with the chemical network (to which one adds advection terms for each species). Usually, in a complete simulation there are typically from  $10^5$  to  $10^9$  cells, and each one is advanced in time for thousands of time-steps, so that a fast integrator for the chemical network is clearly essential.

The gasdynamic equations are:

$$\frac{\partial \rho}{\partial t} + \nabla \cdot (\rho \mathbf{u}) = 0, \quad (4.14)$$



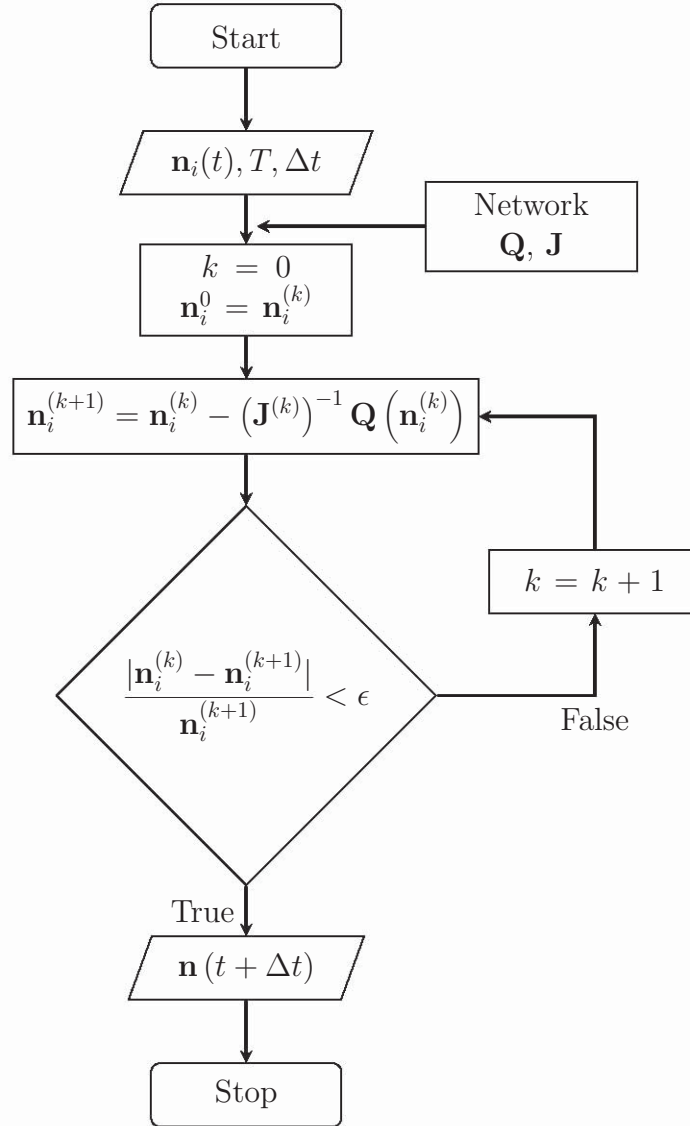


Figure 4.1: KIMYA flow chart. Our code receives the initial densities of each species, the gas temperature and an arbitrary time-step and returns the time-advanced densities.

$$\frac{\partial \rho \mathbf{u}}{\partial t} + \nabla \cdot \rho \mathbf{u} \mathbf{u} + \nabla P = 0, \quad (4.15)$$

$$\frac{\partial}{\partial t} \left( \frac{\rho \mathbf{u}^2}{2} + \frac{P}{\gamma - 1} \right) + \nabla \cdot \left[ \rho \mathbf{u} \left( \frac{\gamma}{\gamma - 1} \frac{P}{\rho} + \frac{u^2}{2} \right) \right] = G - L, \quad (4.16)$$

where  $\rho$ ,  $\mathbf{u}$  and  $P$  are the gas density, velocity and pressure, respectively.  $\gamma$  is the specific heat ratio.  $G$  and  $L$  are the thermal energy gain and loss (respectively) due to interaction with the radiative field or associated with the latent heat of the chemical reactions and/or the internal energy of the molecular/atomic/ionic species. The thermal pressure is given by

$$P = (n + n_e)kT, \quad (4.17)$$

where  $n$  is the total density (of molecules+atoms+ions) and  $n_e$  is the electron density.

The complete set of equations for a reactive flow can then be written for a 2D flow as:

$$\frac{\partial \mathbf{U}}{\partial t} + \frac{\partial \mathbf{F}}{\partial x} + \frac{\partial \mathbf{G}}{\partial y} = \mathbf{S}, \quad (4.18)$$

$$\mathbf{U} = [\rho, \rho u, \rho v, E, n_1, n_2, \dots, n_N] \quad (4.19)$$

$$\mathbf{F} = [\rho u, P + \rho u^2, \rho uv, u(E + P), n_1 u, n_2 u, \dots, n_N u] \quad (4.20)$$

$$\mathbf{G} = [\rho v, \rho uv, P + \rho v^2, v(E + P), n_1 v, n_2 v, \dots, n_N v] \quad (4.21)$$

$$\mathbf{S} = [0, 0, 0, 0, S_1, S_2, \dots, S_N] \quad (4.22)$$

where  $n_1, n_2, \dots, n_N$  are the densities of the different species. The vector  $\mathbf{U}$  contains the so-called conservative variables.  $\rho$ ,  $T$  y  $P$ , were defined previously,  $u$  and  $v$  are the velocity in the  $x$  and  $y$  direction (respectively), and  $E$  is the energy written as:

$$E = \frac{1}{2} \rho u^2 + \frac{P}{\gamma - 1}, \quad (4.23)$$

the thermal pressure  $P$  is given by equation 4.17.

We note that the evolution equations of the chemical network were included as  $N$  continuity equations (as active scalars) and the sources  $S_i$  are given by the right hand side of equation 4.2. These source terms should also include the appropriate geometrical terms when considering 2D, axisymmetric flow problems. Solutions to this set of equations are presented below.

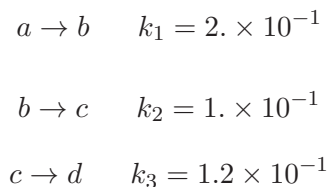
## 4.5 Numerical and experimental models to code verification

In order to show the characteristics of the KIMYA astrochemical code we provided three numerical simulations. We first try a standard test presented by Braun, Herron & Kahaner (1988), who used the ACUCHEM<sup>1</sup> code. The second test is a dark cloud model, which we describe in Section 4.5.2. Our third test deals with the nitric oxide formation with a laser induced plasma (meant to model a lightning discharge), which is described in Section 4.5.3. In all cases, the maximum number of iterations mentioned in subsection 4.2.1 is  $N_{it} = 40$ . In all cases the code reaches the convergence criterion for a smaller number of iterations.

### 4.5.1 Sequence reactions test

In this section, we show the implementation of the KIMYA code for two reaction systems proposed by Braun, Herron & Kahaner (1988): a sequence and a reverse reaction system.

The first test is the system of sequence reactions:



where,  $a, b, c$  and  $d$  are the species. The total density is,

$$n_T = n_a + n_b + n_c + n_d. \quad (4.24)$$

The creation and destruction rates of the species are given by,

$$\begin{aligned} \frac{dn_a}{dt} &= -k_1 n_a, \\ \frac{dn_b}{dt} &= k_1 n_a - k_2 n_b, \\ \frac{dn_c}{dt} &= k_2 n_b - k_3 n_c. \end{aligned} \quad (4.25)$$

The density of species  $d$  is calculated by means of the conservation equation (4.24).

---

<sup>1</sup><http://global.oup.com/us/companion.websites/9780199730728/Acuchem/>

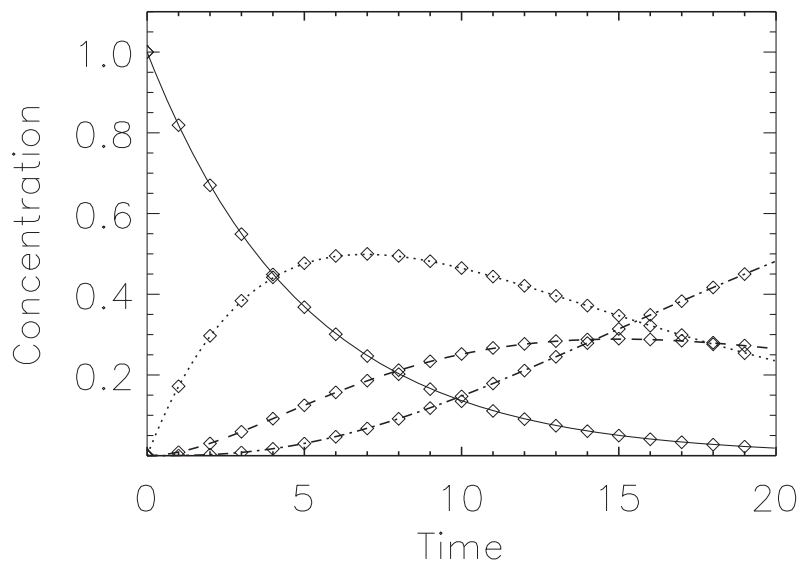


Figure 4.2: Normalized densities (concentrations) of species  $a, b, c$  and  $d$  as a function of time (in dimensionless units) obtained from the sequence test (see equations 4.24-4.25). The solid, dotted, dashed and dot-dashed lines, are the  $n_a, n_b, n_c$  and  $n_d$  concentrations obtained with KIMYA, respectively, and the diamonds are the corresponding values obtained using ACUCHEM.

We rewrite equations (4.24)-(4.25) in the form of equation (4.5):

$$\begin{aligned}
 Q_a &= -\frac{n_a - n_{a,0}}{\Delta t} - k_1 n_a, \\
 Q_b &= -\frac{n_b - n_{b,0}}{\Delta t} + k_1 n_a - k_2 n_b, \\
 Q_c &= -\frac{n_c - n_{c,0}}{\Delta t} + k_2 n_b - k_3 n_c, \\
 Q_d &= n_a + n_b + n_c + n_d - n_T,
 \end{aligned} \tag{4.26}$$

the root of this set of equations then gives the time-advanced solution.

With equations (4.26), we can calculate the Jacobian matrix,

$$\mathbf{J} = \begin{pmatrix} -1/\Delta t - k_1 & 0 & 0 & 0 \\ k_1 & -1/\Delta t - k_2 & 0 & 0 \\ 0 & k_2 & -1/\Delta t - k_3 & 0 \\ 1 & 1 & 1 & 1 \end{pmatrix} \tag{4.27}$$

Then, using the set of equations (4.26) and the Jacobian matrix (equation 4.27) in equation (4.8) we carry out a time integration from  $t = 0$  to  $t = 20$ . For the convergence factor (see equation 4.10) we set  $\beta = 0.0$  (i.e.,  $f = 1$ ), and we chose an  $\epsilon = 10^{-5}$  tolerance. We consider initial densities  $n_a = 1$  and  $n_b = n_c = n_d = 0$  (in dimensionless units).

Figure 4.2 shows the densities of the species  $a, b, c$  and  $d$  as functions of time (in dimensionless units), the solid, dotted, dashed and dot-dashed lines, are the  $n_a, n_b, n_c$  and  $n_d$  densities, respectively and the diamonds are the values calculated using the standard ACUCHEM code. The values obtained with our code are in very good agreement with the results obtained using ACUCHEM.

## 4.5.2 Dark cloud model

Dark clouds consist of cold ( $\sim 10$  K) and dense ( $10^3 - 10^6$ )  $\text{cm}^3$ , regions opaque to visible and UV radiation which are composed mainly of gas-phase molecular material. The dark clouds are very inhomogeneous, and usually present dense, filamentary structures. Also, the dust presented in these condensations completely absorbs the photons in optical and UV wavelengths.

Following the work of McElroy et al. (2013), we consider an isotropic and homogeneous medium with  $n(\text{H}_2) = 10^4 \text{ cm}^{-3}$ , and  $T = 10$  K. We want to compare our results with the chemical concentrations obtained by McElroy et al. (2013), who used the complete network of the UMIST database,

Table 4.1: Initial conditions in KIMYA.

| Species i      | $n_i/n_H$ <sup>1</sup> | Species i | $n_i/n_H$ |
|----------------|------------------------|-----------|-----------|
| H <sub>2</sub> | 0.5                    | H         | 5.0(-5)   |
| C              | 1.4(-4)                | O         | 3.2(-4)   |

<sup>1</sup> $n_H$  is the number density of H nuclei.

The  $a(b) = a \times 10^b$  format has been used

which includes direct cosmic-ray ionization reactions, cosmic-ray-induced photoreactions and interstellar photoreactions. This complete network is composed by 467 species and 6174 reactions. We have chosen a reduced subset of species and reactions (13 species and 146 reactions, see below) that correctly reproduces the chemical evolution, but with a significantly faster time-integration. We are most interested in reproducing the densities of OH, CO, H<sub>2</sub>O and H<sub>2</sub>, which are the most important molecules in the ISM which dominate the molecular cooling function (see Neufeld et al., 1993, 1995).

In order to compute our (simplified) dark cloud model, we use the following selection criteria for the reactions:

- the only ionized species are those that are formed solely of hydrogen;
- the atoms taking part in the network are only H, C, and O;
- the molecules contain at most three atoms;
- the only grain-surface reaction included is the formation of H<sub>2</sub> due to the combination of two atoms of H:

$$\frac{dn_{H_2}}{dt} = 5.2 \times 10^{-17} \left( \frac{T}{300} \right)^{0.5} n_H n_{HI} \quad [\text{cm}^{-3} \text{s}^{-1}], \quad (4.28)$$

where  $n_H$  and  $n_{HI}$  are the total number of H nuclei, associated to the dust grain density, and the density of neutral atomic hydrogen, related to the atoms available to form a new H<sub>2</sub> molecule, respectively.

Taking into account these considerations, we obtain a network with 13 species (H, H<sup>+</sup>, CH, CH<sub>2</sub>, H<sub>2</sub>O, OH, CO, C, C<sub>2</sub>, O, O<sub>2</sub>, HCO, CO<sub>2</sub>) together with 146 reactions (including the formation of H<sub>2</sub> in dust grain surfaces). We must note that, according to these criteria, direct cosmic-ray ionization reactions, cosmic-ray-induced photoreactions and interstellar photoreactions were excluded. The reaction coefficients are set to zero outside the temperature range in which they are valid.

We show the initial conditions for the dark cloud model in Table 4.1. The only molecule that has a non-zero concentration at the beginning of the simulation is H<sub>2</sub>.

We ran our simulation up to  $10^8$  yr. The results obtained are shown in columns 3 and 6 of Table 4.2. Columns 2 and 5 give the values taken from the webpage of the UMIST database with RATE 12 (McElroy et al., 2013) evolved up to the same time as our KIMYA simulation.

Table 4.2: Relative densities to  $H_2$  in a dark cloud model after  $10^8$  years

| Specie | Density<br>$\log(X/H_2)$ |        | Density<br>$\log(X/H_2)$ |        |        |
|--------|--------------------------|--------|--------------------------|--------|--------|
|        | Rate12                   | KIMYA  |                          | Rate12 | KIMYA  |
| H      | -3.60                    | -3.60  | C                        | -4.42  | -8.43  |
| $H^+$  | -4.91                    | -10.02 | $C_2$                    | -17.00 | -12.43 |
| CH     | -9.96                    | -10.47 | O                        | -3.55  | -3.54  |
| $CH_2$ | -3.95                    | -11.33 | $O_2$                    | -4.03  | -4.19  |
| $H_2O$ | -4.33                    | -6.35  | HCO                      | -17.00 | -11.25 |
| OH     | -7.93                    | -7.49  | $CO_2$                   | -7.08  | -6.94  |
| CO     | -3.88                    | -3.55  |                          |        |        |

The final concentrations of species like H, O, OH, CO, CH, and  $CO_2$  obtained in our calculations are in very good agreement with those reported in the UMIST homepage. This fact is important because these molecules are some of the most important for comparisons with astrochemical models and observations, since they are the most abundant in the ISM and play an important role in calculating the molecular cooling. Also, this first analysis will serve as a basis to explore and study in more details what kind of reactions are needed in order to improve the chemical evolution of different species.

### 4.5.3 Nitric oxide formed during lightning discharge

The production mechanism of nitrogen oxides by electrical discharges has been discussed by several authors, starting with the paper of Stark et al. (1996). The velocity of the shock fronts generated by laboratory scale discharges has been measured, and is found to be too slow to raise the air temperature up to  $\sim 3000$  K that is necessary for nitrogen fixation by the Zel'dovich mechanism (Zel'dovich & Raizer, 1966). The freeze out mixing ratio of  $NO_x$  in air has been measured directly for low pressure discharges and is found to be of the order expected from the Zel'dovich mechanism for the gas cooling over a timescale far longer than the duration of the shock front.

Navarro-González, McKay & Mvondo (2001a) presented an experimental study of the nitric oxide (NO) formation during a lightning discharge. A lightning was simulated in the laboratory by a plasma generated with a pulsed Nd-YAG laser. They presented the experimental variation of the nitric oxide yield as a function of the  $CO_2$  mixing ratio in simulated lightning in primitive atmospheres. The atmospheres are composed of  $CO_2$  and  $N_2$  at 1 bar, and all samples were irradiated at  $20^\circ C$  from 5 to 30 min.

Navarro-González et al. (2001b) reported an experimental assessment of the contributions of the shock wave and the hot plasma bubble to the production of nitric oxide by a simulated lightning. Their results provided a picture of the temperature evolution of a simulated lightning discharge from nanosecond to millisecond time scales and quantitatively assessed the contributions of the shock wave and the bubble to the nitrogen fixation rate on the gas target.

The experimental setup consists of a pulsing Nd:YAG laser which is focussed within an enclosure with gas of the chosen initial chemical composition. In the focal region, an approximately conically shaped plasma bubble is produced in each pulse. The plasma bubbles expand producing a central, hot gas region and outwards moving shocks. After a large number of laser pulses, the chemical composition of the enclosed gas is analyzed (see, e.g., Navarro-González, McKay & Mvondo, 2001a). We model this flow configuration by studying the time-evolution of hot, initially conical bubbles which expand into an initially homogeneous environment.

In order to study the formation of NO in these experiments, we applied KIMYA in two different ways: as a zero-dimensional model using the techniques presented in section 4.2 (using the experimentally determined time-evolution of the plasma/hot air and shock wave temperatures), and a gasdynamic model using the reactive flow equations described in section 4.4.

### Zero-dimensional model

We first compute “0D” numerical simulations (i.e., single parcel models) of NO formation using a gas with atmospheric pressure and an initial temperature of 300 K. We used a gas that was initially composed only of CO<sub>2</sub> and N<sub>2</sub>. We then performed a set of numerical simulations changing the initial chemical composition of the gas, that is, changing the proportion of CO<sub>2</sub> in the initial gas density ( $\chi_{\text{CO}_2}$ , by number). The simulations were carried out for the following values of  $\chi_{\text{CO}_2}$ : 0.25, 0.375, 0.5, 0.65, 0.8, 0.9, 0.975 and 0.99.

We used the time-dependent temperature shown in Figure 4.3 for the hot air bubble and the shock wave obtained experimentally by Navarro-González, McKay & Mvondo (2001a), then used KIMYA to calculate the nitric oxide yield using these two temperature profiles for 3000 consecutive pulses with a frequency of 1 Hz (one pulse per second).

The simulations have a chemical network of 11 species and 40 reactions. The reactions and the coefficients  $\alpha$  and  $\gamma$  in the Arrhenius equation ( $k = \alpha e^{\gamma/RT}$ , where  $T$  is the gas temperature), are



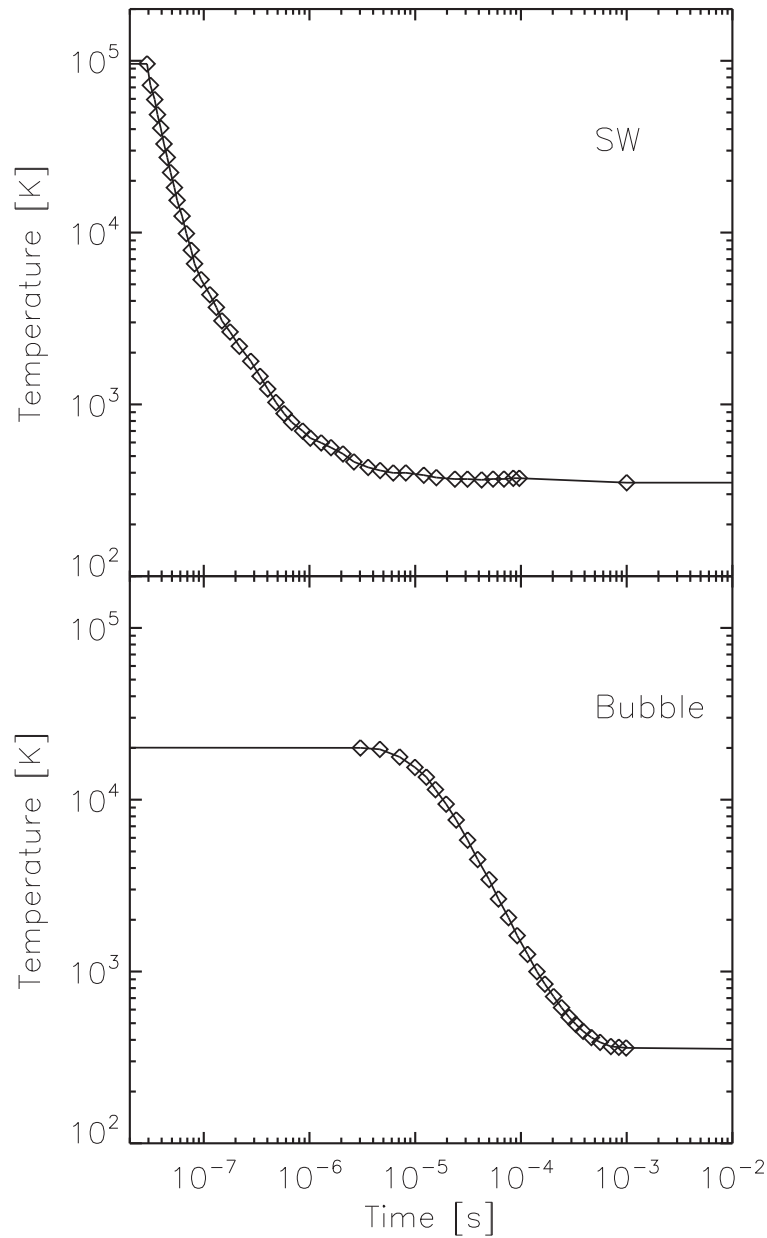


Figure 4.3: Temporal evolution of the post-shock wave temperature (top frame) and the bubble plasma/hot air temperature (bottom) obtained from a laser-induced plasma with a 300 mJ per pulse discharge energy (see also Navarro-González et al. 2001b). The diamonds are the experimental data, while the solid line represents the fitted curve used to run the numerical models.

shown in Table 4.3, columns 2, 3 and 4, respectively.

Figure 4.4 shows the number of molecules of nitric oxide formed by the laser pulse per unit energy (of the laser) versus the initial concentration of  $\text{CO}_2$ . The dash-dotted and dashed lines are the final concentrations (after the 3000 pulses, see above) obtained for the plasma/hot air bubble (dash-dotted line) and for the shock wave (dashed line), and the diamond symbols are the experimental measurements (with their errors) for all of the gas (bubble+shock wave) presented by Navarro-González, McKay & Mvondo (2001a).

It is clear that for  $\chi_{\text{CO}_2}$  between 0.25 and 0.95 the measured NO yields lie in between the simulated yields obtained for the hot bubble and for the shock wave. However, for  $\chi_{\text{CO}_2} \leq 0.2$  and for  $\chi_{\text{CO}_2} \geq 0.95$  there are significant differences between the model predictions and the experimental results. These differences are likely to be a result of the fact that our chemical network does not include some molecular species and/or reaction rates significant at very high or low initial values of  $\chi_{\text{CO}_2}$ .

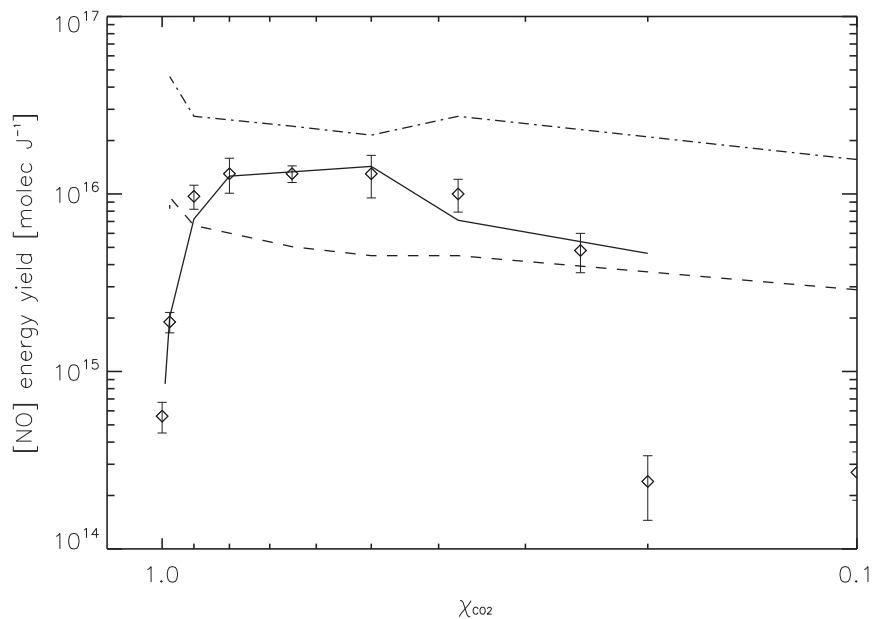


Figure 4.4: The variation of the nitric oxide yield as a function of the  $\text{CO}_2$  mixing ratio in simulated lightning for the experimental data (the diamonds) and the three numerical models. The dash-dotted (plasma/hot air bubble) and dashed lines (shock wave) correspond to the zero-dimensional model. The solid line corresponds to the hydrodynamical model (see the next section).

Figure 4.5 shows the evolution of the plasma temperature and number densities of  $\text{N}$ ,  $\text{N}_2$ ,  $\text{N}_2\text{O}$ ,

NO, NO<sub>2</sub>, NO<sub>3</sub>, O, O<sub>2</sub>, O<sub>3</sub>, CO and CO<sub>2</sub> for the first 18 simulated pulses. The peaks in the plasma temperature correspond to the energy injection times (i.e., to the laser pulses, which are assumed to produce instantaneous temperature rises). The concentrations of N<sub>2</sub>, NO, O and CO<sub>2</sub> go up and the concentrations of N, N<sub>2</sub>O, NO, NO<sub>2</sub>, NO<sub>3</sub> and O<sub>2</sub> decrease in the pulses. The NO yield has a peak in each pulse, but after  $\sim 1200$  pulses it attains an almost time-independent, constant value. This is the value that is compared with the experimental measurements.

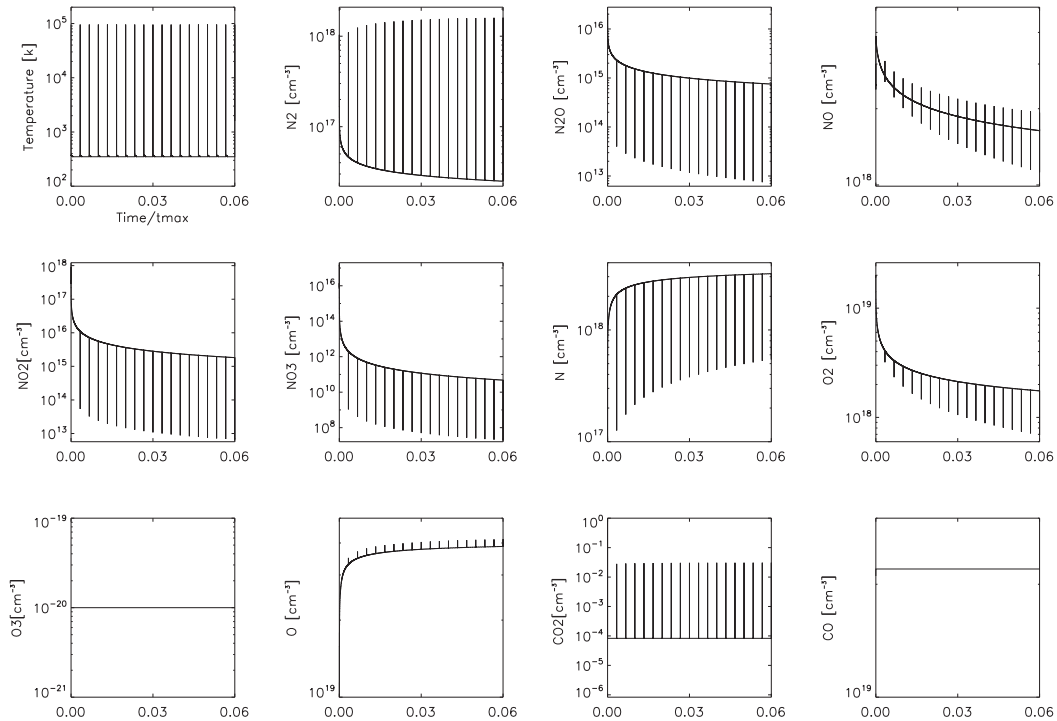


Figure 4.5: The evolution of the plasma temperature and numerical densities of N, N<sub>2</sub>, N<sub>2</sub>O, NO, NO<sub>2</sub>, NO<sub>3</sub>, O, O<sub>2</sub>, O<sub>3</sub>, CO and CO<sub>2</sub> for the first 18 simulated pulses. The time is normalized by  $t_{max} = 300.27$  s.

### Gasdynamic model

We also provided the reactive flow simulations using the WALIXCE 2D code (Esquivel et al. 2010) + KIMYA. The WALIXCE 2D code solves the gas dynamic equations (see equations 4.14-4.16 in Section 4.4) in a cylindrical, two-dimensional adaptive mesh, using a second-order HLLC Riemann solver (Toro et al. 1994). This fusion of the two codes is named WALKIMYA-2D. To carry out the numerical simulations, we integrate the gasdynamic equations and continuity/reaction rate equations for all of

the species, as discussed previously in Section 4.4.

The adaptative mesh consists of four root blocks of  $16 \times 16$  cells, with 7 levels of refinement, yielding a maximum resolution of  $4096 \times 1024$  (axial  $\times$  radial) cells. The maximum resolution (along the two axes) is of  $1.95 \times 10^{-3}$  cm. The boundary conditions used in the simulations are reflected on the symmetry axis and transmitted everywhere else. The size of the mesh is large enough so that the choice of outer boundaries does not affect simulations.

The timestep is chosen with the traditional CFL (Courant-Friedrichs-Lewy) stability condition of the explicit gasdynamic integrater of the WALIXCE 2D code (Esquivel et al. 2010). The same timestep is used for the (simultaneous) integration of the chemical reaction terms with the KIMYA routines.

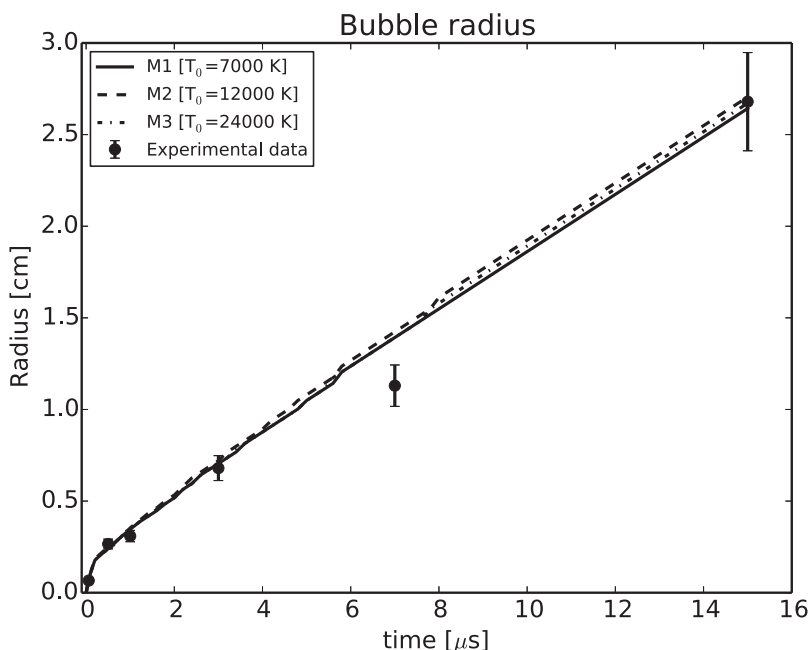


Figure 4.6: Radius of the simulated bubble versus time using different initial temperatures for the hot cone:  $T_0 = 7000$ ,  $12000$  and  $24000$  K (solid, dashed and dotted line, respectively). The symbols are the experimental data together with their respective errors.

An atmospheric pressure and temperature  $T = 300$ K were used as initial conditions. A  $\gamma = 7/5$ , constant specific heat ratio was assumed. The hot plasma bubble (generated in the experiment in the focal region of a focused laser pulse) is introduced in the center of the computational mesh, as a hot,  $T_0 \sim 10^4$  K cone of  $0.25$  cm (axial) length and  $\alpha = 30^\circ$  half-opening angle (the initial density within the cone having the environmental value, and the values chosen for  $T_0$  are discussed below).

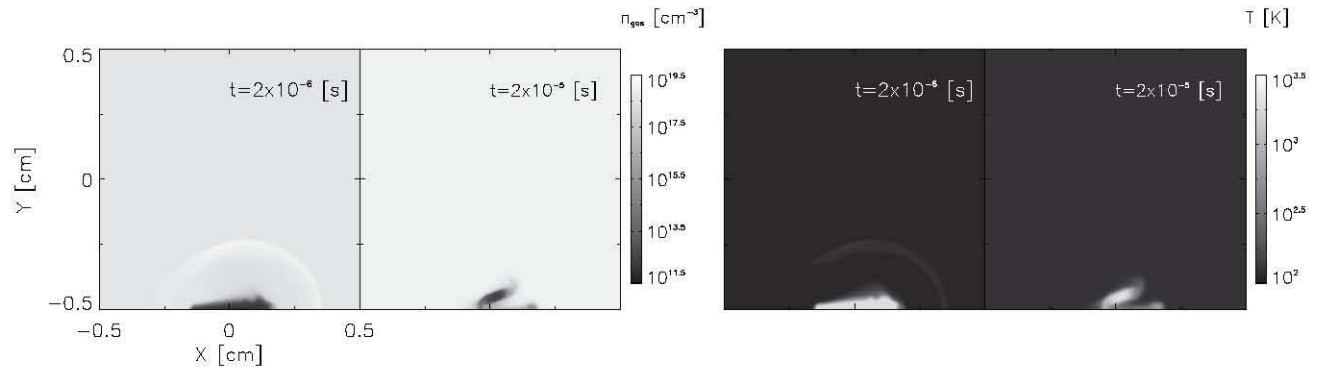


Figure 4.7: Density (left) and temperature maps (right panel) at  $t = 2 \times 10^{-6}$  and  $2 \times 10^{-5}$  s (as indicated on the top right of the frames of the two boxes). The left frames are the density maps and the frames on the right (of each panel) are the temperature maps.

This high pressure cone expands, driving a shock wave into the unperturbed environment. The simulations were stopped at  $2.0 \times 10^{-5}$  sec.

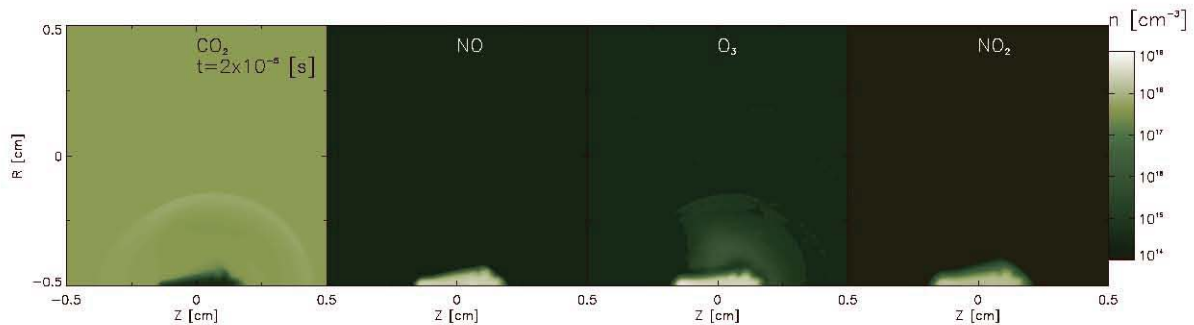


Figure 4.8: Density maps of  $\text{CO}_2$ ,  $\text{NO}$ ,  $\text{O}_3$  and  $\text{NO}_2$  at  $t = 2 \times 10^{-6}$ .

In order to reproduce the time-dependent evolution of the shock wave produced by an expanding, laser-generated plasma bubble, we computed simulations using initial temperatures (for the hot cone)  $T_0 = 7000$ ,  $12000$  and  $24000$  K. Figure 4.6 shows the average radius of the shock wave as a function of time, and we see that the three chosen values of  $T_0$  lead to the shock wave radii close to the experimentally measured values (see Raga et al. 2000, and references therein). The predictions for the chemical evolution that we present below are obtained from simulations with  $T_0 = 12000$  K.

Figure 4.7 shows density and temperature maps for two stages of the bubble evolution. The two panels on the left correspond to density maps for evolutionary times of  $2 \times 10^{-6}$  and  $2 \times 10^{-5}$  sec, and

the two panels on the right side are the temperature maps at the same two evolutionary times. At  $2 \times 10^{-6}$  sec, the gas which is compressed by the shock wave and a low density, inner region (with a temperature  $\sim 10^4$  K) are clearly seen. At  $10^{-5}$  sec, the shock wave is no longer visible, and the central, low density region has a  $\sim 1000$  K temperature.

The gas is initially composed only of  $\text{CO}_2$  and  $\text{N}_2$ . We compute simulations changing the initial value of  $\chi_{\text{CO}_2}$  in the same way as in the previous section to obtain densities of 11 chemical species as functions of time. Figure 4.8 shows the density maps of  $\text{CO}_2$ ,  $\text{NO}$ ,  $\text{O}_3$  and  $\text{NO}_2$  (left, center-left, center-right and right panels, respectively) at  $2 \times 10^{-6}$  sec obtained from the simulation with  $\chi_{\text{CO}_2} = 0.865$ . The  $\text{CO}_2$  is piled up behind the leading shock, while  $\text{NO}$ , ozone and  $\text{NO}_2$  have been formed in the inner, the hottest region of the central bubble. Notice that ozone is also weakly formed in an extended region between the hot bubble and the shock wave.

The total  $\text{NO}$  yields obtained from the simulations are shown with the solid line in Figure 4.4. It is clear that these yields are consistent with the experimental measurements of Navarro-González, McKay & Mvondo (2001a) over most of the explored  $\chi_{\text{CO}_2}$  range.

Finally, Figure 4.9 shows the total yield of all of the molecules included in the numerical simulations. We find that for initial  $\text{CO}_2$  densities larger than 0.865,  $\text{N}_2\text{O}$ ,  $\text{NO}_2$ ,  $\text{NO}_3$  and  $\text{O}_3$  do not form, but in environments with smaller initial  $\text{CO}_2$  and larger initial  $\text{N}_2$  densities, the formation of these oxides is very important.

#### 4.5.4 Scaling of the computational time

In order to illustrate the scaling of our reactive gasdynamic code as a function of number of species and reactions, we have carried out a set of simulations similar to the ones presented in section 4.5.3. In these simulations we change (see Table 4.4):

- the number of reactions (models M2a, M2b, M2c, M2d and M2e), but keeping the same number of species,
- the number of reactions and species (models M3, M4, M5 and M6).

In the left panel of Figure 4.10 (and also in column 4 of Table 4.4), we show the scaled computational time as a function of number of reactions. We have scaled the computational times using to the computational time of a purely hydrodynamic simulation (model M1, with no chemical species). From these models (models M2a, b, c, d and e) we see an approximately linear increase in com-

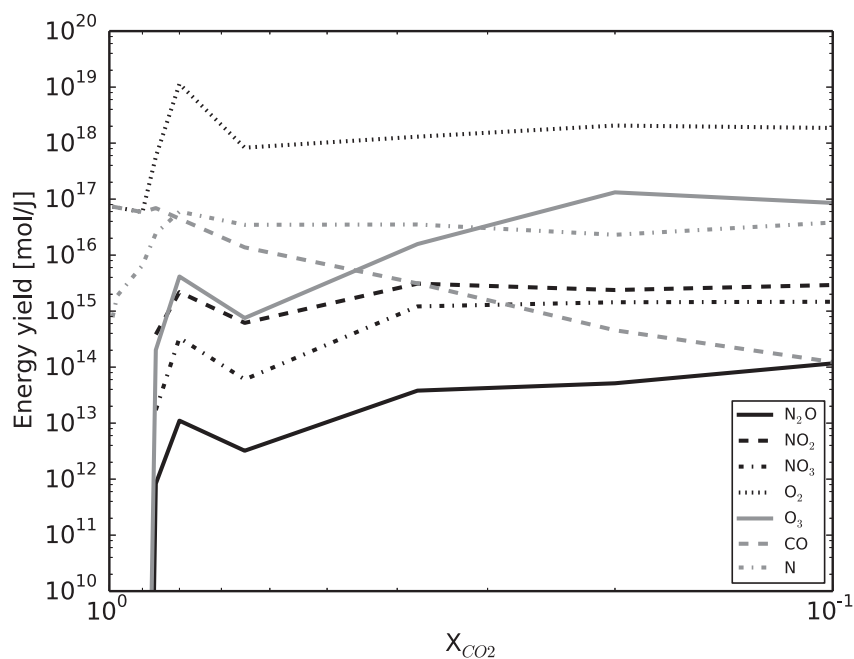


Figure 4.9: The variation of the  $\text{N}_2\text{O}$ ,  $\text{NO}_2$ ,  $\text{NO}_3$ ,  $\text{O}_2$ ,  $\text{O}_3$  and  $\text{N}$  yields as a function of the  $\text{CO}_2$  mixing ratio in the reactive flow numerical simulations.

putational time with number of chemical reactions (left panel of Figure 4.10). For the case of 140 reactions (model M2e), the computational time is  $\sim 1.8$  times larger than in the case of the purely gasdynamic simulation (model M1, see Table 4.4).

For the sequence of models with increasing number of species and reactions (models M3, M4, M5, M6 and M2e, see Table 4.4) we obtain a rapid growth of computational time for up to 15 species, and a slower growth from 15 to 31 species (see the right panel in Figure 4.10).

## 4.6 Discussion and Conclusion

We have presented the new KIMYA numerical code for solving chemical reaction networks. This code was written in Fortran 90 and has subroutines and modules providing the tools to solve the kinetical chemistry for a reaction network chosen by the user.

In order to solve the system of ODEs, we have implemented an implicit numerical solver (based on the standard, Newton-Raphson method). This method converges for arbitrary values of the chosen timestep.

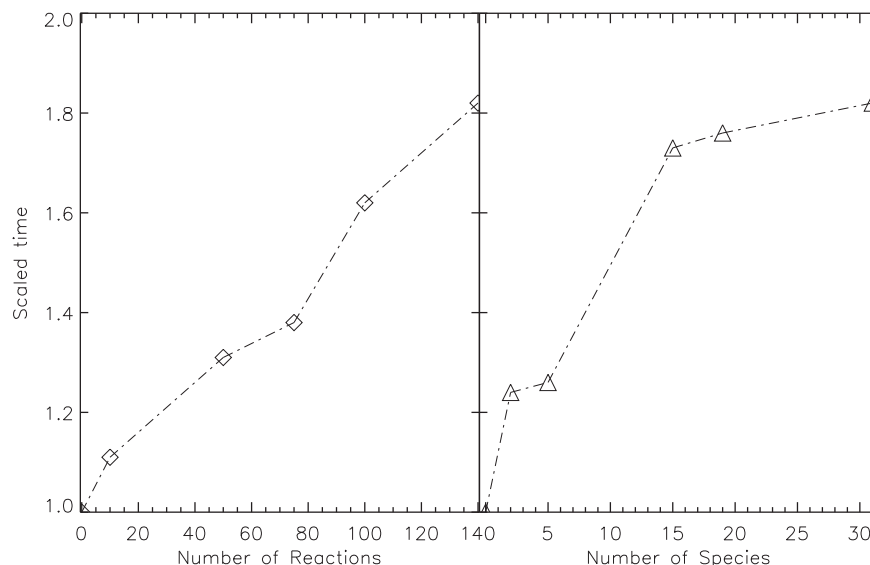


Figure 4.10: Left panel: computational time vs. number of reactions for the M2a, M2b, M2c, M2d, M2e sequence (with constant number of species, see Table 4.4). Right panel: scaled computational time vs. number of species for the sequence of models M3, M4, M5, M6 and M2e, with increasing numbers of species and reactions (see Table 4.4).

We have simulated two problems of interest:

- a dark cloud model: we have computed a single-parcel model which we compare with the previous work of McElroy et al. (2013). We find a good agreement, especially for species like O, OH, H<sub>2</sub>O, CO, and CO<sub>2</sub>. The chemical network used for our simulation consists of 13 species: H, H<sup>+</sup>, CH, CH<sub>2</sub>, H<sub>2</sub>O, OH, CO, C, C<sub>2</sub>, O, O<sub>2</sub>, HCO, CO<sub>2</sub>, and 146 reactions.
- laser laboratory experiments of the formation of nitric oxide during lightning discharges: we have computed single-parcel models and axisymmetric reactive gasdynamic models, and compared the induced chemistry with the experimental study of NO formation presented in Navarro-González, McKay & Mvondo (2001a). The models include changes in the initial chemical composition of the gas, and present the chemical composition after a single laser pulse and after 3000 pulses. We find that for initial CO<sub>2</sub> concentrations in the  $0.2 < \chi_{\text{CO}_2} < 0.95$  range, we obtain a remarkably good agreement between the numerical and experimental results.

Though this second problem is not of a direct astrophysical application, it allows us to evaluate the precision of reactive gasdynamic simulations, by comparing the final (spatially integrated) chemical composition obtained from the simulation with laboratory measurements.



We find that for a benchmark model which includes 11 chemical species and 40 chemical reactions, our code solves a single timestep in  $\sim 3.9 \times 10^{-5}$  s. We find that the speed of our algorithm is sufficient for combining it with a multi-dimensional gasdynamic (or magnetohydrodynamic) code, in which the chemical evolution must be solved in  $10^4 - 10^9$  computational cells.

Thus, KIMYA can be used to solve a chemical reaction network for a “single parcel” model. Also, the code can be integrated in a full gasdynamic (or magnetohydrodynamic) simulation, computing the temporal evolution of the chemical species. The most simple possible implicit timestep (see Section 4.2) carried out by KIMYA gives a short computational time which results in only relatively moderate ( $\sim$  factor of 2, see section 5.4) increases over “non-reactive” hydrodynamic simulations (without a chemical network). The KIMYA code is efficient and can handle a complex set of chemical reactions that can be used in interstellar chemistry, planetary atmospheres, combustion and detonation experiments, air pollution studies, among others.

Although the main utility of the code is to model different phenomena in the ISM, it can also be used in other areas (see above). We find that comparisons between the numerical simulations and experiments (see section 4.5) show good agreement. As far as we are aware, this is the first time that an astrophysical reactive gasdynamic code has been tested with laboratory experiments. This test gives confidence that our code is working properly. The experimental results we have described here could be used to test other reactive flow codes.

In order to make KIMYA more user friendly, we are planning to include an automatic chemical network generator. The code will then write the rate equations and the elements of the jacobian matrix directly from the reactions chosen by the user. Also, we will develop procedures for defining the set of reactions, choosing the more representative reactions for a particular problem and limiting the number of species. This is not an easy task, and a substantial effort must be made to find the best way to do this (Wiebe, Semenov & Henning (2003) and Grassi et al. (2012) for the case of astrochemical networks).

Table 4.3: Gas phase reactions used to model the NO formed during lightning discharge.

| No. | Reaction   | $\alpha$               | $\gamma$ [kJ] |
|-----|--|------------------------|---------------|
| 1   | $\text{N} + \text{N} + \text{M} \rightarrow \text{N}_2 + \text{M}$           | $2.6 \times 10^{-33}$  | -3.7          |
| 2   | $\text{N} + \text{O} + \text{M} \rightarrow \text{NO} + \text{M}$            | $2.6 \times 10^{-33}$  | -3.1          |
| 3   | $\text{N}_2 + \text{M} \rightarrow \text{N} + \text{N} + \text{M}$           | $8.5 \times 10^{-4}$   | 1102.2        |
| 4   | $\text{N}_2 + \text{e} \rightarrow \text{N} + \text{N} + \text{e}$           | $8.1 \times 10^{-13}$  | 0.            |
| 5   | $\text{NO} + \text{M} \rightarrow \text{N} + \text{O} + \text{M}$            | $3.1 \times 10^{-9}$   | 628.5         |
| 6   | $\text{NO} + \text{N} \rightarrow \text{N}_2 + \text{O}$                     | $3.2 \times 10^{-11}$  | 1.4           |
| 7   | $\text{NO} + \text{O} \rightarrow \text{N} + \text{O}_2$                     | $1.2 \times 10^{-11}$  | 169.7         |
| 8   | $\text{NO} + \text{O} + \text{M} \rightarrow \text{NO}_2 + \text{M}$         | $7.0 \times 10^{-33}$  | -5.7          |
| 9   | $\text{NO} + \text{NO} + \text{O}_2 \rightarrow \text{NO}_2 + \text{NO}_2$   | $3.3 \times 10^{-39}$  | -4.4          |
| 10  | $\text{NO} + \text{O}_2 + \text{M} \rightarrow \text{NO}_3 + \text{M}$       | $5.7 \times 10^{-41}$  | 1.8           |
| 11  | $\text{NO} + \text{NO} \rightarrow \text{N}_2 + \text{O}_2$                  | $2.5 \times 10^{-11}$  | 254.9         |
| 12  | $\text{NO} + \text{NO} \rightarrow \text{N}_2\text{O} + \text{O}$            | $4.5 \times 10^{-12}$  | 267.7         |
| 13  | $\text{NO} + \text{O}_3 \rightarrow \text{NO}_2 + \text{O}_2$                | $2.3 \times 10^{-12}$  | 11.7          |
| 14  | $\text{NO}_2 + \text{M} \rightarrow \text{NO} + \text{O} + \text{M}$         | $1.2 \times 10^{-12}$  | 117.3         |
| 15  | $\text{NO}_2 + \text{O} \rightarrow \text{NO} + \text{O}_2$                  | $5.8 \times 10^{-12}$  | 0.7           |
| 16  | $\text{NO}_2 + \text{O} + \text{M} \rightarrow \text{NO}_3 + \text{M}$       | $1.7 \times 10^{-33}$  | -8.7          |
| 17  | $\text{NO}_2 + \text{N} \rightarrow \text{N}_2\text{O} + \text{O}$           | $5.8 \times 10^{-12}$  | -1.8          |
| 18  | $\text{NO}_2 + \text{O}_3 \rightarrow \text{NO}_3 + \text{O}_2$              | $3.2 \times 10^{-13}$  | 22.1          |
| 19  | $\text{NO}_2 + \text{NO}_2 \rightarrow \text{NO} + \text{NO} + \text{O}_2$   | $2.7 \times 10^{-12}$  | 109.3         |
| 20  | $\text{NO}_2 + \text{NO}_2 \rightarrow \text{NO}_3 + \text{NO}$              | $5.7 \times 10^{-12}$  | 96.4          |
| 21  | $\text{NO}_3 + \text{M} \rightarrow \text{NO} + \text{O}_2 + \text{M}$       | $4.5 \times 10^{-13}$  | 17.6          |
| 22  | $\text{NO}_3 + \text{O} \rightarrow \text{NO}_2 + \text{O}_2$                | $1.0 \times 10^{-11}$  | 0.            |
| 23  | $\text{NO}_3 + \text{NO} \rightarrow \text{NO}_2 + \text{NO}_2$              | $4.8 \times 10^{-12}$  | -3.6          |
| 24  | $\text{NO}_3 + \text{NO}_2 \rightarrow \text{NO} + \text{NO}_2 + \text{O}_2$ | $1.5 \times 10^{-13}$  | 13.3          |
| 25  | $\text{N}_2\text{O} + \text{M} \rightarrow \text{N}_2 + \text{O} + \text{M}$ | $3.5 \times 10^{-10}$  | 220.6         |
| 26  | $\text{N}_2\text{O} + \text{O} \rightarrow \text{N}_2 + \text{O}_2$          | $2.6 \times 10^{-10}$  | 118.8         |
| 27  | $\text{N}_2\text{O} + \text{O} \rightarrow \text{NO} + \text{NO}$            | $1.4 \times 10^{-10}$  | 114.4         |
| 28  | $\text{N}_2\text{O} + \text{NO} \rightarrow \text{N}_2 + \text{NO}_2$        | $3.6 \times 10^{-10}$  | 211.5         |
| 29  | $\text{O} + \text{O} + \text{M} \rightarrow \text{O}_2 + \text{M}$           | $1.7 \times 10^{-34}$  | -6.0          |
| 30  | $\text{O} + \text{O}_2 + \text{M} \rightarrow \text{O}_3 + \text{M}$         | $9.2 \times 10^{-35}$  | -4.3          |
| 31  | $\text{O}_2 + \text{M} \rightarrow \text{O} + \text{O} + \text{M}$           | $5.0 \times 10^{-7}$   | 493.0         |
| 33  | $\text{O}_2 + \text{e} \rightarrow \text{O} + \text{O} + \text{e}$           | $4.3 \times 10^{-11}$  | 0.            |
| 34  | $\text{O}_2 + \text{N} \rightarrow \text{NO} + \text{O}$                     | $1.5 \times 10^{-10}$  | 63.1          |
| 34  | $\text{O}_3 + \text{M} \rightarrow \text{O}_2 + \text{O} + \text{M}$         | $1.2 \times 10^{-9}$   | 95.5          |
| 35  | $\text{O}_3 + \text{O} \rightarrow \text{O}_2 + \text{O}_2$                  | $1.2 \times 10^{-11}$  | 17.6          |
| 36  | $\text{O}_3 + \text{N} \rightarrow \text{NO} + \text{O}_2$                   | $5.7 \times 10^{-13}$  | 0.            |
| 37  | $\text{CO}_2 \rightarrow \text{CO} + \text{O}$                               | $1.3 \times 10^{-9}$   | -424          |
| 38  | $\text{CO} + \text{O} \rightarrow \text{CO}_2$                               | $1.7 \times 10^{-33}$  | -12.5         |
| 39  | $\text{CO}_2 + \text{N} \rightarrow \text{NO} + \text{CO}$                   | $3.2 \times 10^{-13}$  | -1710.        |
| 40  | $\text{O} + \text{CO}_2 \rightarrow \text{O}_2 + \text{CO}$                  | $2.46 \times 10^{-11}$ | -220.         |

Table 4.4: Numerical Models

| Model<br>Model | Number of<br>species | Number of<br>reactions | Scaled<br>time |
|----------------|----------------------|------------------------|----------------|
| M1             | 0 <sup>a</sup>       | 0                      | 1.0            |
| M2a            | 31                   | 10                     | 1.11           |
| M2b            | 31                   | 50                     | 1.31           |
| M2c            | 31                   | 75                     | 1.38           |
| M2d            | 31                   | 100                    | 1.62           |
| M2e            | 31                   | 140                    | 1.82           |
| M3             | 2                    | 1                      | 1.24           |
| M4             | 5                    | 6                      | 1.26           |
| M5             | 15                   | 47                     | 1.73           |
| M6             | 19                   | 82                     | 1.75           |
| M2e            | 31                   | 140                    | 1.82           |

<sup>a</sup> Solving only the hydrodynamic equations.



# Chapter 5

## Modelling the CO streamers in the Orion BN/KL region

To be send to *Monthly Notices of the Royal Astronomical Society* in July 2019. **P.R. Rivera-Ortiz**, A. Castellanos-Ramírez, A.C. Raga, R. Navarro-González, L. Hernández-Martínez, J. Cantó, F. Robles-Valdez, A. Esquivel & L. Zapata

*In this chapter we present numerical simulations of reactive flows for CO streamers observed in OMC1 Orion BN/KL. We have considered 15 chemical species, a cooling function for atomic and molecular gas, and the gas heating through the cosmic rays. Our numerical simulation explore different ejection velocities, interstellar medium densities, and the CO contents. Using the CO density and temperature, we have calculated the CO emissivity for every cell in our axisymmetric simulation, and we have built CO maps and PV diagrams that allow us to see the region in the streamer where the emission of CO is more important. We found that the peak of the CO emission is related with the ambient density and this peak is located at  $\epsilon = 0.6$  times the length of the streamer, at  $t < 300$  yr and this value increases in the older streamers, i.e. for ages larger than 500 yr, the peak of CO emission is at 75% of the finger length.*

### 5.1 Introduction

The BN/KL region, which has a great diversity of molecules, is located behind the Orion Nebula (at a distance of 414 pc from the Sun). This region has a breaking-up multiple stellar system (Rodríguez et al., 2017), a peculiar outflow with about 200 filamentary structures, known as “fingers”, detected in H<sub>2</sub> emission (Bally et al., 2015) and a system of “streamers” in CO emission (Zapata et al. (2009)). These three components seem to have been originated in the same ejection event approx-

imately 500 yr ago and could have been caused by a stellar merger or the dynamic rearrangement of a non-hierarchical system of young, massive stars or proto-stars. Strong evidences supporting this model were presented by Zapata et al. (2009), Bally et al. (2011) and Goddi et al. 2011, such as the velocities of the runaway stars that were presumably ejected from the same origin as the system of fingers and streamers.

The Orion BN/KL fingers were discovered by Allen & Burton (1993) as  $\text{H}_2$  2.1  $\mu\text{m}$  features emanating outwards from the central region of OMC-1 and terminating in a series of Herbig-Haro (HH) objects, which had previously been observed as [O I] 6300 Å, high-speed “bullets” by Axon & Taylor (1993). On the other hand, other observational studies present other properties that can help to constrain the physic of the fingers, i.e. kinematics of the  $\text{H}_2$  emission features has been studied with Fabry-Perot observations by Chrysostomou et al. (1997) and Salas et al. (1999) and the proper motion measurements was presented by Bally et al. (2011), as well as the proper motions of some of the optically detected bullets have also been presented by Doi et al. (2002).

Following Bally (2011 and 2015), there are about 200  $\text{H}_2$  fingers, which are longer to the NW and shorter to the SE and SW. Very few weak features to the E and NE. The longer fingers have a length of  $\sim 50000$  au (using the distance of 414 pc obtained in Menten 2007) and diameters between 800 to 3200 au. The shorter filaments are narrower, more numerous, and tend to overlap. The heads of the  $\text{H}_2$  fingers (seen in  $\text{H}_2$  and [Fe II] IR lines and optically as HH objects, see above) have diameters  $\sim 40 \rightarrow 400$  au. The well defined, longer filaments, have velocities of  $\sim 350 \text{ km s}^{-1}$  (derived from the radial velocity and proper motion measurements) .

The lengths and velocities of the fingers are consistent with an origin in a single ejection event (for all fingers) that occurs  $\sim 500 - 1000$  yr ago. However, there is evidence of a substantial braking of the motion of the heads of those fingers over their evolution (Bally et al. 2011). An estimation of the total kinetic energy of the fingers is about  $10^{46} \rightarrow 10^{47}$  erg, which can be interpreted as an estimation of the energy of an “ejection event” that gave rise to the present-day fingers.

This region also has an extended CO outflow which was first detected in single-dish observations by Kwan & Scoville (1976). In more recent using a interferometric observations, this outflow has been resolved into a system of CO “streamers” (Zapata et al. 2009, Bally et al. 2017). The CO streamers show a more isotropic direction distribution than the  $\text{H}_2$  fingers, with several streamers with infrared emission due of the  $J=2 \rightarrow 1$  rotational transition in CO molecule, into the NW. The total mass moving with velocities larger than  $20 \text{ km s}^{-1}$  is the  $\sim 8 M_{\odot}$  (Bally et al. 2015 and references therein). In order to propose a mean mass in each of the fingers, one can assumed that

all the fingers has the same mass, therefore dividing total mass in this region by the  $\sim 200$  observed fingers, and one can obtain the mass per finger  $\sim 0.04 M_{\odot}$ .

Many of the CO streamers partially coincide with the H<sub>2</sub> fingers but they do not reach out to the position of the optical bullets at the tip of the fingers. Typically, the CO emission of the streamers fades away at a fraction 0.3 – 0.7 of the length of the corresponding H<sub>2</sub> fingers. The CO streamers are barely resolved with the ALMA interferometer, with widths of 400 → 800 au (Bally et al. 2017). Therefore, the CO streamers are shorter and narrower than the H<sub>2</sub> fingers by factors of  $\sim 2$ . As some of the fingers and the streamers are spatially coincident and have different widths, it can be argued the CO emission is produced inside the H<sub>2</sub> fingers.

The radial velocities show a quite dramatic pattern of mostly red-shifted CO streamers to the W and SW, blue-shifted streamers to the N and E, and intermixed blue and red-shifted streamers to the NW. Also, the CO streamers have very dramatic “Hubble law”, linear radial velocity vs. distance signatures, which are also in a good agreement with a simultaneous ejection  $\sim 500$  yr ago (see Zapata et al. 2009). These “Hubble law” velocity vs. distance signatures indicate that the CO emitting material has not suffered substantial braking. The peak radial velocities (at the tip of the CO streamers) have values of less than  $\sim 120$  km s<sup>-1</sup>, corresponding to approximately 1/2 of the fastest spatial motions of the H<sub>2</sub> fingers (of  $\sim 350$  km s<sup>-1</sup>, see above).

The environment that surrounds the OMC1 outflow is a dense molecular core. Oh et al. (2016) analyzed the extinction and the overall angular spread of the H<sub>2</sub> emission and they proposed a lower density, in this molecular core, is  $\sim 10^5$  cm<sup>-3</sup>. From the CO emission, Bally et al. (2017) found an environment density between  $10^6$  and  $10^7$  cm<sup>-3</sup>, assuming a  $X_{CO} = 10^{-4}$  CO fraction, and a background temperature of 10 K. Lower values of  $X_{CO}$  would lead to higher estimates of the environmental density.

In this chapter we present preliminary results of our numerical models to explain the molecular structure in Orion BN/KL. This chapter presents the numerical simulations set up in Section 2 using WALKIMYA-2D code described in chapter 3 and in Castellanos-Ramirez (2018). In section 3, we present a CO emission analysis and finally, the contribution of these models to our understanding of the Orion BN/KL region are discussed in section 4.

## 5.2 Numerical simulation

We have computed 2D numerical simulations using WALKIMYA-2D code. The code solves the hydrodynamic equations and chemical networks, called reactive flows, on a axysymmetric numerical code, a completed description for the code is presented in Castellanos-Ramirez (2018) and Rivera-Ortiz et al. (2019). The chemical network tracks the abundances of 14 chemical species: non-equilibrium evolution of C, C<sub>2</sub>, CH, CH<sub>2</sub>, CO<sub>2</sub>, HCO, H<sub>2</sub>O, O, O<sub>2</sub>, H<sup>+</sup>, H<sup>-</sup>, H and via conservation laws H<sub>2</sub>, CO and OH are calculated. The selection of this network of species and their involved reactions is such that can explain the CO abundances in other astrophysical comparisons (Castellanos-Ramírez et al. 2018).

The complete set of equations for a reactive flow is explained in Castellanos-Ramirez (2018) and one can then write for a 2D flow as:

$$\frac{\partial \mathbf{U}}{\partial t} + \frac{\partial \mathbf{F}}{\partial x} + \frac{\partial \mathbf{G}}{\partial y} = \mathbf{S}, \quad (5.1)$$

where the vector  $\mathbf{U}$  contains the so-called conservative variables:  $\rho$ ,  $T$  and  $P$ ,  $u$  and  $v$  are the velocity in the  $x$  and  $y$  direction (respectively),  $\mathbf{F}$  and  $\mathbf{G}$  contain the fluxes in  $x$  and  $y$  directions, respectively and  $\mathbf{S}$  is the source vector. We also included the reaction rates for each of the chemical species and the thermal energy gain and loss due to interaction with the radiative field and latent heat of the chemical reactions and/or the internal energy of the molecular, atomic or ionic species. These source vectors also include the appropriate geometrical terms for an axisymmetric flow.

The energy equation includes the cooling function described by Raga & Reipurth (2004) for atomic gas and for lower temperatures,  $T < 5280$  K, we have included the parametric molecular presented in Kosiński & Hanasz (2007),

$$\Lambda_{\text{mol}}(T) = L_1 \cdot T^{\epsilon_1} + L_2 \cdot \exp\left(-\frac{c_*}{(T - T_*)^{\epsilon_2}}\right), \quad (5.2)$$

where  $L_1 = 4.4 \times 10^{-67}$ ,  $L_2 = 4.89 \times 10^{-25}$ ,  $c_* = 3.18$ ,  $\epsilon_1 = 10.73$ ,  $\epsilon_2 = 0.1$  and  $T_* = 1$ . K. The total radiative energy for temperatures lower than 5280 K is given by,  $L_{\text{rad},\text{mol}} = n_{\text{gas}} \cdot n_{\text{CO}} \cdot \Lambda_{\text{mol}}(T)$ , where,  $n_{\text{gas}}$  and  $n_{\text{CO}}$  are the number densities of the gas and the CO molecule, respectively. The cosmic ray ionization rate of atomic hydrogen is  $\Gamma_{\text{crp}} = 5 \times 10^{-28} n_{\text{H}}$ , see Henney et al. (2009). Finally, the thermal pressure is given by,  $P = (n + n_e)kT$ , where  $n$  is the total density (i.e. molecules+atoms+ions) and  $n_e$  is the electron density.

The dynamics of a single clump which moves in a homogeneous medium was simulated, with number density  $n_a$ . The adaptative mesh used 7 levels of refinement, yielding  $4096 \times 1024$  (axial  $\times$



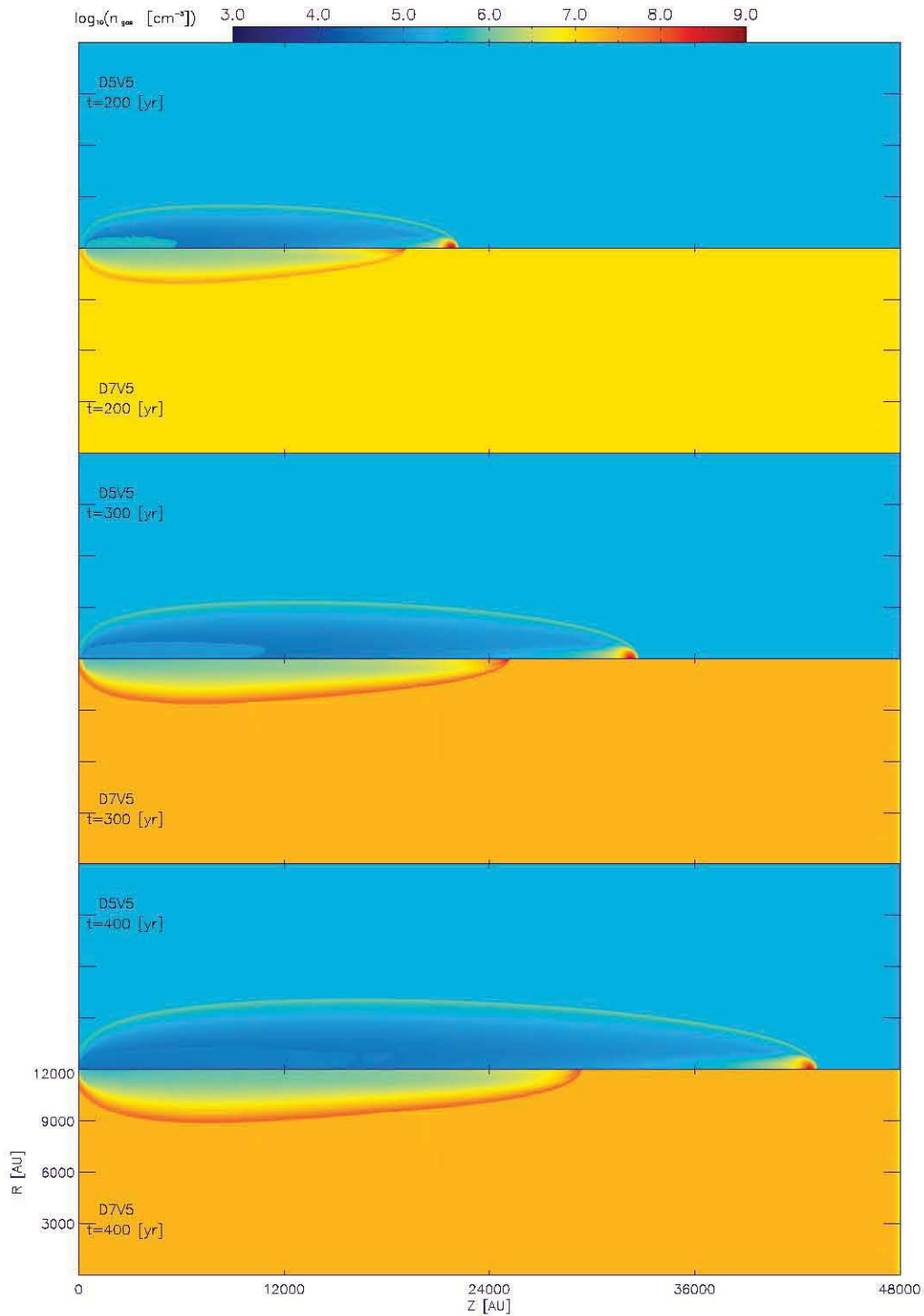


Figure 5.1: Snapshots from the numerical simulations showing the number density. Each pair of panel compares two models with initial velocity of  $500 \text{ km s}^{-1}$  and with interstellar medium density of  $10^5$  (up) and  $10^7$  (down)  $\text{cm}^{-3}$  at  $t = 200, 300$  and  $400$  years.

radial) cells, in a computational domain of  $48000 \times 12000$  au. Therefore, the maximum resolution of the simulations is 11 au per pixel. We used a reflective boundary condition for the symmetry axis and a free outflow boundary condition for all the other frontiers. The size of the mesh is large enough so that the outer boundaries do not affect the simulation. Similarly to Bally et al. (2015), we model fast, and homogeneous (in density and temperature) clumps to generate a CO streamer. The clumps were simulated as gas spheres which are ejected from 500 AU at the left side of the simulation box with:

- a velocity  $v_{cl} = 300 - 500 \text{ km s}^{-1}$ ,
- a radius  $r_{cl} = 50 \text{ au}$  (in the range of sizes observed for the heads of the H<sub>2</sub> fingers),
- a mass  $M_{cl} = 0.03 M_{\odot}$ , resulting in an initial number density of H<sub>2</sub> molecules of  $n_{cl} \sim 10^{10} \text{ cm}^{-3}$ ,
- a temperature  $T_{cl} = 30 \text{ K}$ .

These parameters are consistent with the H<sub>2</sub> and CO observations of the fingers/streamers system discussed in previous sections.

In all our simulations, we assumed a computational domain initially filled by an homogeneous, stationary ambient medium with temperature  $T_a = 100 \text{ K}$  and we ran models with different densities,  $n_a$ , as they are presented in Table 5.1. The ejection velocity,  $v_0$ , is a free parameter in our numerical simulations. We have selected a range of densities that coincide with those proposed by observations,

- H<sub>2</sub> number densities in the range  $n_a = 10^5 - 10^7 \text{ cm}^{-3}$ ,
- a  $T_a = 100 \text{ K}$  temperature.

We have ran 9 numerical simulations using different clump initial velocity and ambient density values. In Table 5.1 we present the numerical models physical conditions. For the both the clump and the environment, we assumed, initially, that H is fully in the form of H<sub>2</sub> and the CO density is  $n_{CO} = 1.6 \times 10^{-4} n_H$  (where  $n_H$  is the density of H nuclei), assuming that all O nuclei are in the form of CO.

Figure 5.1 shows the number density slices for the models D5V5 and D7V5 (upper and bottom panels, respectively) at evolutionary times 200, 300 and 500 yr (top, middle and bottom panels, respectively). As we can expect, clumps moving in denser environments have a larger deceleration and higher mass-loss than clumps moving in less dense ambients. After 500 years, the clump evolving in a interstellar medium of  $10^5 \text{ cm}^{-3}$ , the model D5V5, has traveled, at least, about 90 % of the

Table 5.1: Physical initial conditions of the numerical simulations

| Model | ISM                           | Clump                         |
|-------|-------------------------------|-------------------------------|
|       | $n_a$<br>[ $\text{cm}^{-3}$ ] | $v_{cl}$<br>[ $\text{km/s}$ ] |
| D5V3  | $10^5$                        | 300                           |
| D6V3  | $10^6$                        | 300                           |
| D7V3  | $10^7$                        | 300                           |
| D5V4  | $10^5$                        | 400                           |
| D6V4  | $10^6$                        | 400                           |
| D7V4  | $10^7$                        | 400                           |
| D5V5  | $10^5$                        | 500                           |
| D6V5  | $10^6$                        | 500                           |
| D7V5  | $10^7$                        | 500                           |

simulation box, and the head of the finger, the clump, keeps its form decreasing the gas density of the clump. Behind of the head, the gas expelled from the clump surface and dragged from the ambient forms a molecular tail. However, the clump evolving in a higher density ambient, with a number density of  $n_a = 10^7 \text{ cm}^{-3}$ , travels only during 200 yr without change its initial density structure. After this time the density is adjusted to the plasmon structure (see DA and Rivera-Ortiz et al. 2019). This increases the clump cross section, rapidly enlarging the clump deceleration.

Part of the gas expelled by the clump reaches temperatures between tens and hundreds of thousands Kelvins. With this temperature the molecules are dissociated and one would not expect CO emission from the clump expelled material. Additionally, the interaction between the bow shock and interstellar medium is another source of molecular dissociation. The supersonic motion of the clump produce a frontal shock wave, which modifies the interacting interstellar medium proprieties. The interstellar medium shocked temperature, density and velocity increase and can reach temperatures of some hundred thousands kelvins, for shocks with velocities of  $\sim 100 \text{ km s}^{-1}$ . However the velocity of the bow shock with respect to the interstellar medium has a maximum value on the front of the clump and the relative velocity between the shock and the interstellar medium has its lowest value in the transverse direction ( $R$ ) of the propagation of the stream. In this point, the bow shock velocity is approximately the local sound speed velocity  $\sim 10 \text{ km s}^{-1}$ , and the temperature of the shocked gas is only a few hundred of kelvins, where the molecules of the interstellar medium are not dissociated by the bow shock interaction.

### 5.3 The CO emission of the streamers

The intrinsic emissivity is obtained directly from the hydrodynamical simulations by integrating the CO emissivity a given line of sight. We obtained the CO emission coefficient in each of the numerical cells using the CO density and the temperature of the gas, in the emission coefficient equation,

$$j_{\text{CO}_{2 \rightarrow 1}} = \frac{1}{4\pi} \frac{g_1}{g_2} n_{\text{CO}} \cdot e^{-\frac{E_{\text{CO}_{2 \rightarrow 1}}}{kT_{ab}}} A_{\text{CO}_{2 \rightarrow 1}} E_{\text{CO}_{2 \rightarrow 1}}, \quad (5.3)$$

where,  $g_1 = 3$  is the gaunt factor and  $g_2 = \sum_i^N = e^{-T_{\text{levCO}}/T(i,j)}$ ,  $T_{\text{levCO}} = 0.0, 5.53, 16.60, 33.19, 55.32, 82.97, 116.16, 154.87, 199.11, 248.87, 304.16, 364.97, 431.29, 503.13, 580$  K,  $A_{\text{CO},J=2-1} = 7.16 \times 10^{-7} \text{ s}^{-1}$  is the spontaneous emission coefficient,  $E_{\text{CO},J=2-1} = h\nu_{\text{CO},J=2-1}$  is the energy of the transition,  $\nu_{\text{CO},J=2-1} = 230.538$  GHz and  $h$  is the Planck's constant.

To avoid the detailed radiative transfer calculation, we have to estimate the clump optical depth using its cross section  $\sigma_{\text{CO}}$  and number density  $n_{\text{CO}}$  as,

$$\tau = \Delta l n_{\text{CO}} \sigma_{\text{CO}}. \quad (5.4)$$

The optical length  $\Delta l$  is such that satisfies

$$\Delta l \left( \frac{dv_r}{dl} \right) = v_t, \quad (5.5)$$

where  $dv_r/dl$  is the derivative of the relative speed  $v_r$  along the line of sight  $l$  for an emitting source with thermal speed  $v_t$ .

For an homogeneous source of size  $R_c$ , constant relative speed and temperature, a zero-order approximation can be made,

$$\frac{dv_r}{dl} = \frac{v_r}{R_c}. \quad (5.6)$$

This leads to an optical length,

$$\Delta l = \frac{v_t}{v_r} R_c. \quad (5.7)$$

The optical depth  $\tau$  for the CO molecule can be computed. Assuming a constant temperature 10 K and a size  $R_c = 50$  au, which corresponds to a  $v_t = 0.13$  km s<sup>-1</sup>. This is significantly inferior to the ejection velocity of the clump of  $v_r \sim 300$  km s<sup>-1</sup>.

Also, we use a typical cross section  $\sigma_{\text{CO}} = 10^{-15}$  cm<sup>2</sup> and a CO number density related to the total  $n(\text{H}_2)$  as  $n_{\text{CO}} = 10^{-4} n(\text{H}_2)$ , with  $n(\text{H}_2) = 10^9$  cm<sup>-3</sup>. This gives an optical depth of  $\tau \sim 60$ . This

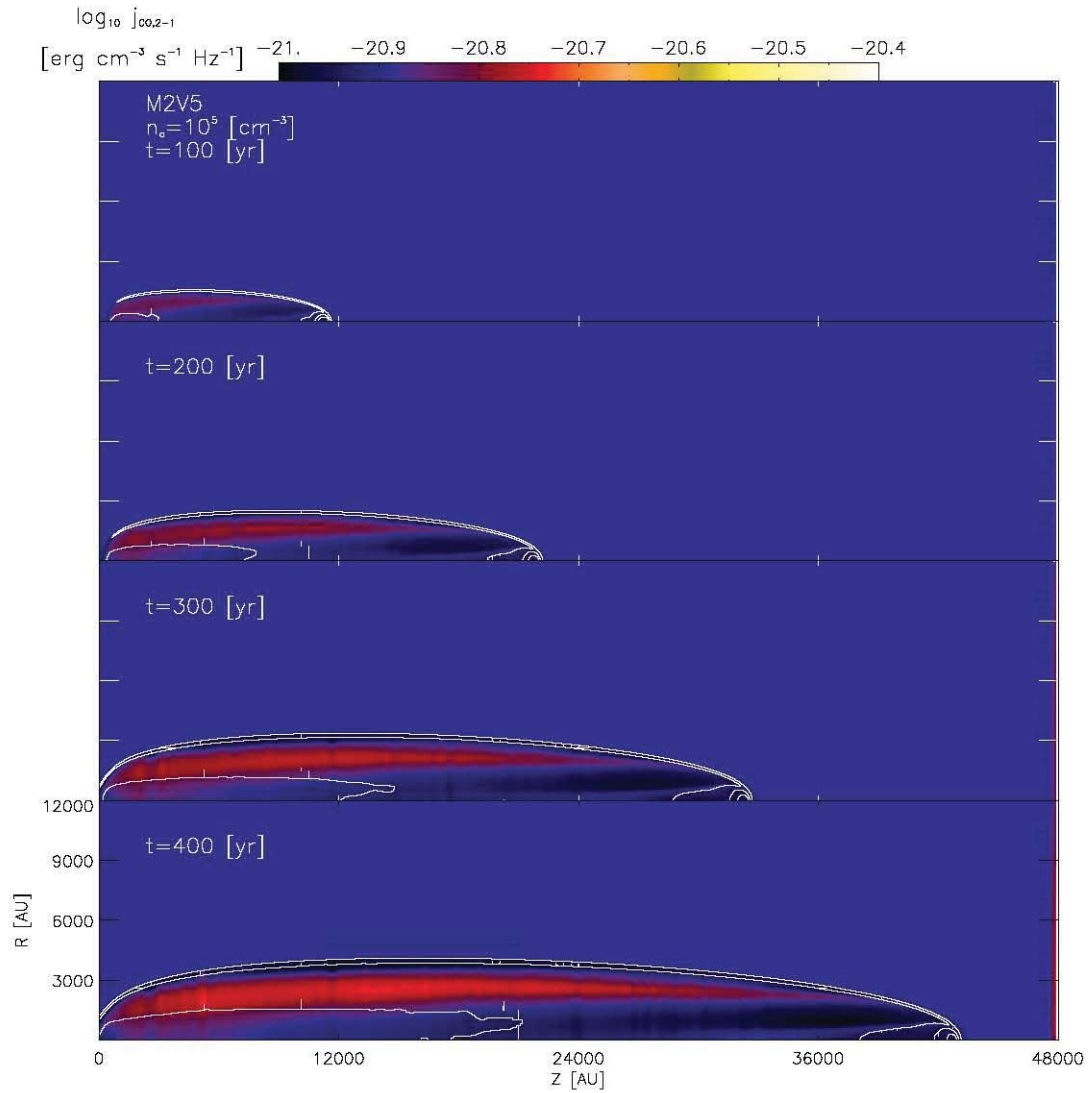


Figure 5.2: Snapshots from the numerical simulations showing the integrated CO emission and the gas number density. The panels are showing the evolutionary times 100, 200 300 and 400 yr top, top-middle, bottom-middle, bottom, respectively, for D5V5.

can be used to assume an optically thick CO emission, and avoid the detailed radiative transfer.

Figure 5.2 shows the integrated CO emission in a map of  $512 \times 128$  pixels in the horizontal and vertical axis, respectively. The CO emission, in  $\text{erg cm}^{-3} \text{s}^{-1} \text{Hz}^{-2}$ , is coded by the color scale as is shown in the color bar at the top of the map. The white contours follow the gas density. In this figure we have showed the emission maps at  $t=100, 200, 300$  and  $400$  yr, from the top to the bottom panel, respectively. As one can see, the CO emission is not coinciding with the leading clump but it is associated to its tail. However, it has its maximum in the middle of the streamer where some part of gas lost by the clump has interacted with the shocked interstellar gas. The gas, that crosses the bow shock, which moves at a few tens of kilometers per second velocity and moves almost transverse to the direction of movement of the clump, is not dissociated and also is not obscured due to the high density, as it happens in the clump head and the tail. Therefore, the larger CO emission is predicted at the middle of the stream.

We have also integrated the CO maps and obtained the total CO emission as a function only of the Z-coordinate, in our numerical simulations. Figure 5.3 shows the CO emission  $J=2 \rightarrow 1$  in Jansky as a function of the moving material length, for the evolutionary times 100, 200, 300, 400, 500, 600 and 700 yr for the model D6V3. In this figure, the size of the symbols sizes are related with the total emission (also the colors), the larger symbols are for the higher emission values. Note that the gas with velocities smaller than the local sound speed is not considered. One can see that the CO emission reaches the maximum value at about the middle of the finger total length, and the velocity of the streamer is a linear function of its length up to 0.6 times the finger length such as a *Hubble type law*. The slope of this linear relationship is lower as the evolutionary time increases. On the other hand, in the region with CO emission, the velocities are slower than the initial velocity of the clump,  $300 \text{ km s}^{-1}$ , and in the 600 yr track, the fastest parcel of gas with CO emission has a velocity of around  $200 \text{ km s}^{-1}$ .

On the other hand, we can see the maximum value of the CO emission for the model D6V3 at  $t=500$  yr located about  $0.075 \text{ pc}$  and the maximum length of the CO streamer is  $\sim 0.125 \text{ pc}$ , so the ratio between the maximum and total length of the CO streamer, that we called  $\epsilon$ , is 0.6. We have calculated  $\epsilon$  for the models D5V3, D6V3, D7V3, D5V4, D6V4, D7V4, D5V5, D6V5 and D7V5. At evolutionary time,  $t$ , of 500 yr the model D6V4 and D6V5 have a  $\epsilon$  value of 0.75 and 0.77, respectively being  $0.16$  and  $0.20 \text{ pc}$ , the length of the CO streamers. That is, the ejected clumps with higher ejected velocities, as one can expect, have longer CO streamers, in addition to having larger  $\epsilon$  values.

To compare our numerical simulations with the observations directly we have created a synthetic

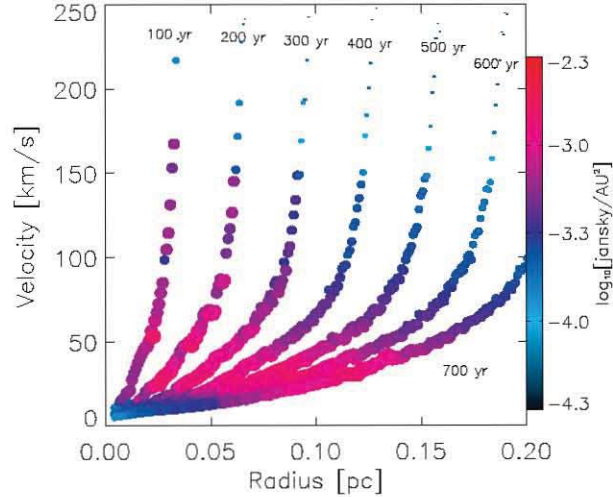


Figure 5.3: The integrated CO emission versus velocity of the gas. The colors represent the CO,  $J=2-1$  emission in Jansky. The evolutionary time at 100, 200, 300, 400, 500, 600 and 700 yr for the model D6V3 is presented. The size of the symbols decrease for lower emissions and it is zero if the gas velocity is lower than the local sound speed.

Position-Velocity diagram, rotating the axi-symmetric simulation around the symmetry axis to create a 3D mesh. Then, we assumed a projection angle with respect to the plane of the sky and integrating along the line of vision, obtained a position-velocity diagram for the model D7V5 at  $t=600$  yr presented in Figure 5.4. It presents the emission in a color scale as a function of the material at a distance  $P$  from the simulation origin, and relative velocity  $V$  to the observer.

This synthetic PV diagram has three characteristic features: the emission of the leading clump, a strong extended across the position axis emission, and a linear streamer emission disconnected of the clump. This is very similar to the observed PV-diagram (Figure 5.5 in Bally et al., 2017), which presents the overlapping emission near the position axis, and the linear Hubble type law along streamers. There are no reported observations of emitting clumps. This can be explained if clumps have a small CO fraction. Using models with a CO fraction  $10^{-3}$  the canonical value of the CO fraction  $10^{-4}$ , we can reduce the clump emission in the PV-diagrams. This suggests that the diagram presented by Bally et al. (2017) could present very weak emitting clumps that are not reported.

Figure 5.6 shows the ratio between the position of the CO emission maximum and the total length of the CO streamer,  $\epsilon$ , as a function of time. The solid, dashed and dotted lines in this figure are the models with the ambient density  $10^4$ ,  $10^5$  and  $10^6$   $\text{cm}^{-3}$ , respectively. The upper, middle and bottom panels present the models with ejection velocities 300, 400 and 500  $\text{km s}^{-1}$ . This figure shows that

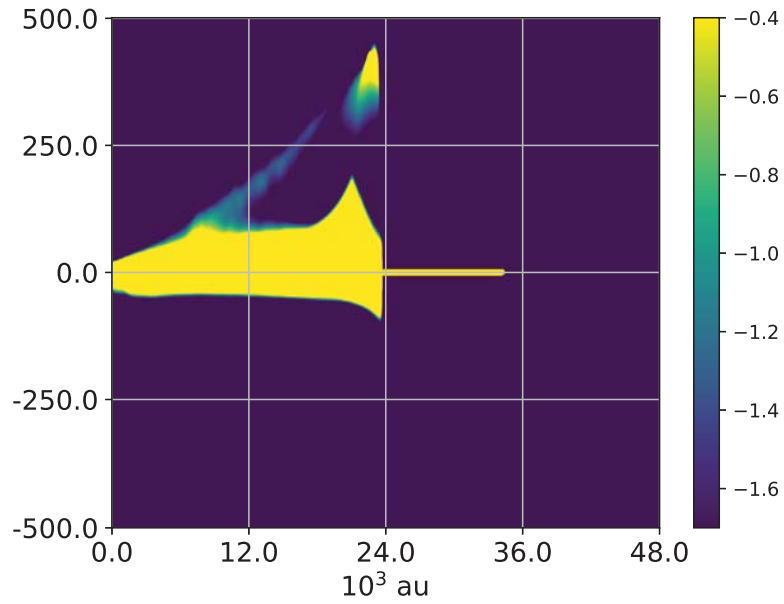


Figure 5.4: Synthetic position-velocity diagram for the model MV at 600 years. The vertical and horizontal axes are in  $\text{km s}^{-1}$  and  $10^3 \text{ au}$ . The color bar is in  $\log(\text{erg cm}^{-2} \text{ s}^{-1} \text{ sr}^{-1})$

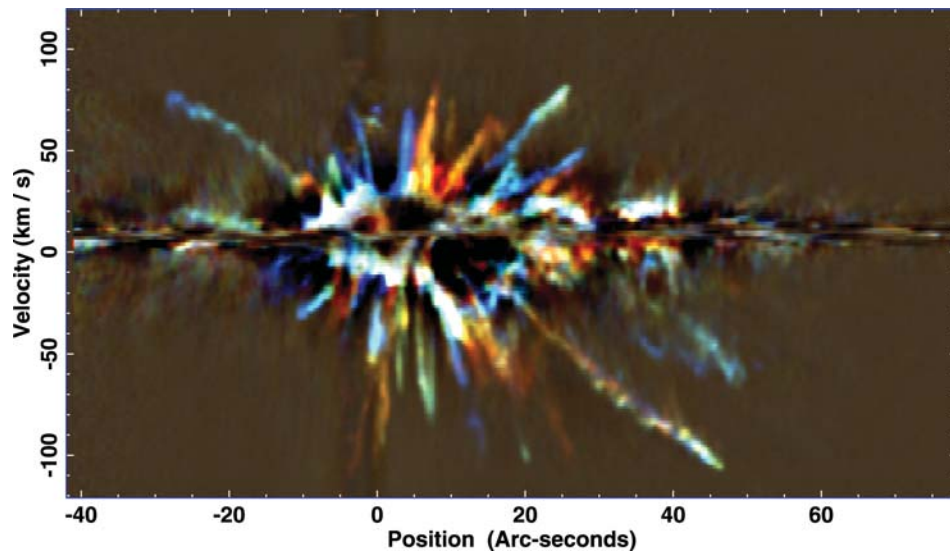


Figure 5.5: Observed position-velocity diagram (Bally et al., 2017)



in models with the ambient gas density  $10^4 \text{ cm}^{-3}$  the  $\epsilon$  ratio changes with the evolutionary time. At early evolutionary times,  $\epsilon \sim 0.5$ , that implies that the CO emission maximum value is located around the middle of the  $\text{H}_2$  finger. The value of  $\epsilon$  grows with the age of the streamers. However, in the models with the ambient gas densities  $10^5$  and  $10^6 \text{ cm}^{-3}$   $\epsilon$  has a value around  $\sim 0.8$ .

## 5.4 Discussion

In this chapter, we have presented our preliminary results of the numerical models of the CO streamers in the Orion BN/KL region. We have carried out numerical simulations of reactive flows, using the Walkimya code to model the CO emission observed in the Orion BN/KL streamers. Our numerical simulations considered 14 chemical species, a cooling function for atomic and molecular gas, and the heating through the cosmic rays. We have used different ejection velocities, densities of the interstellar medium and the amount of CO in the interstellar medium.

Using the CO densities and temperatures obtained in the simulations, we have calculated the CO emissivity for every cell and built CO maps which allow us to see the region in the streamer where the CO emission is produced. Using our numerical simulations we have found that the CO emission is coming from the interstellar medium gas shocked by the bow shock in the back of clump where bow shock sweeps the medium with a few tens of  $\text{km s}^{-1}$ . The CO streamers emission is smaller than the fingers, as is observed in the Bally et al. (2017), as well as the maximum peak of the CO emission is near to the total length of the CO streamers. The length of the CO emission, as one can expected, increase as a function of time, however in the front part of the CO streamer, the emission falls down rapidly.

An important CO emission is coming from the interstellar medium crossing the bow shock where the crossing velocity is not large enough to strongly increase the gas temperature. The shock wave velocity in the transverse direction is not larger than  $10 \text{ km s}^{-1}$  and the temperature of the swept up gas is less than 1000 K. Therefore, the molecular species are not dissociated. Finally, we have calculated the PV diagrams and found a characteristic *Hubble type law* for the CO streamers as a function of the distance from the origin center.

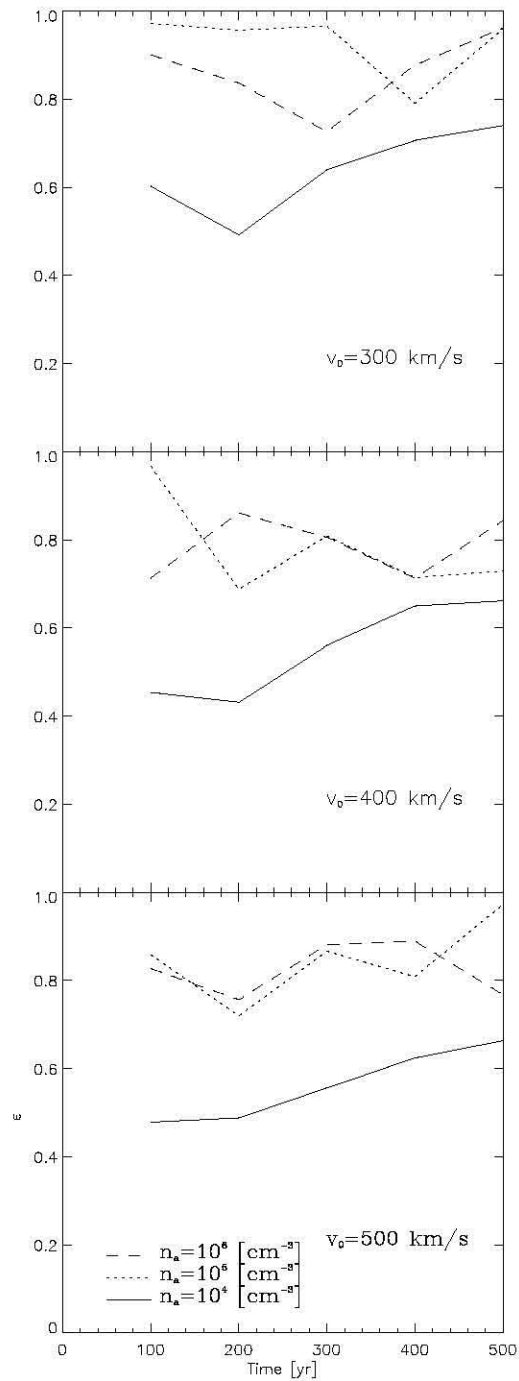


Figure 5.6: The ratio between the position of the maximum in the emission of CO and total length of the CO finger. The solid, dashed and dotted lines are the models with interstellar medium density of  $10^4$ ,  $10^5$  and  $10^6$   $\text{cm}^{-3}$ , respectively, and the upper panel present the epsilon values for the models with ejection velocity of  $300$   $\text{km s}^{-1}$ , the middle panel shows the model with ejection velocity of  $400$   $\text{km s}^{-1}$  and the models with ejection velocities of  $500$   $\text{km s}^{-1}$  are presented in the bottom panel.

# Chapter 6

## Conclusions

Along this work we have studied the region Orion BN/KL and the close encounter event that is associated to its formation. We assume an encounter 544 years ago between sources I, BN and n, related to the ejection mechanism of the clumps that generated the filamentary structure of the region. We summarize our results revisiting the particular goals presented in Chapter 1:

- **Analyze the dynamics of a dense and high velocity clump**

The dynamics of a dense clump ejected was explored in Chapter 2. Through numerical simulations, we have reproduced the motion of a spherical clump thrown into the interstellar medium. The plasmon derived by De Young & Axford (1967) was used as a first attempt to explain the motion of the clumps. Nevertheless, the model did not reproduce our numerical simulations after  $\sim 100$  years, mostly by the evaporation and fragmentation of the gas. We have performed the plasmon model derived by De Young & Axford (1967), adding a mass loss rate per unit area that is proportional to the density and the sound speed of the ejected clump. This leads to interpret mass as a function of the plasmon velocity related by a constant,  $\alpha$ .  $\alpha$  is a friction coefficient, and it depends on the density contrast, between the plasmon and the surrounding environment. Several numerical simulations were performed in the comparison between the results of these and the analytic models help us to validate our analytic model. We found several differences between the constant mass plasmon and the losing mass model: The lifetime obtained from the simple plasmon model is greater than that expected by our losing mass considerations. The deceleration obtained by this method is more likely to be responsible for the age discrepancy in astronomical flows as the Orion fingers. Also, a plasmon with greater ejection speed has a shorter lifetime, which can be observed on simulations, as well. The final length of a plasmon is not related to its shape and depends on the initial conditions of the

plasmon.

- **Explain the deceleration of the H<sub>2</sub> fingers, in order to justify the assumption of an origin in a single ejection event**

In Chapter 3, we applied the observational data of the Orion fingers obtained by several authors to a loosing mass plasmon model, more consistent with the observable constraints of the Orion Fingers. We used the model to obtain the ejection conditions of the single ejection event, constraining the parameters of the explosion in: the size, the ejection velocity and the initial mass of each clump. Even so, it is necessary to complete the observational data, since we have used only the projected information for the region, and spectroscopic information is required to obtain the real length and velocity of the fingers. However, this model can explain the deceleration of the outflow, making plausible to explain that the clumps were expelled in a single event, with masses, energy and velocities in the range of expected values. And, using our model, we found that the lifetimes of the clumps observed in Orion are close to the age of the injection event, which implies that some fingers could have ended their lives with a finite mass. This would explain the H<sub>2</sub> emission with no proper motion and that some CO streamers are not related to H<sub>2</sub> fingers. But the model does not explain the CO emission nor the fact that the CO streamers follow a Hubble type law that has no deceleration.

- **Implement a chemical network solver in hydrodynamical simulations**

In Chapter 4, we have presented the new KIMYA numerical code, which can be used to solve chemical reaction networks. This code was written in Fortran 90 and has subroutines and modules providing the tools to solve the kinetical chemistry for a reaction network chosen by the user. In order to solve the system of ODEs, we have implemented an implicit numerical solver, based on the standard, Newton-Raphson method. This method in principle converges for arbitrary values of the chosen timestep. In order to test the code we have simulated two problems of interest:

- a dark cloud model
- laser laboratory experiments of the formation of nitric oxide during lightning discharges

Though this second problem is not of direct astrophysical application, it allows us to evaluate the precision of a reactive gasdynamic simulation, by comparing the final (spatially integrated) chemical composition obtained from the simulation with laboratory measurements. We find that for a benchmark suite solving 11 chemical species and 40 chemical reactions, our code

solves a single timestep in  $\sim 3.9 \times 10^{-5}$  s. We find that the speed of our algorithm is sufficient for combining it with a multi-dimensional gasdynamic (or magnetohydrodynamic) code, in which the chemical evolution must be solved in  $10^4 - 10^9$  computational cells.

Although the main utility of the code is to model different phenomena in the ISM, it can also be used in other areas. We find that comparisons between the numerical simulations and experiments are in good agreement. As far as we are aware, this is the first time that an astrophysical reactive gasdynamic code has been tested with laboratory experiments.

The KIMYA code is efficient and can handle a complex set of chemical reactions that can be used in interstellar chemistry, planetary atmospheres, combustion and detonation experiments, air pollution studies, among others.

- **Reproduce the observed characteristics of the CO streamers using numerical simulations**

In Chapter 5, we assumed that the CO streamers are formed by the same clumps that form the H<sub>2</sub> fingers. To probe this, we use our numerical code to estimate the CO abundance conditions that can explain observations. We have carried out numerical simulations of reactive flows, using the code WALKIMYA-2D to model the CO streams observed in OMC1 Orion BN/KL. Our numerical simulations considered 14 chemical species, a cooling function for atomic and molecular gas, and the heating through the cosmic rays. We have used different ejection velocities, density of the interstellar medium and the amount of CO in the middle. Using the CO density and temperature, we have calculated the CO emission for every cell in our axisymmetric simulation, and we have built CO maps that allow us to see the region in the stream where the emission of CO is more important. In our numerical simulation, we have considered a different molecular content in the medium as the clump, because the clump has a density higher than the environment, the number of CO molecules in the clump and in the material that this loses, is higher compared to the CO of the environment, attenuating the emission and it is not possible to observe the emission of CO from the gas this region of the stream.

Using the CO emission maps and PV diagrams, we can conclude that the CO emission is coming, mainly, by the interstellar medium that crosses the shock wave and moves perpendicular to the direction of the motion of the clump. The shock wave velocity there is not larger than  $10 \text{ km s}^{-1}$  and the temperature of the swept up gas is less than 1000 K, therefore the molecular species are not dissociated. Using our numerical simulations we have found that the CO emission is coming from the interstellar medium gas shocked by the bow shock in the back of the

clump where the velocity with which the bow shock sweeps the medium is a few tens of  $\text{km s}^{-1}$ .

We found that the peak of the CO emission is related with the ambient density the relation between the radius and velocity from the source (radius zero) is from 0.6 times of the length of the stream, at  $t < 300$  yr and this value increase in the older streams, with ages larger than 500 yr, when  $\epsilon = 0.75$ .

Also we have reproduced PV diagrams from the simulations and found the characteristic *Hubble law* of the CO streamers as a consequence of the excitation of the material swept up by the decelerating clumps that generate the  $\text{H}_2$  fingers.

Currently, the effect of the dust is being explored. The inclusion of the dust in the dynamics of a plasmon can restrain even more the ejection conditions. Qualitatively, the same density contrast between a clump and the environment would lead to a smaller size if we consider the same initial mass. Also, the chemistry would be affected by the gas-dust reactions and the sublimation of chemical species produced by the shocks. One of the future objectives is to quantify the total effect of the dust in the region and its influence in the dynamics, chemistry, deviation, fragmentation and instabilities of the molecular material. Also, in the future, we plan to explore the motion of a clump in a variable density environment and the effect on the dynamic history.

Then, the losing mass plasmon model can be used in another explosive events, such as DR21 and G5.89, to find the ejection conditions and the energy involved in the explosion. The analysis of more regions like those, can give a more precise idea of the duration and contribution of the event in the enrichment of the interstellar medium.

Finally, even when we have proposed a dynamic model and a chemical network solver that can be used in several astrophysical contexts, the precise mechanism that led to the decay of the stellar cluster and the formation of the filamentary outflow remains unknown. Then, a model that can explain the ejection of clumps as the result of the close interaction of star forming objects is still necessary.

# Bibliography

- Allen, D. A., & Burton, M. G. 1993, *Nature*, 363, 54
- Bally, J., Licht, D., Smith, N. & Walawender, J., 2005, *AJ*, 129, 355.
- Bally, J., Cunningham, N. J., Moeckel, N., Burton, M. G., Smith, N., Frank, A. & Nordlund, A., 2011, *ApJ*, 727, 113.
- Bally, J., 2016, *ARA&A*, 491, 54
- Bally, J., Ginsburg, A., Silvia, D. & Youngblood, A., 2015, *A&A*, 579, 130.
- Bally, J., Ginsburg, A., Arce, H., Eisner, J., Youngblood, A., Zapata, L. & Zinnecker, H., 2017, *ApJ*, 837, 60.
- Bañó Esplugues, G. 2014, PhD thesis, Universidad Complutense de Madrid, Madrid, España
- Barger, A. J., Aragon-Salamanca, A., Ellis, R. S., et al. 1996, *MNRAS*, 279, 1
- Bates, D. R., & Spitzer, L. J. 1951, *ApJ*, 113, 441
- Baulch DL, Bowman CT, Cobos CJ, Cox RA, Just T, Kerr JA, Pilling MJ, Stocker D, Troe J, Tsang W, Walker RW, Warnatz J (2005) Evaluated kinetic data for combustion modeling: supplement II. *J Phys Chem Ref Data* 34:757-1397.
- Becklin, E. E., & Neugebauer, G. 1967, *ApJ*, 147, 799
- Beuther, H., & Nissen, H. D. 2008, *ApJ*, 679, L121
- Braun, W., Herron, J. T. & Kahaner, D. K., 1988, *Int. J. Chem. Kinet.*, 20, 51.
- Brouillet, N., Despois, D., Lu, X.-H., et al., 2015, *A&A*, 576, A129
- Canto, J., Espresate, J., Raga, A. C. & D'Alessio, P., 1998, *MNRAS*, 296, 1041.
- Cantó, J., Raga, A. 1991, *ApJ*, 372, 646.

- Castellanos-Ramírez, A., Rodríguez-González, A., Rivera-Ortíz, P. R., Raga, A. C., Navarro-González, R. & Esquivel, A., 2018, *RMxAA*, 54, 409.
- A. Castellanos-Ramírez, A. Rodríguez-González, P. R. Rivera-Ortiz, A. C. Raga, R. Navarro-González & A. Esquivel, 2018, *RMxAA*, 54, 409
- Crowley JN, Ammann M, Cox RA, Hynes RG, Jenkin ME, Mellouki A, Rossi MJ, Troe J, Wallington TJ (2010) Evaluated kinetic and photochemical data for atmospheric chemistry. *Atmos Chem Phys* 10:9059-9223.
- Cunningham, N., 2006, "Extended shocks within one kiloparsec: Instrumentation and observations", *PhD*, 80p.
- Curtiss, C.F., & J.O. Hirschfelder. 1952. *Proc. Nat. Acad. Sci.* 38:235-243.
- Dahlquist, G.G. & B. Lindberg. 1973. Technical Report TRITA-NA-7302. Stockholm: Royal Institute of Technology.
- Daly, R. A. , 1994, *ApJ*, 38, 426
- Daly, R. A. , 1995, *ApJ*, 580, 454
- De Young D. S., Axford W. I., 1967, *Nat*, 216, 129.
- Doi, Takao, O'Dell, C. R. & Hartigan, Patrick, 2002, *AJ*, 124, 445.
- Kosiński, R. & Hanasz, M., 2007, *MNRAS*, 376, 861.
- Doeleman, S. S., Lonsdale, C. J., Phillips, R. B., Barvainis, R. E., & Greenhill, L. J. 1998, in *Bulletin of the American Astronomical Society*, Vol. 30, American Astronomical Society Meeting Abstracts, 1362
- Draine, B. T., & Hao, L., 2002, *ApJ*, 569, 780
- Esquivel A., Raga A. C., Cantó J., Rodríguez González, A., López-Cámara D., Velázquez P. F., De Colle F., 2010, *ApJ*, 725, 1466
- Feng, S., Beuther, H., Henning, Th., Semenov, D., Palau, A. & Mills, E. A. C., 2015, *A&A*, 581, 71.
- Friedel, D. N., & Widicus Weaver, S. L., 2012, *ApJS*, 201, 17
- Fuente, A., Cernicharo, J., Caselli, P., et al. 2014, *A&A*, 568, A65
- Furuya, R. S., & Shinnaga, H. 2009, *ApJ*, 703, 1198



- Garrod, R. T., Widicus Weaver, S. L., & Herbst, E. 2008, *ApJ*, 682, 283
- Gear, C. W. Numerical initial value problems in ordinary differential equations, Englewood Cliffs, N.J.: Prentice Hall.
- Genzel, R., Reid, M. J., Moran, J. M., & Downes, D. 1981, *ApJ*, 244, 884
- Greenhill, L. J., Gwinn, C. R., Schwartz, C., Moran, J. M., & Diamond, P. J. 1998, *Nat*, 396, 650
- Goddi, C. 2010, *From Stars to Galaxies: Connecting our Understanding of Star and Galaxy Formation*, 36
- Goddi, C., Humphreys, E. M. L., Greenhill, L. J., Chandler, C. J. & Matthews, L. D., 2011, *ApJ*, 728, 15.
- Goicoechea, J. R., Chavarría, L., Cernicharo, J., et al., 2015, *ApJ*, 799, 102
- Graham, M. F., Meaburn, J., & Redman, M. P. 2003, *MNRAS*, 343, 419
- Grassi T., Bovino S., Gianturco F. A., Baiocchi P., Merlin E., 2012, *MNRAS*, 425, 1332
- Grassi, T., Bovino, S., Schleicher, D. R. G., et al. 2014, *MNRAS*, 439, 2386
- Henney, W. J. and Arthur, S. J. and de Colle, F. and Mellema, G., 2009, *MNRAS*, 157, 398
- Henney, W. J., Arthur, S. J., de Colle, F. & Mellema, G., 2009, *MNRAS*, 398, 157.
- Hosokawa, T. & Omukai, K., 2009, *ApJ*, 691, 823.
- Hosokawa, T., Yorke, H. W. & Omukai, K., 2010, *ApJ*, 721, 478.
- Jacobson, M., Z. Fundamentals of Atmospheric Modeling, 2nd ed. Cambridge University Press 2005, Chapter 10.
- Kahn, F.D., 1980, *Astron&Astrophys*, 83, 303 Kaifu, N., Usuda, T., Hayashi, S. S., et al. 2000, *PASJ*, 52, 1
- Kleinmann, D. E., & Low, F. J. 1967, *ApJl*, 149, L1
- Kosiński, R. and Hanasz, M., 2007, *MNRAS*, 376, 376
- Kwan, J., & Scoville, N. 1976, *ApJl*, 210, L39

- Loinard, L., Zapata, L. A., Rodriguez, L. F., et al. 2011, *Bulletin of the American Astronomical Society*, 43, 434.44
- Lu, J. 2013, HST Proposal,
- Maret, S., Caux, E., Baluteau, J. P., et al. 2001, *The Promise of the Herschel Space Observatory*, 460, 455
- May, R., & J. Noye. 1984. *Computational techniques for differential equations*, ed. J. Noye, 1-94. New York: North-Holland.
- McElroy D., Walsh C., Markwick A. J., Cordiner M. A., Smith K., & Millar T. J., 2013, *A&A*, 550, A36
- Millar TJ, Rawlings JMC, Bennett A, Brown PD, Charnley SB (1991). *Astron Astrophys Suppl Ser* 87:585-619
- Motoyama K., Morata O., Shang H., Krasnopolsky R., Hasegawa T., 2015, *ApJ*, 808, 46
- Navarro-González, R., McKay, C. P. & Nna Mvondo, D., 2001a, *Nature*, 412, 5.
- Navarro-González, R., Villagrán-Muniz, M., Sobral, H., Molina, L. T. & Molina, M. J., 2001b, *GEOPHYS. RES. LETT.*, 28, 3867.
- Navarro-González, R., E. Vargas, J. de la Rosa, A. C. Raga, and C. P. McKay (2010), *Reanalysis of the Viking results suggests perchlorate and organics at midlatitudes on Mars*, *J. Geophys. Res.*, 115, E12010
- Nejad, L. A. M. 2005, *Ap&SS*, 299, 1
- Neufeld, D. A., & Kaufman, M. J. 1993, *ApJ*, 418, 263
- Neufeld D. A., Lepp S., & Melnick G. J., 1995, *ApJS*, 100, 132
- Niederhofer, F., Humphreys, E. M. L., & Goddi, C., 2012, *A&A*, 548, A69
- Nissen, H. D., Cunningham, N. J., Gustafsson, M., et al., 2012, *A&A*, 540, A119
- Oh, H., Pyo, T., Kaplan, K., Yuk, I., Park, B., Mace, G., Park, C., Chun, M., Pak, S., Kim, K., Sok Oh, J., Jeong, U., Yu, Y., Lee, J., Kim, H., Hwang, N., Lee, H., Nguyen Le, H., Lee, S. & Jaffe, D., 2016, *ApJ*, 833, 275.
- Palau, A., Zapata, L. A., Román-Zúñiga, C. G., et al., 2018, *ApJ*, 855, 24

- Peng, T.-C., Zapata, L. A., Wyrowski, F., Güsten, R., & Menten, K. M. 2012, *A&A*, 544, L19
- Plambeck, R. L., Wright, M. C. H., Friedel, D. N., et al. 2009, *ApJl*, 704, L25
- Press, W. H., Teukolsky, S. A., Vetterling, W. T., & Flannery, B. P. 2007, *Numerical Recipes 3rd Edition: The Art of Scientific Computing*, 3rd edn. (New York, NY, USA: Cambridge University Press)
- Puy, D., Grenacher, L., & Jetzer, P. 1999, *A&A*, 345, 723
- Plambeck, R. L., Wright, M. C. H., Welch, W. J., et al., 1982, *ApJ*, 259, 617
- William H. Press, Saul A. Teukolsky, William T. Vetterling, and Brian P. Flannery. 1993. *Numerical Recipes in Fortran; the Art of Scientific Computing* (2nd ed.). Cambridge University Press, New York, NY, USA.
- Raga, A. C. & Biro, S., 1993, *MNRAS*, 264, 758.
- Raga, A., Cabrit, S., Cantó, J. 1995, *MNRAS*, 273, 422.
- Raga, A. C., Canto, J., Curiel, S. & Taylor, S., *MNRAS*, 295, 738.
- Raga A. C., Navarro-González R., Villagrán-Muñiz M., 2000, *RMxAA*, 36, 67
- Raga, A. C. & Reipurth, B., 2004, *RMxAA*, 40, 15.
- Raga, A. C., Sobral, H., Villagrán-Muniz, M., Navarro-González, R., & Masciadri, E. 2001, *MNRAS*, 324, 206
- Raga, A. C. and Reipurth, B., 2004, *RMxAA*, 15, 40
- Raas, W. L., Doleman, S. S., & Lonsdale, C. J. 2000, *Bulletin of the American Astronomical Society*, 32, 43.01
- Reid, M. J., Menten, K. M., Greenhill, L. J., & Chandler, C. J. 2007, *ApJ*, 664, 950
- Reipurth, B., & Bally, J. 2001, *ARA&A*, 39, 403
- Rimmer, P. B. 2012, PhD thesis, The Ohio State University
- Rivera-Ortiz, P., Rodríguez-González, A., Hernández-Martínez, L. & Cantó, J., 2019, *ApJ*, 874, 38.
- Rodríguez, L. F., Dzib, Sergio A.; Loinard, L., Zapata, L., Gómez, L., Menten, K. & Lizano, S., 2017, *ApJ*, 834, 140.

- Salas, L., Rosado, M., Cruz-González, I., et al. 1999, *ApJ*, 511, 822
- Schiffer, III, F. H. 1976, PhD thesis, Wisconsin Univ., Madison.
- Schwartz, C., Greenhill, L. J., Diamond, P. J., Moran, J. M., & Gwinn, C. R. 1997, *Bulletin of the American Astronomical Society*, 29, 07.19
- Schultz, A., Colgan, S. W. J., Bally, J., et al. 2007, *Bulletin of the American Astronomical Society*, 39, 62.06
- Semenov, D., Hersant, F., Wakelam, V., et al. 2010, *A&A*, 522, A42
- Smith, B. D., Bryan, G. L., Glover, S. C. O., et al. 2017, *MNRAS*, 466, 2217
- Snell, R. L., Scoville, N. Z., Sanders, D. B., & Erickson, N. R. 1984, *ApJ*, 284, 176
- Stark, M. S., Harrison, J. T. H. & Anastasi, C., 1996, *Journal of Geophysical Research: Atmospheres*, 101, 6963.
- Taylor, D. and Dyson, J. E. and Axon, D. J., 1992, *MNRAS*, 351, 255
- Taylor, K. N. R., Storey, J. W. V., Sandell, G., Williams, P. M., & Zealey, W. J. 1984, *NAT*, 311, 236
- Toro, E. F., Spruce, M., & Speares, W. 1994, *Shock Waves*, 4, 25
- Ubachukwu, A. A. and Okoye, S. E. and Onuora, L. I., 1991, *ApJ*, 56, 383
- Veilleux, S. and Tully, R. B. and Bland-Hawthorn, J., 1993, *AJ*, 1318, 105
- Velázquez, P. F., Sobral, H., Raga, A. C., Villagrán-Muniz, M., & Navarro-González, R. 2001, *RMxAA*, 37, 87
- de Vicente, P., Martín-Pintado, J., Neri, R., & Rodríguez-Franco, A., 2002, *ApJl*, 574, L163
- Wakelam V et al (2012). *Astrophys J Suppl Ser* 199:21. doi:10.1088/0067-0049/199/1/21
- Wiebe D., Semenov D., Henning Th., 2003, *A&A*, 399, 197
- Wiseman, J. J., & Ho, P. T. P. 1996, *NAT*, 382, 139
- Yalinewich, A. and Sari, R., 2016, *ApJ*, 177, 826
- Yokogawa, S. 2003, Subaru Proposal.
- Young, T. R., & Boris, J. P. 1973, *NRL Mem. Rep.* 2611

Youngblood, A., Ginsburg, A., & Bally, J., 2016, *AJ*, 151, 173

Zapata, L. A., Schmid-Burgk, J., Ho, P. T. P., Rodríguez, L. F. & Menten, K. M., 2009, *ApJ*, 704, 45.

Zapata, L. A., Schmid-Burgk, J., & Menten, K. M., 2011, *A&A*, 529, A24

Zapata, L. A., Schmid-Burgk, J., Pérez-Goytia, N., et al., 2013, *ApJ*, 765, L29

Zel'dovich, Y.B., & Y.P. Raizer, *Physics of shock waves and high-temperature hydrodynamic phenomena*, 464 pp., Academic Press, New York, 1966.

Ziegler, U. 2016 *A&A* 586, A82



# Appendix A

## Speed of sound

Consider a supersonic flow with velocity  $v_2$  and density  $\rho_2$  interacting with a medium at rest with density  $\rho_1$ . The interaction produces two shocks  $S_1$  and  $S_2$  (see Figure (A.1)). Between the shocks there is a growing region that has a uniform velocity  $v_c$  and a uniform pressure  $P$ .  $S_1$ , the forward shock, moves with velocity  $v_{S1}$  and runs into the medium at rest, accelerating it to the velocity  $v_c$ , while  $S_2$ , the reverse shock, moves with velocity  $v_{S2}$  into the impinging flow decelerating it to the same velocity  $v_c$ . The region has two parts: one has density  $\rho'_2$  and temperature  $T'_2$  and is filled by shocked flow 2, while the other part is filled by shocked medium 1 and has density  $\rho'_1$  and temperature  $T'_1$ . Note that the pressure of both regions is however the same. These two regions are separated by a contact discontinuity  $C$ . We further assume that the shocks are strong and parallel. On a frame of reference moving with shock  $S_2$ , we can write,

$$\rho'_2 = \frac{\gamma + 1}{\gamma - 1} \rho_2, \quad (\text{A.1})$$

$$v'_2 = \frac{\gamma - 1}{\gamma + 1} (v_2 - v_{S2}) = v_c - v_{S2}, \quad (\text{A.2})$$

and

$$P = \frac{2}{\gamma + 1} \rho_2 (v_2 - v_{S2})^2, \quad (\text{A.3})$$

where  $v'_2$  is the post- $S_2$  shock flow velocity in this frame of reference and  $\gamma$  is the ratio of specific heats.

Now, in a frame of reference that moves with shock  $S_1$ , the jump conditions across the shock gives,

$$\rho'_1 = \frac{\gamma + 1}{\gamma - 1} \rho_1, \quad (\text{A.4})$$

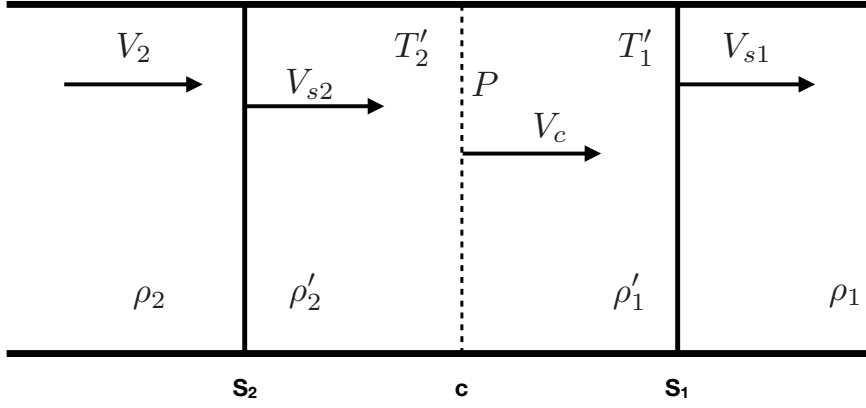


Figure A.1: Scheme of the flow configuration produced by the interaction of a highly supersonic flow 2 with a gas at rest 1.

$$v'_1 = \frac{\gamma - 1}{\gamma + 1}(-v_{S1}) = v_c - v_{S1}, \quad (\text{A.5})$$

and

$$P = \frac{2}{\gamma + 1}\rho_1(-v_{S1})^2, \quad (\text{A.6})$$

where  $v'_1$  is the post- $S_1$  shock velocity in this frame of reference.

From (A3) and (A6) we find

$$v_2 - v_{S2} = \beta v_{S1}, \quad (\text{A.7})$$

where  $\beta = (\rho_1/\rho_2)^{\frac{1}{2}}$ .

Combining (A7) with (A2), (A5) and (A6) we find

$$v_c = \frac{v_2}{1 + \beta}, \quad (\text{A.8})$$



$$v_{S1} = \frac{\gamma + 1}{2(1 + \beta)} v_2, \quad (\text{A.9})$$

$$v_{S2} = \frac{2 + \beta(1 - \gamma)}{2(1 + \beta)} v_2, \quad (\text{A.10})$$

$$P = \frac{\gamma + 1}{2(1 + \beta)^2} \rho_1 v_2^2. \quad (\text{A.11})$$

Finally, the isothermal sound speed behind shock  $S_2$  is,

$$c_2 = \sqrt{\frac{P}{\rho_2}}, \quad (\text{A.12})$$

$$c_2 = \left( \frac{\gamma - 1}{2} \right)^{1/2} \left( \frac{\beta}{1 + \beta} \right) v_2, \quad (\text{A.13})$$

where we have used (A1) and the definition of  $\beta$ .

We can use Eq. (A12) to estimate the sound speed of the gas that was left behind by the reverse shock (shock  $S_2$ ); that is the sound speed inside the plasmon. For this, we identify the impinging flow in the model presented in this Appendix with the original clump. So, if  $v_0$  and  $\rho_{cl}$  are the launch velocity and density of the clump respectively, then, we take,  $v_2 = v_0$ ,  $\rho_2 = \rho_{cl}$  and  $\rho_1$  equal to the density of the ambient medium through which the plasmon is moving  $\rho_a$ . Then,  $c_2$  will be the sound speed inside the plasmon  $c$ , while  $v_c$  (from equation(A8)) will be the initial velocity of the plasmon  $v_0$ . Substituting in Eq. (A.13) we find,

$$c = v_0 \left( \frac{\gamma - 1}{2} \right)^{1/2} \beta. \quad (\text{A.14})$$



# Appendix B

## Numerical densities of the molecules

In this appendix, we present the numerical density of the molecules of the models D5V4, D5.5V4, D6V4, M6.5V4 and D7V4 presented in the chapter. We have taken as sample the models with ejection velocity of  $400 \text{ km s}^{-1}$ .

To facilitate the compression and comparison of the maps we have normalized each of the maps using the maximum density for each molecule. The value of the maximum density, for each of the molecules, can be observed within the corresponding panel. The maps present a range of densities between the maximum value and density of 7 orders of magnitude less.

For the D5V4 (see Table ??) model 2 ages, 200 and 500 years are shown, for the other models only the numerical (standardized) density is presented at 500 yr of evolution.

The maps show the densities of C, C<sub>2</sub>, CH, CH<sub>2</sub>, CO or CO<sub>2</sub> and O, O<sub>2</sub>, H<sub>2</sub>O, HCO, H<sub>2</sub> and OH.

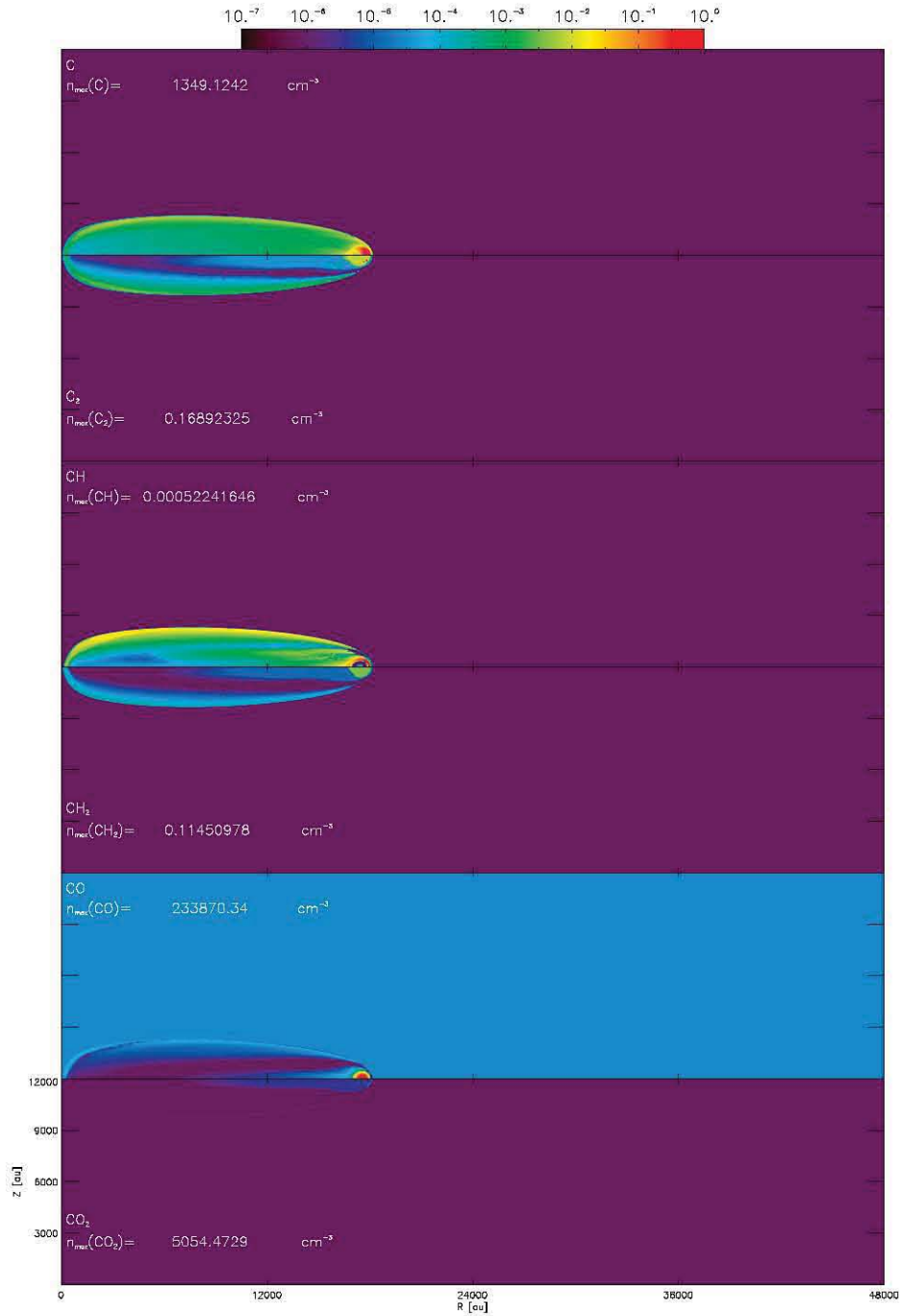


Figure B.1: Normalized numerical density of C, C<sub>2</sub>, CH, CH<sub>2</sub>, CO and CO<sub>2</sub> in descending order for the model D5V4 at 200 yr.

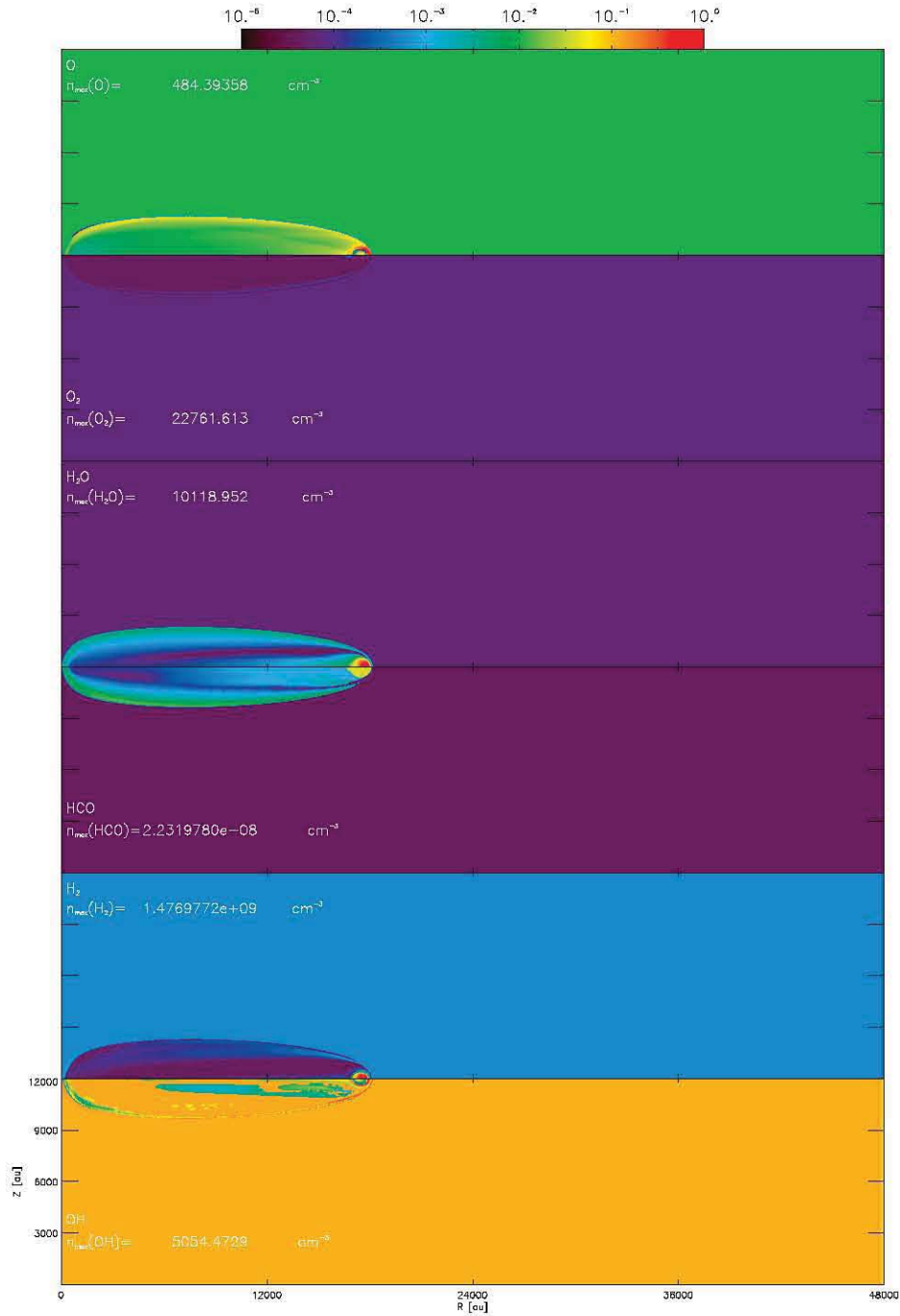


Figure B.2: Normalized numerical density of O, O<sub>2</sub>, H<sub>2</sub>O, HCO, H<sub>2</sub> and OH in descending order for the model D5V4 at 200 yr.

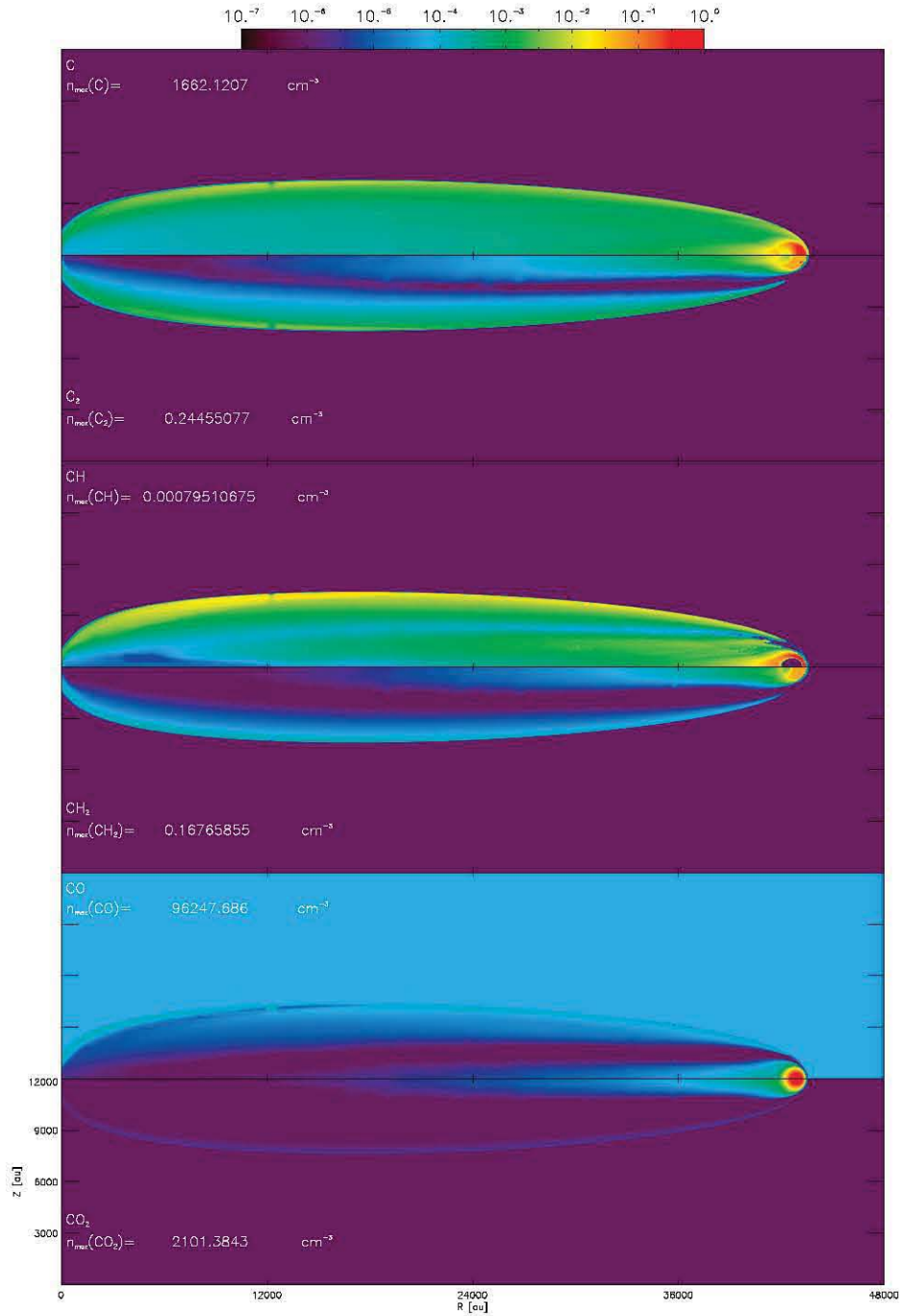


Figure B.3: Normalized numerical density of C,  $\text{C}_2$ , CH,  $\text{CH}_2$ , CO and  $\text{CO}_2$  in descending order for the model D5V4 at 500 yr.

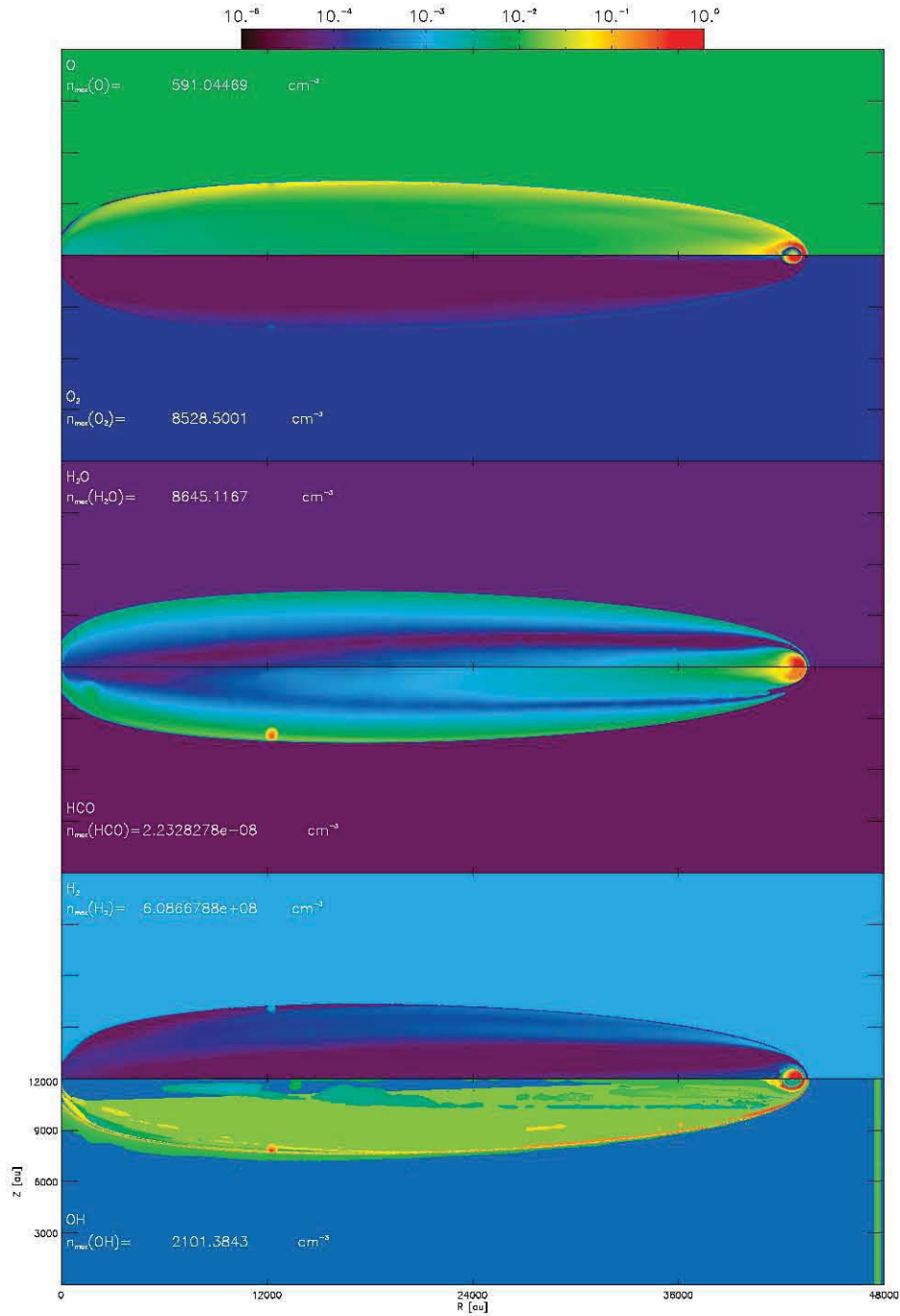


Figure B.4: Normalized numerical density of O, O<sub>2</sub>, H<sub>2</sub>O, HCO, H<sub>2</sub> and OH in descending order for the model D5V4 at 500 yr.

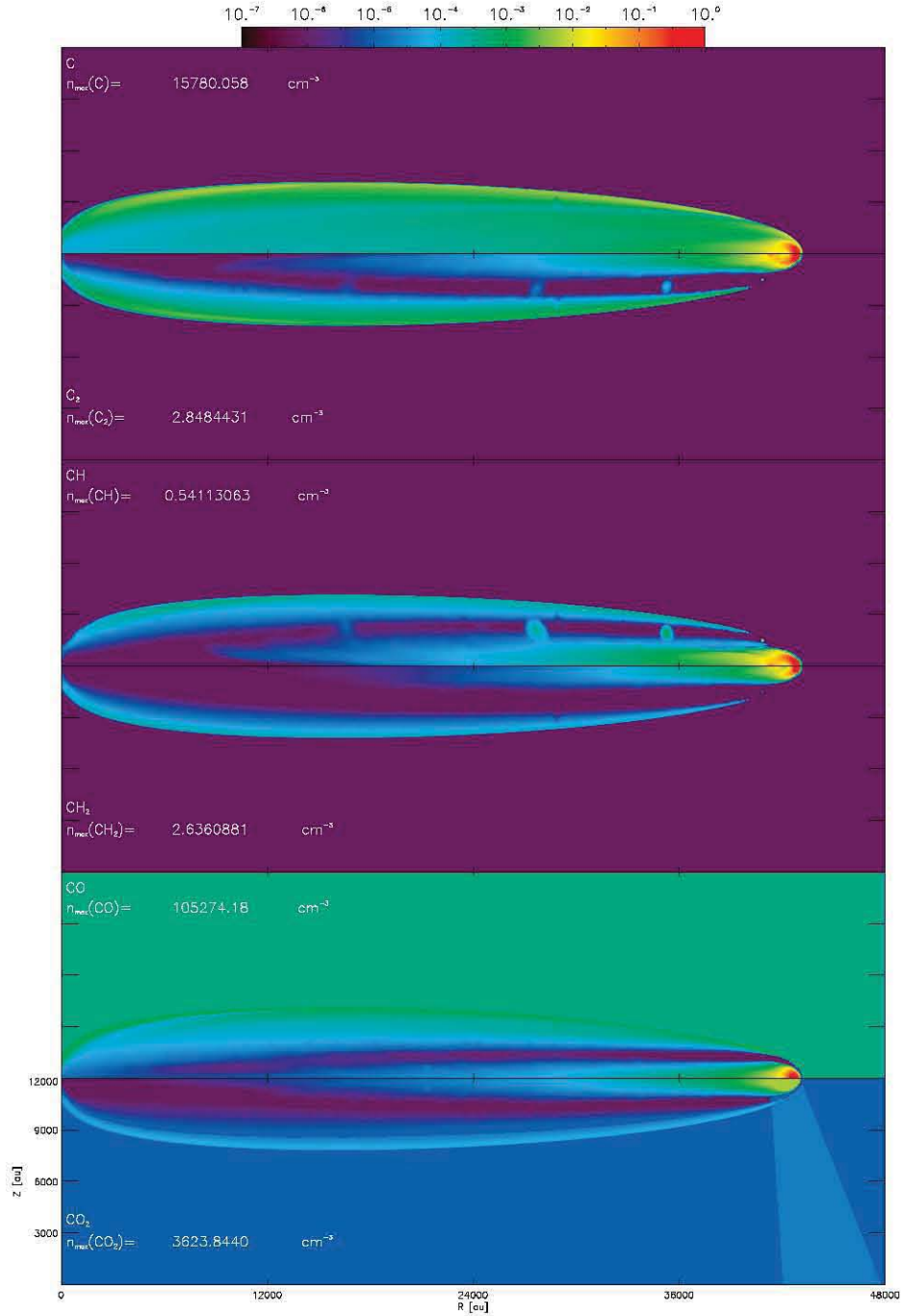


Figure B.5: Normalized numerical density of C, C<sub>2</sub>, CH, CH<sub>2</sub>, CO and CO<sub>2</sub> in descending order for the model D5.5V4 at 500 yr.



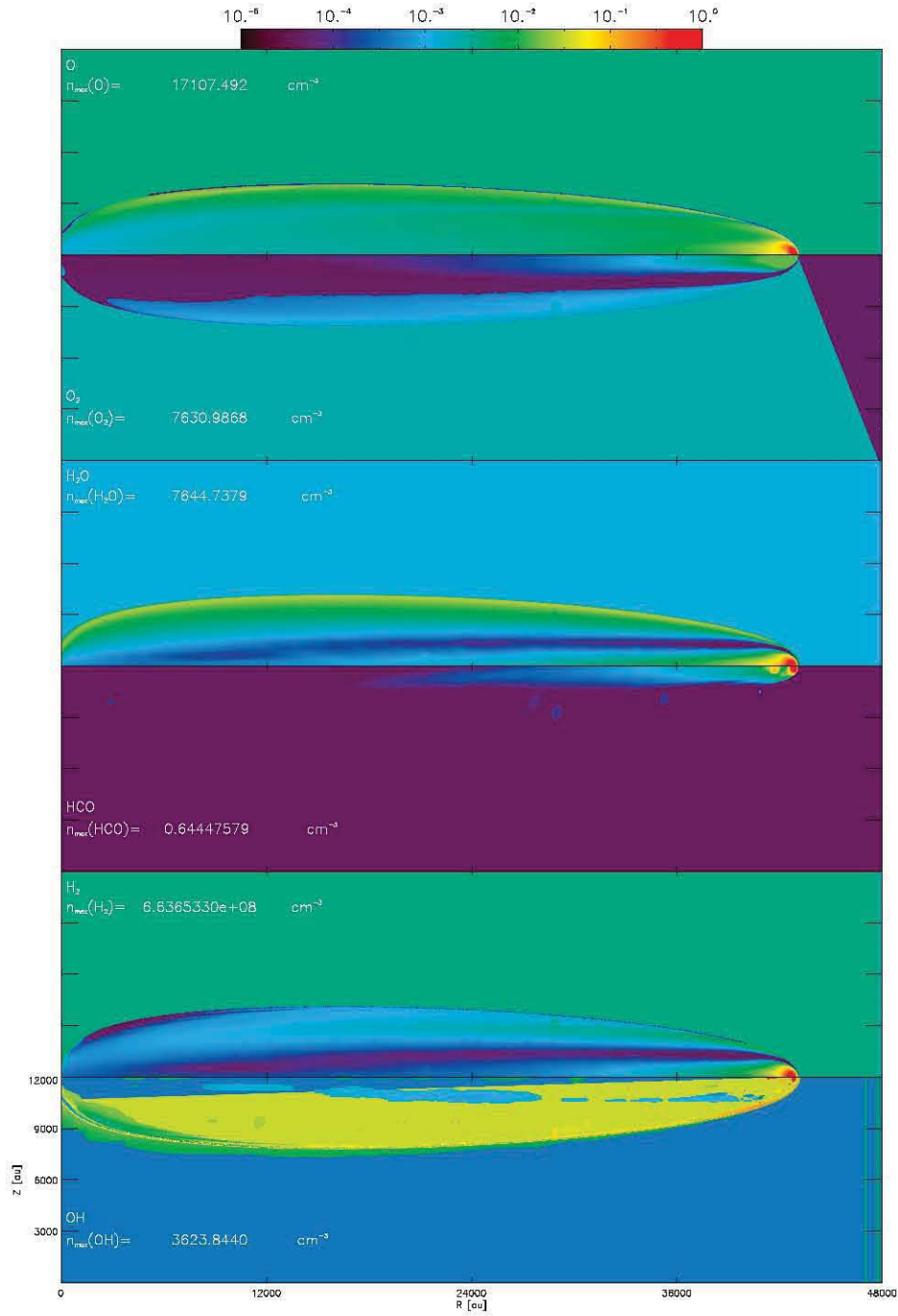


Figure B.6: Normalized numerical density of O, O<sub>2</sub>, H<sub>2</sub>O, HCO, H<sub>2</sub> and OH in descending order for the model D5.5V4 at 500 yr.

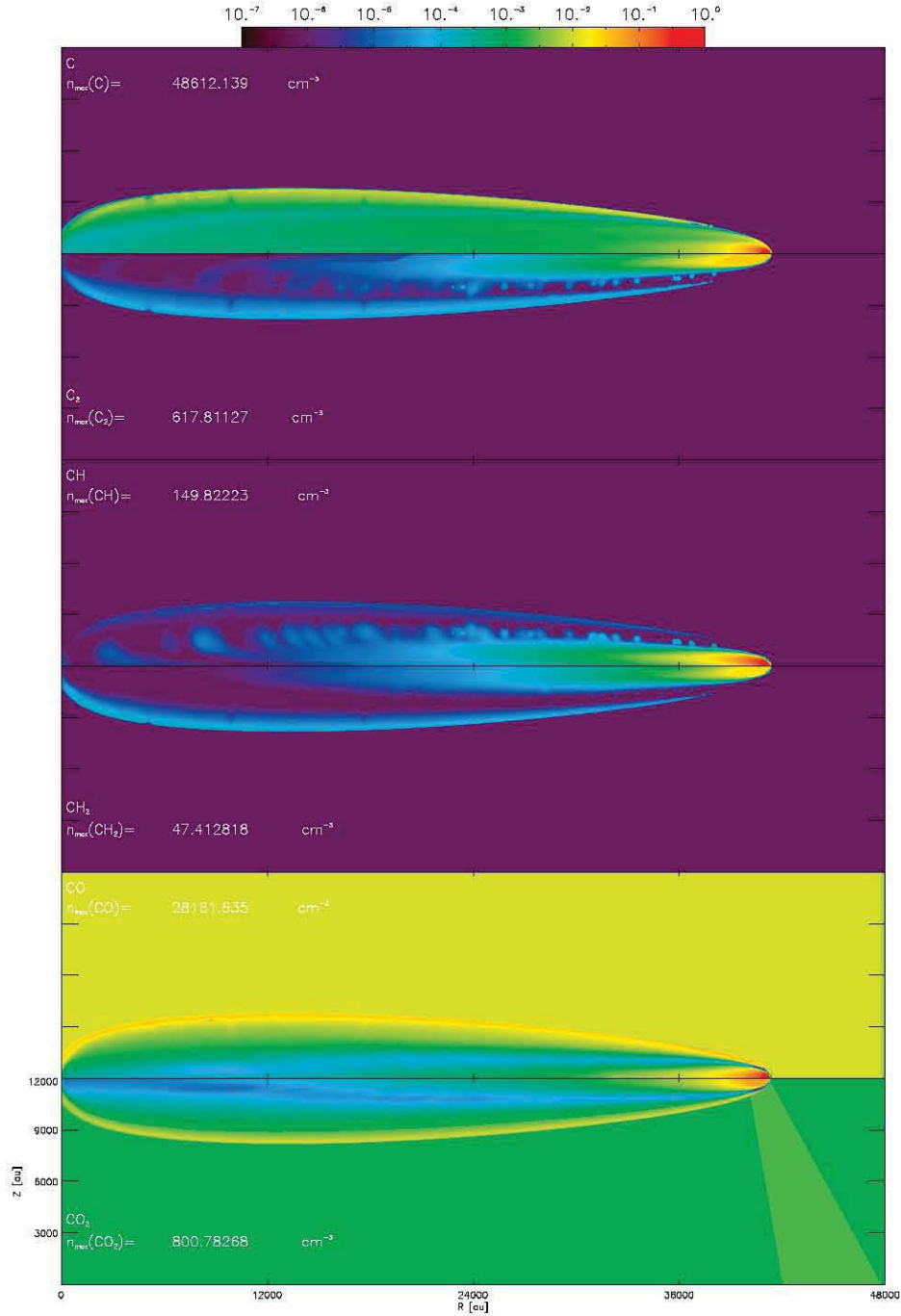


Figure B.7: Normalized numerical density of C, C<sub>2</sub>, CH, CH<sub>2</sub>, CO and CO<sub>2</sub> in descending order for the model D6V4 at 500 yr.

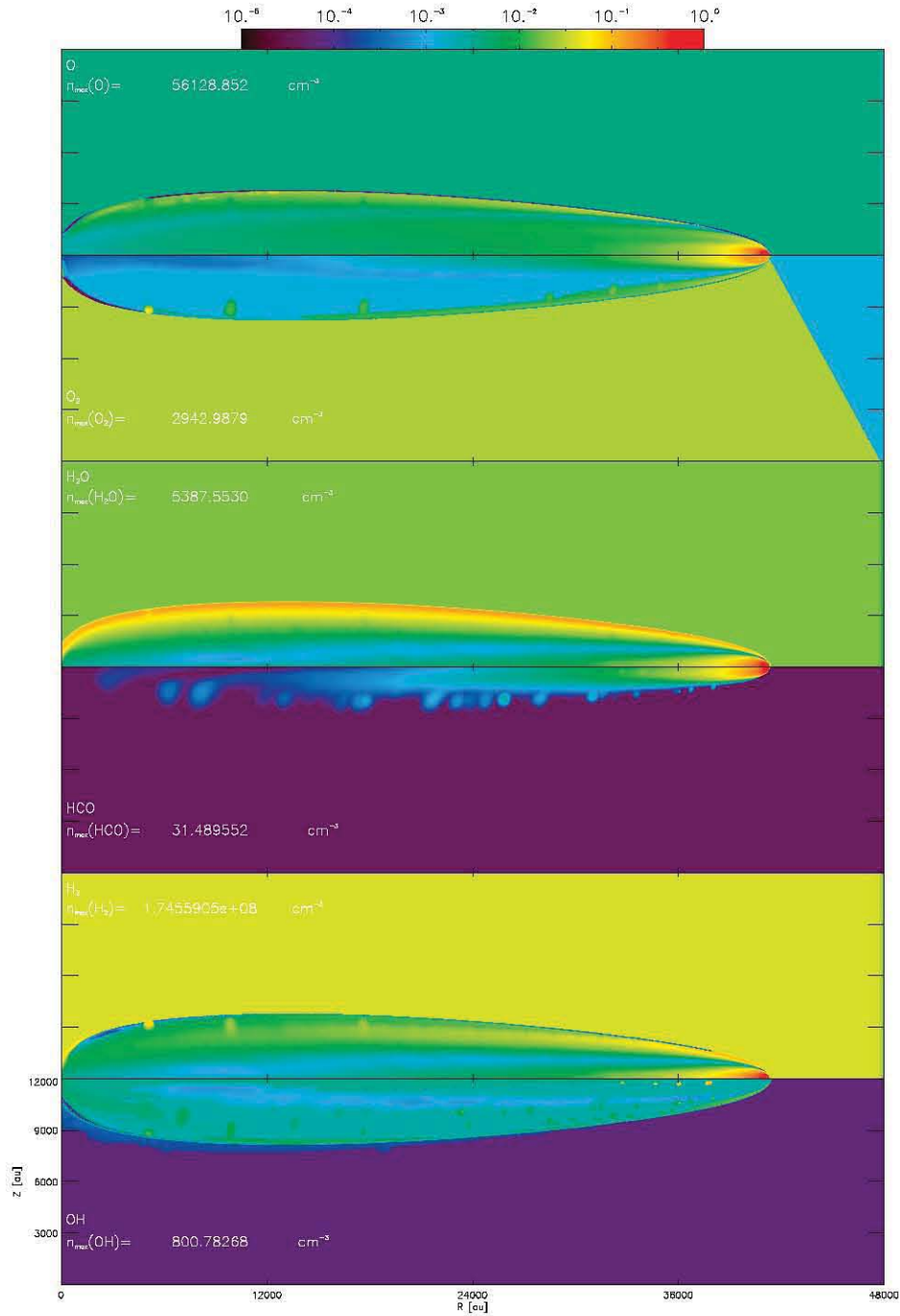


Figure B.8: Normalized numerical density of O, O<sub>2</sub>, H<sub>2</sub>O, HCO, H<sub>2</sub> and OH in descending order for the model D6V4 at 500 yr.

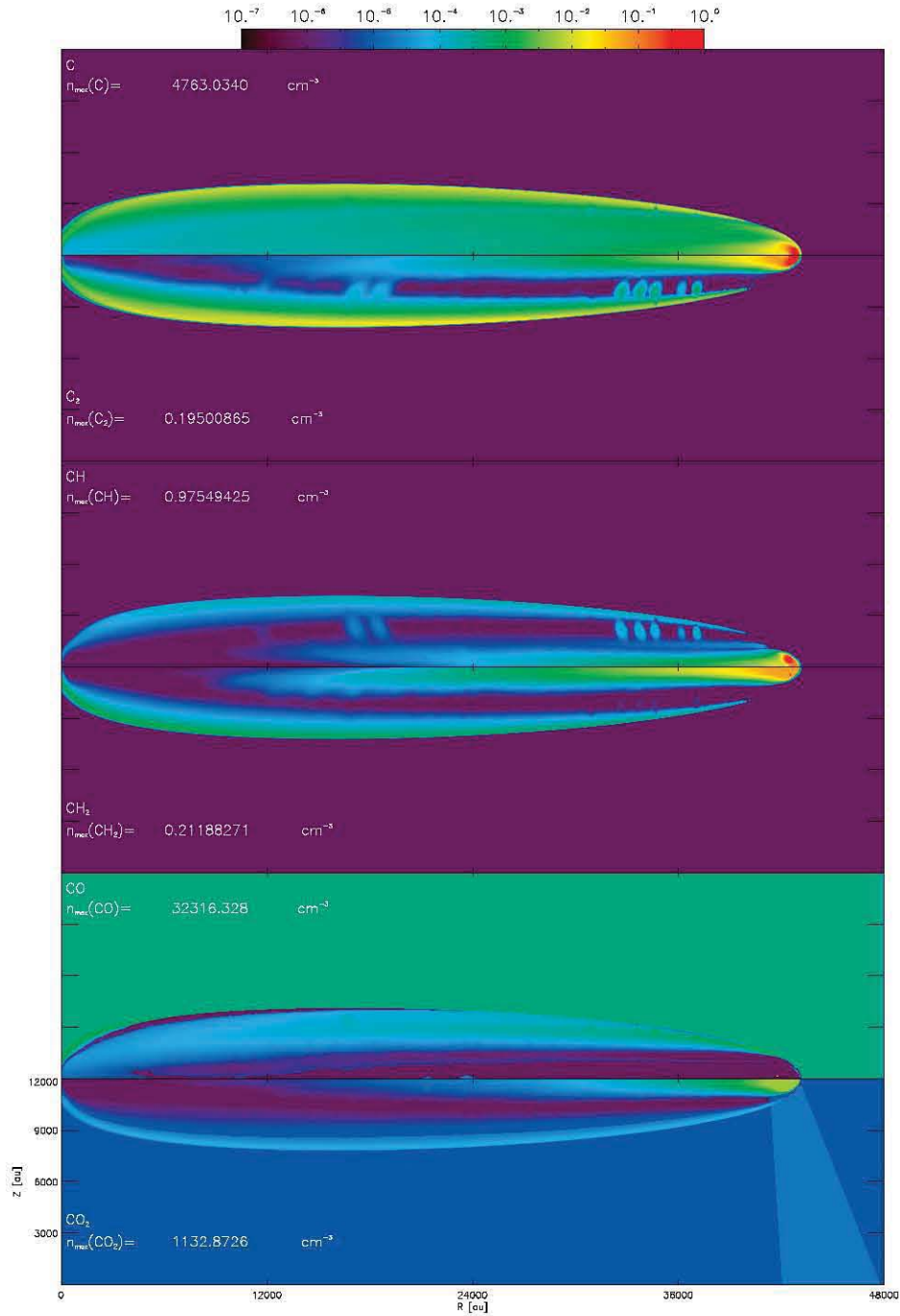


Figure B.9: Normalized numerical density of C, C<sub>2</sub>, CH, CH<sub>2</sub>, CO and CO<sub>2</sub> in descending order for the model D6.5V4 at 500 yr.

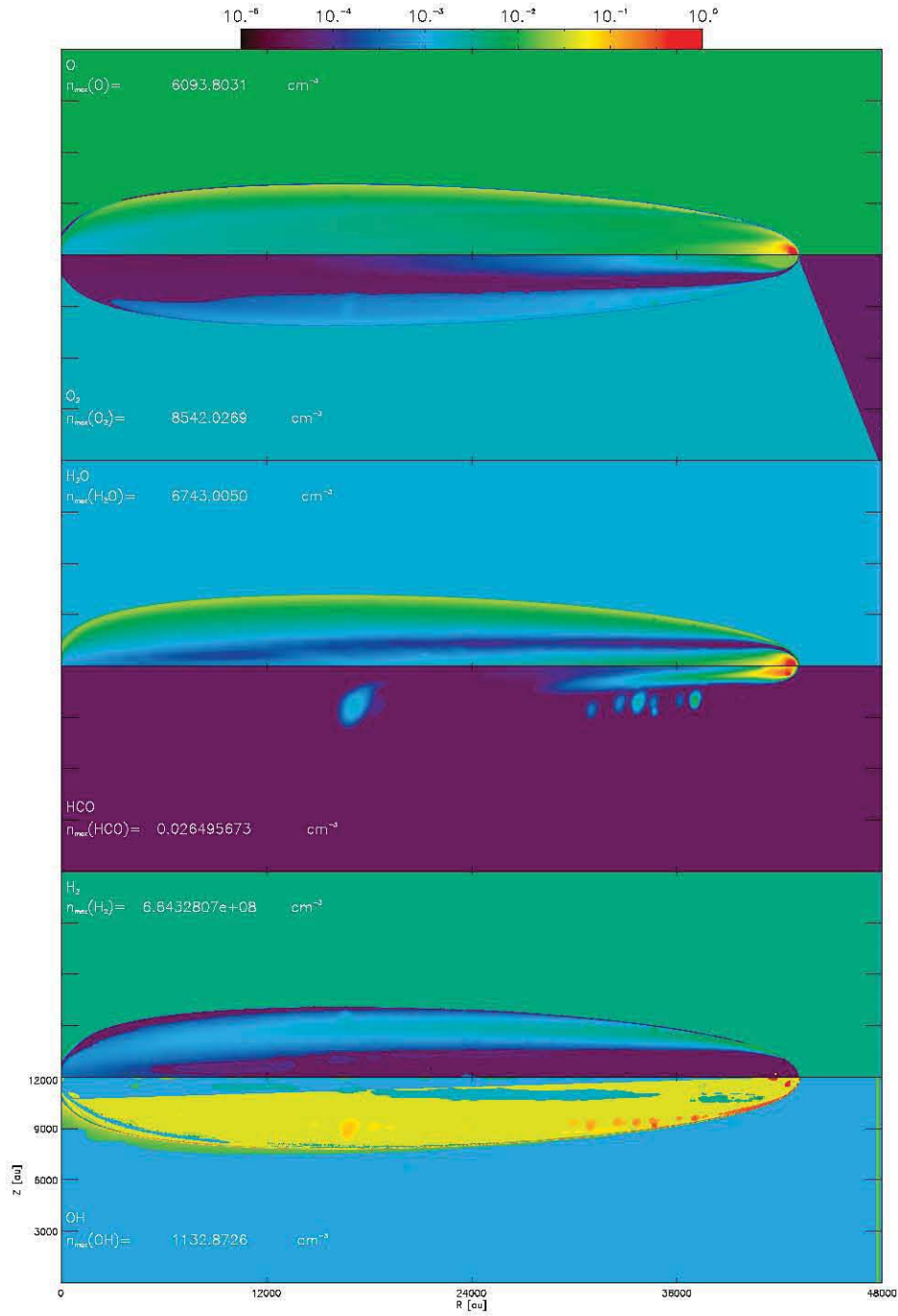


Figure B.10: Normalized numerical density of O, O<sub>2</sub>, H<sub>2</sub>O, HCO, H<sub>2</sub> and OH in descending order for the model D6.5V4 at 500 yr.

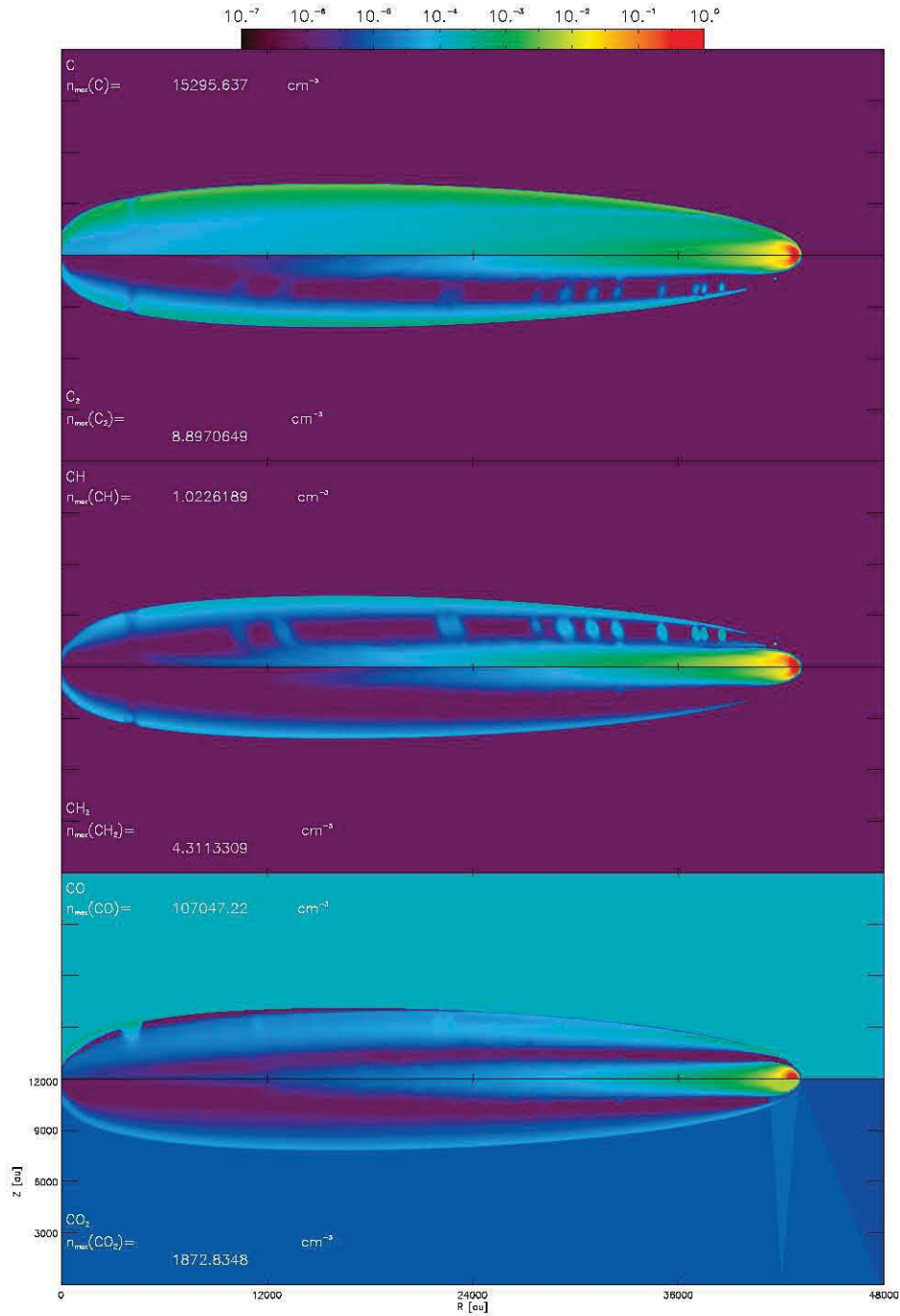


Figure B.11: Normalized numerical density of C, C<sub>2</sub>, CH, CH<sub>2</sub>, CO and CO<sub>2</sub> in descending order for the model D7V4 at 500 yr.

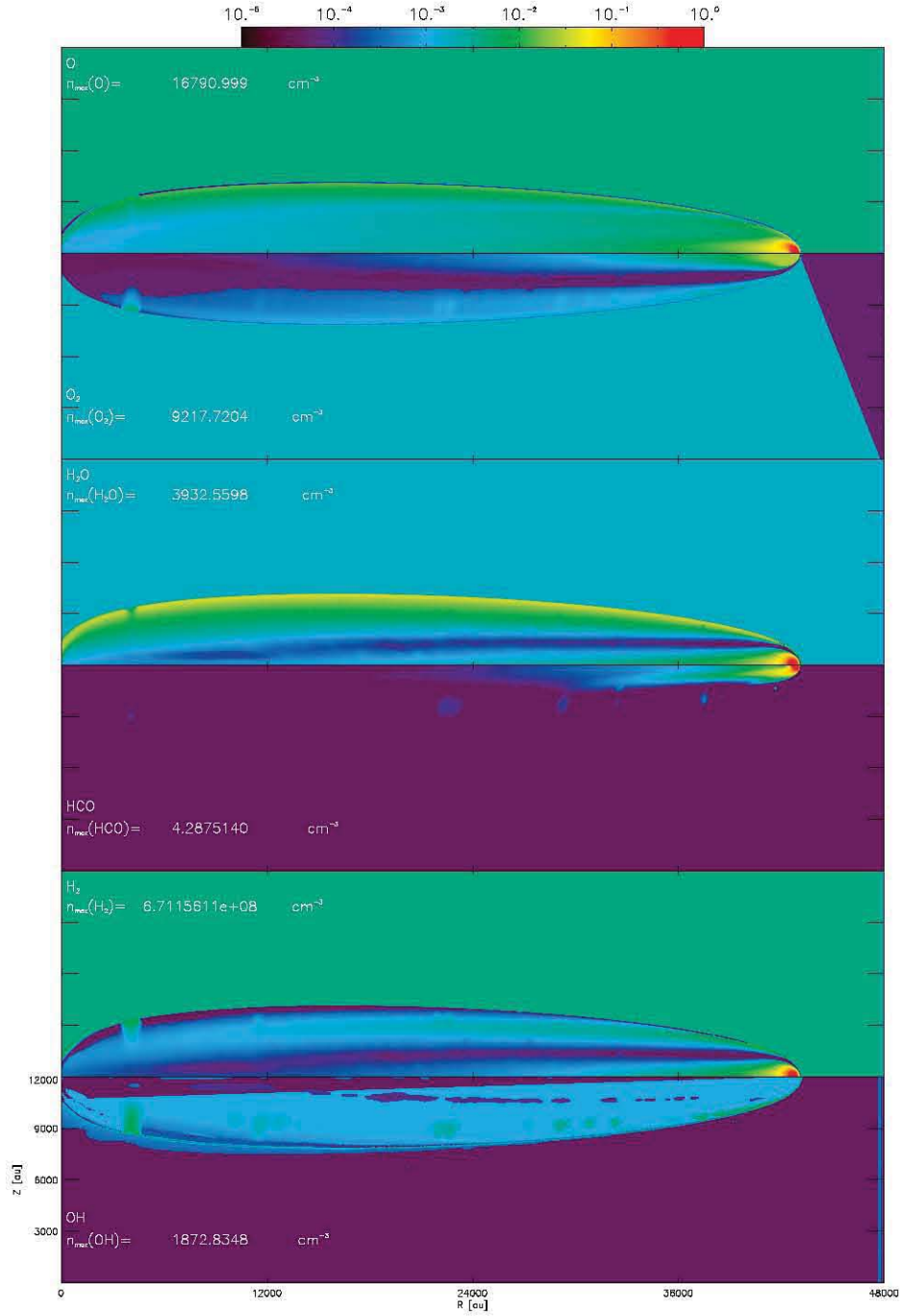


Figure B.12: Normalized numerical density of O, O<sub>2</sub>, H<sub>2</sub>O, HCO, H<sub>2</sub> and OH in descending order for the model D7V4 at 500 yr.





# Appendix C

## Reaction selection

Here, we present the algorithm to select the chemical species from the UMIST12 database. Also, this code writes the reactions equations and the jacobians that are used in KIMYA.




# Appendix D

## Papers related to this thesis



# The Motion of a Losing Mass Plasmon

P. R. Rivera-Ortiz<sup>1,2</sup>, A. Rodríguez-González<sup>1,2</sup> , L. Hernández-Martínez<sup>1</sup>, and J. Cantó<sup>3</sup>

<sup>1</sup> Instituto de Ciencias Nucleares, Universidad Nacional Autónoma de México, Ap. 70-543, 04510 D.F., México; [pedro.rivera@correo.nucleares.unam.mx](mailto:pedro.rivera@correo.nucleares.unam.mx)

<sup>2</sup> LUTH, Observatoire de Paris, PSL, CNRS, UPMC, Univ Paris Diderot, 5 place Jules Janssen, F-92195 Meudon, France

<sup>3</sup> Instituto de Astronomía, Universidad Nacional Autónoma de México, Ap. 70-264, 04510 D.F., México

Received 2018 November 13; revised 2019 January 30; accepted 2019 February 7; published 2019 March 19

## Abstract

The interaction of a high velocity clump of gas has been described by the plasmon model, which considers balance between ram pressure and the internal stratified structure of the decelerated clump. In this paper we propose an analytical model to describe the mass loss of such a clump due the interaction with the environment, describing its influence on the plasmon dynamics. We carry out comparisons between an analytic model and axisymmetric gas dynamic simulations of plasmon evolution. From our simulations we were able to find the values of the friction constants  $\alpha$  and  $\lambda$ . Comparing with the complete analytic model from which we can infer the position and the mass loss of the clump as a function of the clump's density and the environment ratio.

*Key words:* ISM: general – ISM: jets and outflows – ISM: kinematics and dynamics – shock waves

## 1. Introduction

The problem of a wind/molecular cloud interaction has been studied at length in the past. De Young & Axford (1967, hereafter DA) described the motion of a clump decelerated by the ram pressure and determined the lifetime of the plasmon. They applied this model to Cygnus A and concluded that analyzing the dynamics of plasmons should reduce their free parameters. It became a very popular model to explain confinement of radio lobes propagating through the intergalactic medium (Ubachukwu et al. 1991; Daly 1994), models of radio-loud quasars (Daly 1995), and models of the optical narrow-line regions of Seyfert galaxies (Taylor et al. 1992; Veilleux et al. 1993). Cantó et al. (1998; hereafter C98) rederived the plasmon solution, adding the centrifugal pressure to obtain a modified plasmon profile.

In most cases it is difficult to calculate the real age of an astronomical plasmon because there is no clear information about deceleration and most plasmons are isolated so there is not enough information about the static medium. To solve this problem a set of several plasmons with an noticeable deceleration moving under similar restrictions is needed.

Orion BN/KL is an ideal laboratory to prove the plasmon solution, because it has an almost isotropic and explosive outflow that could be produced by the nonhierarchical close dynamic interaction of a forming multiple-star system (Zapata et al. 2009). In this region there are more than a hundred filamentary structures known as fingers that allow us to estimate a dynamical age between 1000 and 500 yr, assuming no deceleration. Nevertheless, there is observational evidence that the longest fingers detected in H<sub>2</sub> emission are losing speed, probing their interaction with the environment (Bally et al. 2011). It is a very interesting star formation region that due to its distance, at 414 pc, allows us to determine its characteristics with enough detail. Therefore, we also can model the physics using theoretical and numerical models, using some observational constrains. Some of these models have achieved important results as determining the dynamical age and the energy of the explosive event. Nevertheless, there are important questions that deserve attention and are not resolved yet, such as the real age of the event, the mechanism

that can generate such distribution of the fingers, as well as their ejection velocity since there is evidence of a drag force.

The effect of a drag force is necessary to understand the real motion of a plasmon. Several numerical simulations have shown a deceleration effect greater than that expected by ram pressure (Yalinewich & Sari 2016), but it has not been deeply analyzed since cooling effects were not included.

The destruction of the original clump was also considered in Raga et al. (1998) in their study of the interaction of a fast wind impinging into a compact spherical cloud. They concluded that the motion is affected by the detachment of material of the cloud, which results in a limited application of their model.

Then, the assumption that a clump has no deceleration or a deceleration according to models with constant mass, can lead to an overestimate of the age of astrophysical outflows.

In this work, we use the DA solution to propose a mass-loss rate for a plasmon and we obtained its equation of motion. We compare results of this analytic model with numerical simulations using Orion BN/KL plausible ejection conditions. We presented analytic (Section 2) and numerical (Section 3) models of a deceleration of the clumps as a function of ratio density when the mass-loss rate is considered. We present a comparison between the analytic and numerical models and a prediction of the lifetime of clumps assuming similar conditions to the system Orion BN/KL in Section 4. Finally, we present our conclusions in Section 5.

## 2. Analytical Model

### 2.1. DA's Plasmon

DA studied the problem of a clump of gas moving through a uniform environment. They found a solution (the “plasmon” solution) based on the balance between the ram pressure of the environment and the stratified thermal pressure of the decelerating clump. For a clump of mass  $M$ , isothermal sound speed  $c$ , moving supersonically with velocity  $v$  through a medium of density  $\rho_a$ , the plasmon adopts a pressure and density stratification given by

$$P = P_0 e^{-x/h}, \quad \rho = \rho_0 e^{-x/h}, \quad (1)$$

## OBTAINING THE INITIAL CONDITIONS OF THE ORION BN/KL'S FINGERS.

P. R. RIVERA-ORTIZ<sup>1,2</sup>, A. RODRÍGUEZ-GONZÁLEZ<sup>1,2</sup>, L. HERNÁNDEZ-MARTÍNEZ<sup>1</sup>, J. CANTÓ<sup>3</sup>

<sup>1</sup> Instituto de Ciencias Nucleares, Universidad Nacional Autónoma de México, Ap. 70-543, 04510 D.F., México

<sup>2</sup> LUTH, Observatoire de Paris, PSL, CNRS, UPMC, Univ Paris Diderot, F-92195 Meudon, France and

<sup>3</sup> Instituto de Astronomía, Universidad Nacional Autónoma de México, Ap. 70-264, 04510 D.F., México

*Draft version April 22, 2019*

### ABSTRACT

Orion BN/KL is an example of a poorly understood phenomena in star forming regions involving the close interaction. The filamentary structure, the great variety of molecules, the energy involved in the event and the mass of the region suggest a contribution in the enrichment of the interstellar medium. Nevertheless, the frequency and duration of other events like this have not been determined. In particular, the Orion fingers have dynamical ages between 500 and 4000 yr, which is in contradiction with the idea of a single event. In this paper we explore several analytic models taking into account the interaction of a clump and the environment and the resulting deceleration to explain the age discrepancy of the Orion fingers. We select the more probable model to infer the initial conditions of the explosion and estimate a lifetime for the region.

*Keywords:* orion, fingers — age

### 1. INTRODUCTION

Orion BN/KL is a very interesting star formation region that is associated to an explosive event that is poorly understood. In particular it contains around 200 hundred filamentary structures in H<sub>2</sub> emission known as Orion fingers, which could be formed by the close interaction of a protostellar cluster (Zapata et al. 2009, Bally et al. (2011) and references therein). The age of the event have been determined by several authors using different techniques. Zapata et al. 2009 noted the properties of a set of fingers in the J=2-1 CO transition which can be associated to H<sub>2</sub> fingers and, assuming an age, determined the 3D structure and obtained a most probable age of approximately 500 yr. This is in agreement with the age estimated by Rodríguez et al. (2017) using the runaway objects I, n and BN and the age of the expanding the bubble centered in the possible origin of the region. Bally et al. (2011) analyzed the projection of the H<sub>2</sub> fingers position and velocity. For each finger, they found an individual age that is between 1000 and 500 yr. This is in contradiction with the idea that Orion BN/KL was produced in a single explosive event and that the expelled clumps are in ballistic motion, so they concluded that there must be a deceleration effect. There is a chance that the fingers could be originated at different moments. Perhaps, there is an unexplored mechanism to produce such an extended structure. The machine-gun model has been mentioned as a possible explanation, but previous models (Raga & Biro 1993), even when they are not collimated, it is far from being as isotropic as the Orion fingers. On the other hand, the runaway stars (Rodríguez et al. 2017), the expansion of the hot core (Zapata et al., 2011) and the age determined by the CO fingers (Zapata et al., 2009), are strong evidence of a single and simultaneous event. Then, adopting a proper age of  $T = 544$  yr, as calculated by Rodríguez et al. (2017), we can use the several models to obtain the physical conditions of the ejection. The mass-loss plasmon has a implicit dependence on its own size and it can be used to find better

restrictions on the ejection mechanism. This makes important to understand the dynamics of the fingers with the interstellar medium. There are several attempts to describe the interaction of a moving cloud against a static medium. De Young & Axford (1967) (hereafter DA) analyzed the plasmon problem, which consists in a moving cloud that takes a density structure, and derived its equation of motion. Cantó et al. (1998) improved the plasmon solution including centrifugal pressure. Also, Raga et al. (1998) proposed the equation of motion of a static spherical cloud that is accelerated with a high velocity wind due to the ram pressure. More recently, Rivera-Ortiz et al. (2019) (hereafter RO19) proposed a modification to the plasmon problem, adding a mass loss rate, which can modify a plasmon dynamic history if it is embedded in a high density environment. Then the dynamical analysis of the motion of the Orion fingers could lead to a better understanding of the conditions that formed such a structure. Bally et al. (2015) performed numerical simulations of the fingers using observational restraints and obtained a notable resemblance to the actual fingers. Nevertheless, as they described, the interpretation of such simulations is limited since they used an adiabatic system, and the cooling length is much shorter than the total length of the longest fingers. Therefore, more detailed numerical solutions and an adequate analytic model can be helpful to determine the physical conditions and possibly the ejection mechanism of the fingers, which can be helpful to understand the relevance and duration of similar events in the star forming processes. In this work we used different solutions, published in the literature for the clump motion in homogeneous media, to obtain the physical properties of Orion BN/KL components. In Section 2 we present the sample of objects to be analyzed, in Section 3 we present the estimation of the properties for the clumps before the explosive event that generated the Orion fingers in Orion BN/KL.. Finally the conclusions are presented in Section 4.

### 2. OBSERVATIONS

## KIMYA, A CODE FOR SOLVING CHEMICAL REACTION NETWORKS IN ASTROPHYSICS

A. Castellanos-Ramírez, A. Rodríguez-González, P. R. Rivera-Ortíz, A. C. Raga, R. Navarro-González, and A. Esquivel

Instituto de Ciencias Nucleares, UNAM, México.

Received January 30 2018; accepted April 9 2018

### ABSTRACT

KIMYA is a new code for solving the system of differential equations describing the temporal behavior of a chemical network. This paper presents a simple and easy to implement numerical method and tests of its accuracy. KIMYA was designed for incorporating a chemical network into multi-dimensional gasdynamical simulations. In order to test our code we compute three numerical simulations: a model of the chemical evolution of a dark cloud (which we compare with previous calculations), and a model of nitric oxide formation during a lightning discharge simulated with a laser pulse. The latter is done with both a single parcel calculation, as well as a fully hydrodynamical/chemical model, which we compare with results from a laboratory experiment.

### RESUMEN

KIMYA es un nuevo código para resolver el sistema de ecuaciones diferenciales que describe el comportamiento temporal de una red química. En este artículo presentamos un método numérico sencillo y fácil de implementar, y una evaluación de su precisión. KIMYA fue diseñado para incorporar una red química en simulaciones hidrodinámicas multidimensionales. Para probar nuestro código hacemos tres simulaciones numéricas: un modelo de la evolución química de una nube oscura (el cual comparamos con cálculos anteriores) y un modelo de la formación de óxido nítrico durante una descarga de relámpago simulada con un pulso de láser. Este último lo hacemos tanto con un cálculo de una única parcela, como dentro de un cálculo hidrodinámico/químico, y lo comparamos con resultados de un experimento de laboratorio.

*Key Words:* astrochemistry — hydrodynamics — ISM: molecules — methods: numerical — molecular processes — shock waves

### 1. INTRODUCTION

Chemical kinetics networks have applications in atmospheric chemistry, combustion, detonations and biological systems as well as in planetary, stellar and interstellar astrophysics.

In order to follow the time-evolution of a chemical system, one needs to determine the reagents and products involved, as well as the relevant chemical reactions. The resulting rate equations have to be integrated in time together with the equations that describe the time-evolution of the reactive fluid (these could be the gasdynamic or the magnetohydrodynamic equations in 1, 2 or 3D, which are coupled to the chemical network through the equation of state

and possible energy gain/loss terms). The simplest possible model is a “0D” approximation, in which the chemical rate equations are integrated for a single, homogeneous parcel in which either a constant or a time-dependent density (or pressure) and temperature are imposed.

In order to follow the temporal evolution of the molecular composition of a gas, one needs to integrate the density rate of change equations for the different species contained in the gas. In order to do this, one has to construct a chemical network gathering the creation and destruction reactions for all of the different species. Such a chemical network is a system of ordinary differential equations (ODEs).

# Modelling the CO streams in the Orion BN/KL region

P.R. Rivera-Ortiz<sup>1, \*</sup>, A. Rodríguez-González<sup>1,2</sup>, A. Castellanos-Ramírez<sup>1</sup>,  
A.C. Raga<sup>1</sup>, R. Navarro-González<sup>1</sup>, L. Hernández-Martínez<sup>1</sup>, J. Cantó<sup>3</sup>,  
F. Robles-Valdez<sup>4</sup>, A. Esquivel<sup>1,5</sup> & L. Zapata<sup>6</sup>.

<sup>1</sup> *Instituto de Ciencias Nucleares, Universidad Nacional Autónoma de México, Ap. 70-543, 04510 D.F., México.*

<sup>2</sup> *LUTH, Observatoire de Paris, PSL, CNRS, UMPC, Univ Paris Diderot, 5 place Jules Janssen, F-92195 Meudon, France.*

<sup>3</sup> *Instituto de Astronomía, Universidad Nacional Autónoma de México, Ap. 70-264, 04510 D.F., México.*

<sup>4</sup> *Departamento de Astronomía, Universidad de Guanajuato Ap. 144, 36000 Guanajuato, México.*

<sup>5</sup> *Instituto de Astronomía Teórica y Experimental, Universidad Nacional de Córdoba, X5000BGR Córdoba, Argentina.*

Accepted XXX. Received YYY; in original form ZZZ

## ABSTRACT

We present numerical simulations of reactive flows for modeling the CO streams observed in OMC1 Orion BN/KL. We have considered 14 chemical species, a cooling function for atomic and molecular gas, and the heating through cosmic rays. Our numerical simulations explore different ejection velocities, interstellar medium densities and CO content. Using the CO density and temperature, we have calculated the CO emissivity for every cell in our axisymmetric simulation, and we have built CO maps that allow us to see the CO emitting regions of the stream.

We find that the peak of the CO emission is related with the ambient density. The CO peak is located at  $\epsilon = 0.6$  times of the length of the stream at  $t < 300$  yr evolutionary times, and at  $\epsilon = 0.75$  for later ( $t \sim 500$  yr) times.

## 1 INTRODUCTION

The BN/KL region, which has a great diversity of molecules, is located behind the Orion Nebula (at a distance of 414 pc from the Sun). This region has a breaking-up multiple stellar system, an expanding molecular bubble and a peculiar outflow with about 200 filamentary structures, known as “fingers” or “streams”. These three components seem to have originated in the same ejected event approximately 500 yr ago. The most accepted qualitative model for this object (Bally et al. 2005) proposes that a single event ejection could have been caused by a stellar merger or the dynamic rearrangement of a non-hierarchical system of young, massive stars or proto-stars. There is relatively strong evidence supporting this model (Zapata et al. 2009, Bally et al. 2011, Goddi et al. 2011).

The OMC1 “fingers” were discovered by Allen & Burton (1993) as H<sub>2</sub> 2.1 $\mu$ m features emanating outwards from the central region of OMC-1 and terminating in a series of Herbig-Haro (HH) objects, which had previously been observed as [O I] 6300, high-speed “bullets” by Axon & Taylor (1993). These HH objects have been detected in other optical lines (O’Dell et al. 1997). The kinematics of the H<sub>2</sub> emission features has been studied with Fabry-Perot observations (Chrysostomou et al. 1997, Salas et al. 1999) and proper motion measurements (Bally et al. 2011). The proper motions of some of the optically detected bullets have also been presented by Doi et al. 2002.

Following Bally (2011 and 2015) there are about 200 H<sub>2</sub> fingers, which present a distribution of longer features to the

NW, shorter fingers to the SE and SW, and very few and weak features to the E and NE. The longer fingers have a length of  $\sim 50000$  au (using the distance of 414 pc obtained in Menten 2007) and diameters between 800 to 3200 au. The shorter filaments are narrower, more numerous, and tend to overlap. The heads of the H<sub>2</sub> fingers (seen in H<sub>2</sub> and [Fe II] IR lines and optically as HH objects, see above) have diameters  $\sim 40 \rightarrow 400$  au. The well defined, longer filaments have velocities (derived from the radial velocity and proper motion measurements) of  $\sim 350$  km s<sup>-1</sup>.

The lengths and velocities of the fingers are consistent with an origin in a single ejection event (for all fingers)  $\sim 500 \rightarrow 1000$  yr ago. However, there is evidence of a substantial braking of the motion of the heads of those fingers over their evolution (Bally et al. 2011). An estimation of the total kinetic energy of the fingers is about  $10^{47} \rightarrow 10^{48}$  erg, which can be interpreted as an estimation of the energy of an “ejection event” that gave rise to the present-day fingers (see Bally et al. 2011).

This region also has an extended CO outflow which was first detected in single-dish observations by Kwan & Scoville (1976). In more recent interferometric observations, this outflow has been resolved into a system of CO “streams” (Zapata et al. 2009, Bally et al. 2017). The CO streams show a more isotropic direction distribution than the H<sub>2</sub> fingers, with several streams emitting an infrared emission because of the J=2 $\rightarrow$ 1 rotational transition in CO molecule, into the NW. The total mass moving with velocities larger than





# List of Figures

|     |   |    |
|-----|---|----|
| 1.1 | Orion BN/KL region . . . . .  | 6  |
| 1.2 | Proper motions . . . . .  | 7  |
| 1.3 | H <sub>2</sub> and CO emission . . . . .  | 10 |
| 2.1 | Snapshots of a plasmon at different ages . . . . .  | 23 |
| 2.2 | History of physical properties of the simulated plasmons with $v=300 \text{ km s}^{-1}$ . . . . . | 26 |
| 2.3 | History of physical properties of the simulated plasmons with $v=500 \text{ km s}^{-1}$ . . . . . | 28 |
| 2.4 | Mass of a clump as a function of the velocity . . . . .   | 29 |
| 2.5 | Friction constant $\alpha$ . . . . .  | 29 |
| 2.6 | Dimensionless velocity and time for the dynamical models . . . . .                                | 30 |
| 2.7 | Dimensionless position and time of the dynamical and numerical models . . . . .                   | 31 |
| 3.1 | Data sets used in this work to apply the dynamical models . . . . .                               | 38 |
| 3.2 | Kinematic age assuming no deceleration . . . . .  | 39 |
| 3.3 | Trajectories for a constant ejection velocity or constant ejection mass at a fixed time . . . . . | 42 |
| 3.4 | RO19 model applied to the data sets . . . . .   | 44 |
| 3.5 | Mass distribution . . . . .   | 45 |
| 3.6 | Velocity distribution . . . . .   | 46 |
| 3.7 | Lifetime of the fingers . . . . .   | 47 |
| 3.8 | Lifetime of the fingers . . . . .   | 47 |
| 3.9 | Actual distance and age compared to the final distance and lifetime . . . . .                     | 48 |
| 4.1 | KIMYA flow chart . . . . .  | 59 |
| 4.2 | Densities of species $a, b, c$ and $d$ as a function of time . . . . .                            | 62 |
| 4.3 | Temporal evolution of the shock wave temperature and the plasma temperature . . . . .             | 67 |

|      |   |     |
|------|---|-----|
| 4.4  | The variation of the nitric oxide yield as a function of the CO <sub>2</sub> mixing ratio . . . . .   | 68  |
| 4.5  | Evolution of the plasma temperature . . . . .   | 69  |
| 4.6  | Radius of the simulated bubble versus time using different initial temperatures . . .   | 70  |
| 4.7  | Density and temperature maps . . . . .  | 71  |
| 4.8  | Density maps of CO <sub>2</sub> , NO, O <sub>3</sub> and NO <sub>2</sub> at $t = 2 \times 10^{-6}$ . . . . .  | 71  |
| 4.9  | The variation of the N <sub>2</sub> O, NO <sub>2</sub> , NO <sub>3</sub> , O <sub>2</sub> , O <sub>3</sub> and N yields as a function of the CO <sub>2</sub> mixing ratio in the reactive flow numerical simulations. . . . .   | 73  |
| 4.10 | Computational time vs. number of reactions . . . . .  | 74  |
| 5.1  | Snapshots from the numerical simulations showing the number density. Each pair of panel compares two models with initial velocity of 500 km s <sup>-1</sup> and with interstellar medium density of 10 <sup>5</sup> (up) and 10 <sup>7</sup> (down) cm <sup>-3</sup> at $t = 200, 300$ and 400 years. . .   | 83  |
| 5.2  | Snapshots from the numerical simulations showing the integrated CO emission and the gas number density. The panels are showing the evolutionary times 100, 200 300 and 400 yr top, top-middle, bottom-middle, bottom, respectively, for D5V5. . . . .   | 87  |
| 5.3  | The integrated CO emission versus velocity of the gas. The colors represent the CO, J=2-1 emission in Jansky. The evolutionary time at 100, 200, 300, 400, 500, 600 and 700 yr for the model D6V3 is presented. The size of the symbols decrease for lower emissions and it is zero if the gas velocity is lower than the local sound speed. . . . .  | 89  |
| 5.4  | PV synthetic diagram for the model . . . . .  | 90  |
| 5.5  | Observed PV . . . . .   | 90  |
| 5.6  | The ratio between the position of the maximum in the emission of CO and total length of the CO finger. The solid, dashed and dotted lines are the models with interstellar medium density of 10 <sup>4</sup> , 10 <sup>5</sup> and 10 <sup>6</sup> cm <sup>-3</sup> , respectively, and the upper panel present the epsilon values for the models with ejection velocity of 300 km s <sup>-1</sup> , the middle panel shows the model with ejection velocity of 400 km s <sup>-1</sup> and the models with ejection velocities of 500 km s <sup>-1</sup> are presented in the bottom panel. . . . . | 92  |
| A.1  | Scheme of the flow configuration produced by the interaction of a highly supersonic flow 2 with a gas at rest 1. . . . .  | 106 |
| B.1  | Normalized numerical density of C, C <sub>2</sub> , CH, CH <sub>2</sub> , CO and CO <sub>2</sub> in descending order for the model D5V4 at 200 yr. . . . .  | 110 |
| B.2  | Normalized numerical density of C, C <sub>2</sub> , CH, CH <sub>2</sub> , CO and CO <sub>2</sub> in descending order for the model D5V4 at 200 yr. . . . .  | 111 |
| B.3  | The same as B1 for the model D5V4 and 500 years . . . . .   | 112 |

|      |   |     |
|------|---|-----|
| B.4  | The same as B2 for the model D5V4 and 500 years . . . . . | 113 |
| B.5  | The same as B3 for the model D5.5V4 . . . . .             | 114 |
| B.6  | The same as B4 for the model D5.5V4 . . . . .             | 115 |
| B.7  | The same as B3 for the model D6V4 . . . . .               | 116 |
| B.8  | The same as B4 for the model D6V4 . . . . .               | 117 |
| B.9  | The same as B3 for the model D6.5V4 . . . . .             | 118 |
| B.10 | The same as B4 for the model D6.5V4 . . . . .             | 119 |
| B.11 | The same as B3 for the model D7V4 . . . . .               | 120 |
| B.12 | The same as B4 for the model D7V4 . . . . .               | 121 |



# List of Tables

|     |  |    |
|-----|--|----|
| 2.1 | Initial conditions of the numerical models . . . . .   | 24 |
| 2.2 | Analytic and numerical scale length $x_0$ and time $t_0$ for models with $v_0 = 300 \text{ km s}^{-1}$ | 32 |
| 2.3 | Analytic and numerical scale length $x_0$ and time $t_0$ for models with $v_0 = 500 \text{ km s}^{-1}$ | 32 |
| 4.1 | Initial conditions in KIMYA . . . . .  | 64 |
| 4.2 | Relative densities to $\text{H}_2$ . . . . .   | 65 |
| 4.3 | Gas phase reactions used to model the NO formed during lightning discharge. . . . .                    | 76 |
| 4.4 | Numerical Models . . . . .   | 77 |
| 5.1 | Physical initial conditions of the numerical simulations . . . . .                                     | 85 |